FOCUS ARTICLE

Ab Initio Approaches to Simulate Molecular Polaritons: Properties and Quantum Dynamics

Braden M. Weight[1] | **Pengfei Huo**[2,3]

[1] Department of Physics and Astronomy, University of Rochester, Rochester, NY 14627, U.S.A.

[2] Department of Chemistry, University of Rochester, Rochester, NY 14627, U.S.A.

[3] The Institute of Optics, Hajim School of Engineering, University of Rochester, Rochester, NY, 14627, U.S.A.

Correspondence
Braden M. Weight Department of Physics and Astronomy, University of Rochester, Rochester, NY 14627, U.S.A.
Email: bweight@ur.rochester.edu
Pengfei Huo, Department of Chemistry, University of Rochester, Rochester, NY 14627, U.S.A.
Email: pengfei.huo@rochester.edu

Funding information
National Science Foundation CAREER Award under Grant No. CHE-1845747; National Science Foundation “Center for Quantum Electrodynamics for Selective Transformations (QuEST)” under the Grant number CHE-2124398

Molecular polaritons are hybrid states formed by the quantum mechanical interaction between light and matter. Recent experiments have shown the ability to drastically modify chemical reactions in both the ground and excited states through the hybridization of the electronic and photonic degrees of freedom. *Ab initio* simulations of molecular polaritons have demonstrated similar effects for simple ground and excited state reactions. However, the theoretical community has been limited in its ability to describe the complicated dynamical processes of many-molecule collective effects with high-level treatment of all degrees of freedom within a rigorous Hamiltonian. In this review, we provide a general description and overall procedure for exploring molecular polaritons, leveraging standard many-body electronic structure calculations combined with the exact, non-relativistic quantum electrodynamics light-matter Hamiltonian.

KEYWORDS
Polariton, Light-Matter Interaction, *Ab Initio* Electronic Structure, Optical Cavity, Nonadiabatic Dynamics

Contents

1 | INTRODUCTION

Coupling matter (atoms, molecules, or solid-state materials) to the quantized electromagnetic field inside an optical cavity creates a set of new photon-matter hybrid states, so-called polariton states.[1;2;3] These polariton states have delocalized excitations among molecules and the cavity mode, which have been shown to facilitate new chemical reactivities.[3;4;1] Theoretical investigations play a crucial role in understanding new principles in this emerging field and have suggested interesting reaction mechanisms enabled by cavity quantum electrodynamics (QED).[5;6;7;8;9;10;11;12;13;14]

Unlike traditional coherent control strategies[15;16], polariton chemistry does not rely on fragile electronic coherence[15;16] and is robust against decoherence[10]. Compared to the classical laser-matter interactions which operate with a large number of photons, cavity QED enables the hybrid system to initiate chemical reactions even without photons initially present in the cavity[3]. Thus, polariton chemistry provides a new strategy for controlling chemical reactivity in a general way by tuning the fundamental properties of photons and provides a new paradigm for enabling chemical transformations that can profoundly impact catalysis, energy production, and the field of chemistry at large.[17;18;19]

However, recent experimental demonstrations[3;20;4;1;21] of this modification of chemical reactivity are not well understood and, in some cases, not reproducible[22;23]. Since these polaritonic systems often require a quantum mechanical description of the photonic modes, existing physical chemistry theories for chemical reactions are no longer directly applicable to these hybrid systems, requiring a more exact QED approach. While the fundamental theories of QED has been known for decades, directly translating this knowledge to explain measurements of polariton chemistry remains as a major challenge in both theoretical chemistry and quantum optics. Namely, the mechanism behind the strong coupling of a mesoscopic ensemble of molecules to a single optical cavity is still not fully understood. The basic theory for describing the modes in different types of cavity is also briefly discussed in Sec. 2 and 5.3.

Additionally, simulating the time-dependent polariton quantum dynamics of the hybrid matter-field systems is often a necessary and essential task, as these polariton photochemical reactions often involve a complex dynamical interplay among the electronic, nuclear, and photonic degrees of freedom (DOFs). However, accurately simulating polaritonic quantum dynamics remains a challenging task and is beyond the paradigm of traditional photochemistry, which does not include quantized photons, and quantum optics which does not have a well-defined theory to include the influence of nuclear degrees of freedom to describe reactivity nor properly account for molecular structures.[24] Over the past years, enormous progress has been made to address this interdisciplinary challenge. We have witnessed how electronic structure theory (Sec. 3.2) and non-adiabatic quantum dynamics (Sec. 4) have actively participated in this progressing this exciting field.

In Sec. 2, we discuss the rigorous theoretical background of molecular cavity QED. We first review the basic theory of the molecular Hamiltonian (Sec. 2.1) and introduce the necessary formalism for molecular quantum electrodynamics (Sec. 2.2). Sec.3 focuses on solving the polaritonic eigenvalue equation using various approaches from direct diagonalization in the adiabatic-Fock basis (Sec. 3.1.1) and polarized Fock basis (Sec. 3.1.2) as well as the self-consistent solution at the mean-field (Sec. 3.2.2) and correlated (Sec. 3.2.3) levels of theory. Using the tools put forth in the previous two sections, Sec. 4 explores the rich quantum dynamics of strongly coupled light-matter systems, laying out common approaches toward simulating exact (Sec. 4.1) and realistic (Sec. 4.2.1-4.2.3) molecules in the extended Hilbert space of the coupled electron-photon system as well as motivating the need for an accurate description and efficient calculation of the nuclear gradients (Sec. 4.3) used in the exact Pauli-Fierz Hamiltonian. Finally, in Sec. 5, we provide three directions toward a more complete picture of the molecular polariton picture in experiments, including machine learning polariton gradients (Sec. 5.1), the simulation and effects of cavity loss (Sec. 5.2), and the extension to many molecule and many cavity modes (Sec. 5.3).

The purpose of this review is to introduce and outline state-of-the-art techniques toward the simulation of realistic, *ab initio* molecular polaritons for the readers in the emergent field of polariton chemistry. This review captures much of the recent work, but not all, toward the description of polaritonic states and properties, as well as their quantum dynamics. Specifically, this work focuses on the methods and approaches needed for one to explore these complicated problems in more depth and does not primarily focus on connecting theory to experiment. While this connection is intrinsic to the answers one seeks from simulation, the discussion of experimental progress and its setbacks is beyond the scope of this review aimed at *ab initio* computational approaches. We hope that this work allows readers of all kinds to becomes acquainted with the simulation of molecular polaritons to explore the the many unknown possibilities this novel tool has in order to manipulate chemical reactions as well as physical phenomena and to help the community to address the many open questions still unexplored by theory and simulation.

2 | QED THEORETICAL BACKGROUND

2.1 | Molecular Hamiltonian

The molecular Hamiltonian $\hat{H}_\mathrm{M}$ can be written in terms of the nuclear kinetic energy operator $\hat{T}_R$ and the electronic Hamiltonian $\hat{H}_\mathrm{el}$ as,

$$\hat{H}_\mathrm{M} = \hat{T}_R + \hat{H}_\mathrm{el} = \hat{T}_R + \hat{T}_r + \hat{V}, \tag{1}$$

where $\hat{T}_r$ is the electronic kinetic energy operator and $\hat{V}(\mathbf{R}) = \hat{V}_\mathrm{NN} + \hat{V}_\mathrm{eN} + \hat{V}_\mathrm{ee}$ is the electronic potential including the nuclear-nuclear $\hat{V}_\mathrm{NN}$, electron-nuclear $\hat{V}_\mathrm{eN}$, and electron-electron $\hat{V}_\mathrm{ee}$ interactions. The electronic Hamiltonian $\hat{H}_\mathrm{el} = \hat{H}_\mathrm{M} - \hat{T}_R$ is routinely diagonalized via standard electronic structure packages, which attempt to solve the following eigenvalue problem,

$$\hat{H}_\mathrm{el}|\psi_\alpha(\mathbf{R})\rangle = E_\alpha(\mathbf{R})|\psi_\alpha(\mathbf{R})\rangle, \tag{2}$$

which defines the adiabatic electronic states $|\psi_\alpha(\mathbf{R})\rangle$ and potential energy surfaces $E_\alpha(\mathbf{R})$ for the α_th state. Note that both the eigenvalues and eigenfunctions are parameterized by the nuclear positions in the Born-Oppenheimer approximation. In this basis, the molecular Hamiltonian $\hat{H}_\mathrm{M}$ can be written as,

$$\hat{H}_\mathrm{M} = \sum_\alpha E_\alpha(\mathbf{R})|\psi_\alpha\rangle\langle\psi_\alpha| - \frac{\hbar^2}{2\mathbf{M}}\sum_{\alpha\beta}\left[\nabla^2_\mathbf{R}\delta_{\alpha\beta} + 2\mathbf{d}_{\alpha\beta}(\mathbf{R})\cdot\nabla_\mathbf{R} + D_{\alpha\beta}(\mathbf{R})\right]|\psi_\alpha\rangle\langle\psi_\beta| \tag{3}$$

where $\hat{\mathbf{P}}$ is the nuclear momentum operator, $\mathbf{M}$ is the tensor of nuclear masses, and $\nabla_\mathbf{R}$ is the nuclear gradient. Note that we have used the shorthand notation $|\psi_\alpha\rangle \equiv |\psi_\alpha(\mathbf{R})\rangle$. Additionally, $\mathbf{d}_{\alpha\beta}$ is the derivative coupling, expressed as

$$\mathbf{d}_{\alpha\beta}(\mathbf{R}) = \langle\psi_\alpha|\nabla_\mathbf{R}|\psi_\beta\rangle = \frac{\langle\psi_\alpha|\nabla_\mathbf{R}\hat{H}_\mathrm{el}|\psi_\beta\rangle}{E_\beta - E_\alpha}. \tag{4}$$

and $D_{\alpha\beta}(\mathbf{R})$ is the second-derivative coupling, expressed as,

$$D_{\alpha\beta}(\mathbf{R}) = \langle\psi_\alpha|\nabla_\mathbf{R}\cdot\nabla_\mathbf{R}|\psi_\beta\rangle = \langle\psi_\alpha|\nabla^2_\mathbf{R}|\psi_\beta\rangle. \tag{5}$$

The coupling between light and matter, as we will see later, is mediated via the molecular dipole operator $\hat{\boldsymbol{\mu}} = \sum_i z_i\hat{\mathbf{R}}_i - \sum_k \hat{\mathbf{r}}_k$ and the quantized electric field of the optical cavity $\hat{\mathbf{E}}$. The matrix elements of the dipole operator in the adiabatic basis can be written as,

$$\tilde{\mu}_{\alpha\beta}(\mathbf{R}) = \langle\psi_\alpha|\hat{\tilde{\mu}}|\psi_\beta\rangle. \tag{6}$$

For large systems with many electrons, the maximum number of electronic states becomes impractically large for standard electronic structure calculations, even considering only the single excitation manifold. Further, for single-reference methods, such as linear response time-dependent density functionally theory (LR-TD-DFT), the efficient *and accurate* calculation of high-energy excited states is not always trustworthy, so in practice we employ a smaller Hilbert space than that implied by the total molecular Hamiltonian $\hat{H}_\mathrm{M}$ in Eq. 3, which can be defined through the following projection operator,

$$\hat{\mathcal{P}} = \sum_{\alpha=0}^{\mathcal{N}_{\mathrm{el}}-1} |\psi_\alpha\rangle\langle\psi_\alpha|, \tag{7}$$

where $\mathcal{N}_{\mathrm{el}}$ is the number of included adiabatic electronic states (ordered by increasing energy). The identity operator for the total Hilbert space can be written as $\hat{\mathcal{I}}_{\mathrm{el}} = \hat{\mathcal{P}}+\hat{\mathcal{Q}}$, where $\hat{\mathcal{Q}}$ is composed of all non-included states. The projected molecular Hamiltonian can be written as,

$$\hat{\mathcal{P}}\hat{H}_{\mathrm{M}}\hat{\mathcal{P}} = \sum_{\alpha=0}^{\mathcal{N}_{\mathrm{el}}-1} E_\alpha|\psi_\alpha\rangle\langle\psi_\alpha| - \frac{\hbar^2}{2\mathbf{M}} \cdot \sum_{\alpha\beta=0}^{\mathcal{N}_{\mathrm{el}}-1} \left[\nabla_{\mathbf{R}}^2\delta_{\alpha\beta} + 2\mathbf{d}_{\alpha,\beta}\cdot\nabla_{\mathbf{R}} + D_{\alpha\beta}\right]|\psi_\alpha\rangle\langle\psi_\beta|. \tag{8}$$

For the remainder of this work, it will be assumed that all Hamiltonians and operators reside in the truncated Hilbert space $\hat{\mathcal{P}}\hat{H}_{\mathrm{M}}\hat{\mathcal{P}} \to \hat{H}_{\mathrm{M}}$. The dipole operator can also be written in the truncated Hilbert space as,

$$\hat{\mathcal{P}}\hat{\boldsymbol{\mu}}\hat{\mathcal{P}} = \sum_{\alpha,\beta=0}^{\mathcal{N}_{\mathrm{el}}-1} \boldsymbol{\mu}_{\alpha\beta}\ |\psi_\alpha\rangle\langle\psi_\beta|. \tag{9}$$

Later, in Sec. 3.1.2, we will examine an entangled basis for the electron and photon degrees of freedom which we call the polarized Fock state (PFS) basis. In order to construct this basis, we require a unitary transformation of the electronic states such that the dipole operator in the truncated Hilbert space is diagonal. In this way, we can define the dipole operator as,

$$\hat{\mathcal{P}}\hat{\boldsymbol{\mu}}\hat{\mathcal{P}} = \sum_{\nu=0}^{\mathcal{N}_{\mathrm{el}}-1} \boldsymbol{\mu}_{\nu\nu}\ |\phi_\nu\rangle\langle\phi_\nu|. \tag{10}$$

where $|\phi_\nu\rangle$ is the eigenstate of the projected dipole operator $\hat{\mathcal{P}}\hat{\boldsymbol{\mu}}\hat{\mathcal{P}}$ with

$$|\phi_\nu\rangle = \sum_{\alpha=0}^{\mathcal{N}_{\mathrm{el}}-1} c_\alpha^\nu(\mathbf{R})|\psi_\alpha(\mathbf{R})\rangle, \tag{11}$$

and $c_\alpha^\nu = \langle\psi_\alpha|\phi_\nu\rangle$. These states are commonly referred to as Mulliken-Hush (MH) states. In this basis, the electronic Hamiltonian rotates to an off-diagonal matrix as,

$$\hat{H}_{\mathrm{el}} = \sum_{\nu\mu}^{\mathcal{N}_{\mathrm{el}}-1} V_{\nu\mu}(\mathbf{R})|\phi_\nu(\mathbf{R})\rangle\langle\phi_\mu(\mathbf{R})|. \tag{12}$$

2.2 | Pauli-Fierz Hamiltonian

Often, for finite molecular systems, the Pauli-Fierz (PF) Hamiltonian $\hat{H}_{\mathrm{PF}}$ is chosen to model the interactions between the molecular and photonic degrees of freedom inside an optical or plasmonic cavity. We will first introduce the single-mode, single-molecular description; although, later in Section 2.3, we will generalize to the collective many-mode, many-molecule Hamiltonian needed to describe experimental conditions. At this level, the PF Hamiltonian can be written as,

$$\begin{aligned}\hat{H}_{\mathrm{PF}} &= \hat{H}_{\mathrm{M}} + \hat{H}_{\mathrm{ph}} + \hat{H}_{\mathrm{el-ph}} + \hat{H}_{\mathrm{DSE}} \\ &= \hat{H}_{\mathrm{M}} \ + \ \hbar\omega_{\mathrm{c}}(\hat{a}^{\dagger}\hat{a} + \frac{1}{2}) \ + \ \sqrt{\frac{\omega_{\mathrm{c}}}{2}}\boldsymbol{\lambda}\cdot\hat{\boldsymbol{\mu}}(\hat{a}^{\dagger} + \hat{a}) \ + \ \frac{1}{2\hbar}(\boldsymbol{\lambda}\cdot\hat{\boldsymbol{\mu}})^{2} \\ &= \hat{H}_{\mathrm{M}} + \frac{1}{2}\hat{p}_{\mathrm{c}}^{2} + \frac{1}{2}\omega_{\mathrm{c}}^{2}\left(\hat{q}_{\mathrm{c}} + \frac{\boldsymbol{\lambda}}{\omega_{\mathrm{c}}\sqrt{\hbar}}\cdot\hat{\boldsymbol{\mu}}\right)^{2},\end{aligned} \tag{13}$$

where ω_{c} is the cavity frequency and $\hat{a}^{\dagger}$ ($\hat{a}$) is creation (annihilation) ladder operator for the photon field. The Hamiltonian can be factored into the form of a shifted harmonic oscillator via the definition of the canonical coordinates (*i.e.* the operators of positions and momentum) of the quantum harmonic oscillator: $\hat{q}_{\mathrm{c}} = \sqrt{\frac{\hbar}{2\omega_{\mathrm{c}}}}(\hat{a}^{\dagger} + \hat{a})$ and $\hat{p}_{\mathrm{c}} = \sqrt{\frac{\hbar\omega_{\mathrm{c}}}{2}}(\hat{a}^{\dagger} - \hat{a})$. Here $\boldsymbol{\lambda}$ is the light-matter coupling strength commonly used in the literature. Another common choice is the transverse vector potential of the photonic field $\mathbf{A}_0$, related to $\boldsymbol{\lambda}$ as

$$\boldsymbol{\lambda} = \sqrt{\frac{\hbar}{\varepsilon\mathcal{V}}}\hat{\mathbf{e}} \quad \text{and} \quad \mathbf{A}_0 = \sqrt{\frac{\hbar}{2\omega_{\mathrm{c}}\varepsilon\mathcal{V}}}\,\hat{\mathbf{e}} = \sqrt{\frac{1}{2\omega_{\mathrm{c}}}}\,\boldsymbol{\lambda}, \tag{14}$$

where $\mathcal{V}$ is the quantization volume of the photon field, ε is the electric permittivity, and $\hat{\mathbf{e}}$ is the unit vector of the electric field polarization. Eq. 13 is composed of four main elements: the molecular Hamiltonian $\hat{H}_{\mathrm{M}}$, the photonic Hamiltonian $\hat{H}_{\mathrm{ph}}$, the light-matter interaction $\hat{H}_{\mathrm{el-ph}}$, and the dipole self-energy $\hat{H}_{\mathrm{DSE}}$. Similarly to the molecular Hamiltonian, we wish to solve an eigenvalue problem without the nuclear kinetic energy operator $\hat{T}_{R}$, which we define the polaritonic Hamiltonian $\hat{H}_{\mathrm{pl}}$ (analogously to the electronic Hamiltonian $\hat{H}_{\mathrm{el}}$) as,

$$\hat{H}_{\mathrm{pl}} = \hat{H}_{\mathrm{PF}} - \hat{T}_{\mathrm{R}} = \hat{H}_{\mathrm{el}} + \hat{H}_{\mathrm{ph}} + \hat{H}_{\mathrm{el-ph}} + \hat{H}_{\mathrm{DSE}}, \tag{15}$$

whose eigenvalue equation can be written as,

$$\hat{H}_{\mathrm{pl}}|\mathcal{E}_j(\mathbf{R})\rangle = \mathcal{E}_j(\mathbf{R})|\mathcal{E}_j(\mathbf{R})\rangle, \tag{16}$$

where $\mathcal{E}_j(\mathbf{R})$ are the Born-Oppenheimer polaritonic potential energy surfaces and $|\mathcal{E}_j(\mathbf{R})\rangle$ are the adiabatic polaritonic states. The focus of Section 3 will be to explore solving such eigenvalue problems in various choices of basis states and to calculate chemically and physically relevant properties from such polaritonic wavefunctions.

2.3 | Collective Hamiltonian

Although many successful single-molecule experiments[25;26] and theoretical[10;27;28] work have been instrumental in probing the basic physics of polaritonics, most experiments are constructed such that a large ensemble (often $\sim 10^8$ or more) of molecules is coupled simultaneously to many modes of the cavity.[29;30;31;3;30] These many coupled DOFs generate collective upper and lower polaritonic states[29;32;9] as well as the dense manifold of “dark states” which contain minuscule amounts of photonic character and negligible transition dipole.[29]

The direct generalization of Eq. 13 for many molecules $\mathcal{N}_{\mathrm{mol}}$ and cavity modes $\mathcal{N}_{\mathrm{mode}}$, including both parallel k_x

(quasi-continuous) and perpendicular k_z (discrete) modes, can be written as,

$$\begin{aligned}\hat{H}_{\mathrm{PF}}^{\mathrm{G}} = \hat{H}_{\mathrm{M}} + \sum_{\boldsymbol{k}}^{\mathcal{N}_{\mathrm{mode}}} \sum_{p} \Bigg(\hbar\omega_{\boldsymbol{k}} (\hat{a}_{\boldsymbol{k}}^{\dagger}\hat{a}_{\boldsymbol{k}} + \frac{1}{2}) + \sum_{A}^{\mathcal{N}_{\mathrm{mol}}} \sqrt{\frac{\omega_{\mathbf{k}}}{2}} \boldsymbol{\lambda}_{\boldsymbol{k},p} \cdot \hat{\boldsymbol{\mu}}_A(\mathbf{R}_A) (\hat{a}_{\boldsymbol{k}} e^{i\boldsymbol{k}_x \cdot \mathbf{x}_A} + \hat{a}_{\boldsymbol{k}}^{\dagger} e^{-i\boldsymbol{k}_x \cdot \mathbf{x}_A}) \\ + \sum_{A,B}^{\mathcal{N}_{\mathrm{mol}}} \frac{1}{2\hbar} (\boldsymbol{\lambda}_{\boldsymbol{k},p} \cdot \hat{\boldsymbol{\mu}}_A(\mathbf{R}_A)) (\boldsymbol{\lambda}_{\boldsymbol{k},p} \cdot \hat{\boldsymbol{\mu}}_B(\mathbf{R}_B)) e^{-i\boldsymbol{k}_x \cdot (\mathbf{x}_A - \mathbf{x}_B)} \Bigg).\end{aligned} \tag{17}$$

Here, $\mathbf{x}_A$ denotes the center-of-mass position of molecule A and $\mathbf{R}_A$ denotes the nuclear coordinates of molecule A. For typical Fabry-Perot cavities, the photon energy required to excite the cavity mode with the wavevector, $\mathbf{k} = \langle k_x, k_z \rangle$, is $E_{\mathrm{ph}}(\theta) = \frac{\hbar}{n_{\mathrm{c}}} c \sqrt{k_z^2 + k_x^2} = \frac{\hbar}{n_{\mathrm{c}}} c k_z \sqrt{1 + \tan^2\theta}$, which depends on the angle θ ($\tan\theta = k_x/k_z$) of the external probe. Here, c is the speed of light in vacuum, n_{c} is the refractive index inside the cavity, and $\hbar\mathbf{k}$ is the momentum of the photon. While the collective Hamiltonian (Eq. 17) is an extremely important physical object to describe experimental conditions, we will focus the majority of our discussion on the single-molecule, single-mode case (Eq. 13) and return to the collective case in Sec. 5 where we will describe extensions toward the realistic modeling of polaritonic states and their dynamics.

3 | OBTAINING POLARITON EIGENSTATES AND THEIR PROPERTIES

3.1 | Direct Diagonalization

Diagonalizing Hamiltonians is the main task of all quantum mechanics. If one can achieve the exact diagonalization of the Hamiltonian for all DOFs, the exact answer is returned, given a complete basis set. In reality, one is unable to achieve this due to the basis set limitations and/or the complexity of the many-body problem itself. As such, one seeks to find the best alternative toward providing approximate solutions to the many-body problem that returns the correct physics. For the electronic Hamiltonian, the community at large has spent nearly 90 years working on this problem providing methods such as Hartree-Fock theory (HF), density functional theory (DFT), configuration interaction (CI), coupled cluster (CC), among others including their excited state analogues like time-dependent DFT (TD-DFT). Each of these methods returns, to varying degrees of computational expense and accuracy, the solutions to the electronic Hamiltonian.

Considering the photonic part of the light-matter hybrid system, we know these DOFs are explicitly harmonic (*i.e.*, their bare Hamiltonian $\hat{H}_{\mathrm{ph}}$ is simply the quantum harmonic oscillator), and their exact eigenstates are known to be the Fock (or number) states of the quantized field. In this way, we already know the solutions to the unperturbed parts of the light-matter Hamiltonian *exactly* for the photons and *approximately* for the electrons. If one can directly diagonalize the light-matter Hamiltonian (Eq. 15), then one additionally receives the exact correlation between these DOFs.

In contract to a direct diagonalization, many recent works have shown that one can reconstruct the self-consistent schemes used in the many-electron problem and solve the many-electron and many-photon problem simultaneously. In this sense, the basis states are optimized (or are allowed to respond to interactions with the photon DOFs) to achieve a minimization of the energy, subject to the underlying approximations of the theory (*e.g.* density functional theory). Further, the electron-electron, electron-photon, and photon-photon correlations are forced to be described on the same footing. In the following, we will focus our description to direct diagonalization techniques to achieve the *exact* electron-photon correlation, making use of standard electronic structure packages that have been thoroughly tested and are both freely and commercially available. In the last section (Sec. 3.2), we will briefly motivate cases where a self-consistent approach would be advantageous and outline the idea behind such schemes.

3.1.1 | Adiabatic-Fock Basis

In the adiabatic electronic basis $|\psi_\alpha\rangle$ (eigenstates of $\hat{H}_{\mathrm{el}}$) paired with the Fock (or number) basis for the photonic DOFs $|n\rangle$ (eigenstates of $\hat{H}_{\mathrm{ph}} = \hbar\omega_{\mathrm{c}}(\hat{a}^\dagger\hat{a} + \frac{1}{2})$), the matrix elements of the polaritonic Hamiltonian can be written as.

$$\begin{aligned}(\hat{\mathcal{H}}_{\mathrm{pl}})_{\alpha\beta,nm}(\mathbf{R}) &= \left[E_\alpha + \hbar\omega_{\mathrm{c}}(n+\frac{1}{2})\right]\delta_{\alpha\beta}\delta_{nm} + \sqrt{\frac{\omega_{\mathrm{c}}}{2}}\lambda(\tilde{\mu}_{\alpha\beta}\cdot\hat{\mathbf{e}})(\sqrt{n}\delta_{n,m-1} + \sqrt{n+1}\delta_{n,m+1}) \\ &\quad + \frac{1}{2\hbar}\lambda^2\sum_{\gamma=0}^{\mathcal{N}_{\mathrm{el}}-1}(\tilde{\mu}_{\alpha\gamma}\cdot\hat{\mathbf{e}})(\tilde{\mu}_{\gamma\beta}\cdot\hat{\mathbf{e}})\delta_{nm} \\ &= \epsilon_{\alpha,n}(\mathbf{R})\delta_{\alpha\beta}\delta_{nm} + \tilde{\mu}_{\alpha\beta}(\mathbf{R})\eta_{nm} + \mathcal{D}_{\alpha\beta}(\mathbf{R})\delta_{nm},\end{aligned} \tag{18}$$

where $\{\alpha,\beta,\gamma\}$ label the electronic adiabatic states (in the subspace defined by the $\mathcal{N}_{\mathrm{el}}$ lowest-energy states), $\{n,m\}$ label the photonic Fock states (in the subspace defined by the $\mathcal{N}_{\mathrm{F}}$ lowest-energy states), $\hat{\mathbf{e}}$ is the polarization unit vector of the electric field, $\epsilon_{\alpha,n} = E_\alpha + \hbar\omega_{\mathrm{c}}(n+\frac{1}{2})$, $\tilde{\mu}_{\alpha\beta} = \sqrt{\frac{\omega_{\mathrm{c}}}{2}}\lambda(\hat{\mathbf{e}}\cdot\tilde{\mu}_{\alpha\beta})$, $\eta_{nm} = (\sqrt{n}\delta_{n,m-1} + \sqrt{n+1}\delta_{n,m+1})$, and $\mathcal{D}_{\alpha\beta} = \frac{1}{2\hbar}\lambda^2\sum_\gamma(\tilde{\mu}_{\alpha\gamma}\cdot\hat{\mathbf{e}})(\tilde{\mu}_{\gamma\beta}\cdot\hat{\mathbf{e}})$. Here, from the perspective of electronic structure, only the electronically adiabatic state energies E_α and dipole matrix elements $\mu_{\alpha\beta}$ are required as input. Note that in the last line of Eq. 18, we have explicitly inserted the dependence on the nuclear positions **R** for clarity, but in general we choose to neglect writing such dependence for the sake of clarity. The photonic basis is in principle infinite, since the harmonic oscillator has infinite eigenstates, so, similar to the electronic subspace which is truncated at $\mathcal{N}_{\mathrm{el}}$ (Eq. 7), we also introduce a truncation of the photonic Hilbert space including only the lowest $\mathcal{N}_{\mathrm{F}}$ Fock states. The polaritonic Hamiltonian can be easily constructed via Kronecker products (*e.g.*, $\hat{\mu}\otimes\hat{a}$) of the sub-space operators; however, it is worth noting the extreme sparsity afforded by the Fock basis. To make this clear from a visual perspective, the block-like nature of the matrix in this basis can be written as,

$$\hat{\mathcal{H}}_{\mathrm{pl}} = \begin{bmatrix} E_0+\mathcal{D}_{00} & \mathcal{D}_{01} & \cdots & \tilde{\mu}_{00} & \tilde{\mu}_{01} & \cdots \\ \mathcal{D}_{01} & E_1+\mathcal{D}_{11} & \cdots & \tilde{\mu}_{01} & \tilde{\mu}_{11} & \cdots \\ \vdots & \vdots & \ddots & \vdots & \vdots & \vdots \\ \tilde{\mu}_{00} & \tilde{\mu}_{01} & \cdots & E_0+\omega_{\mathrm{c}}+\mathcal{D}_{00} & \mathcal{D}_{01} & \cdots \\ \tilde{\mu}_{01} & \tilde{\mu}_{11} & \cdots & \mathcal{D}_{01} & E_1+\omega_{\mathrm{c}}+\mathcal{D}_{11} & \cdots \\ \vdots & \vdots & \vdots & \vdots & \vdots & \ddots \end{bmatrix} = \begin{bmatrix} \mathbf{M}_0 & \tilde{\boldsymbol{\mu}} & 0 & 0 & \cdots & 0 \\ \tilde{\boldsymbol{\mu}} & \mathbf{M}_1 & \sqrt{2}\tilde{\boldsymbol{\mu}} & 0 & \cdots & 0 \\ 0 & \sqrt{2}\tilde{\boldsymbol{\mu}} & \mathbf{M}_2 & \sqrt{3}\tilde{\boldsymbol{\mu}} & \cdots & 0 \\ 0 & 0 & \sqrt{3}\tilde{\boldsymbol{\mu}} & \ddots & \ddots & \vdots \\ \vdots & \vdots & \vdots & \ddots & \ddots & \sqrt{\mathcal{N}_{\mathrm{F}}}\tilde{\boldsymbol{\mu}} \\ 0 & 0 & 0 & \cdots & \sqrt{\mathcal{N}_{\mathrm{F}}}\tilde{\boldsymbol{\mu}} & \mathbf{M}_{\mathcal{N}_F} \end{bmatrix}. \tag{19}$$

A few important properties of this matrix are as follows: (I) The $\mathcal{N}_{\mathrm{F}}$ block diagonals $\mathbf{M}_n$ are composed of the diagonal energies and diagonal DSE elements $\epsilon_{\alpha,n} + \mathcal{D}_{\alpha\alpha}$ in addition to the off-diagonal DSE elements $\mathcal{D}_{\alpha\beta}$. (II) The super- and sub-diagonal blocks are composed only of the matter dipole operator matrix elements $\tilde{\mu}_{\alpha\beta}$ weighted by the photon number of the larger diagonal Fock state label n. Note here that for clarity, we have neglected the zero-point energy of the photonic mode and **R** dependence. One can easily see from the right-most side of Eq. 19 that this matrix is extremely sparse, especially for larger number of included Fock basis states (needed for convergence), so many approximate diagonalization schemes can be used which rely on the properties of sparse matrices, such as the Lanczos and Krylov subspace techniques,[33;34;35] and are able to return the lowest eigenvalues and eigenvectors without loss of physics but with a large computational speed-up.

Upon diagonalization of Eq. 19, the polaritonic states are represented as linear combinations of the adiabatic-Fock

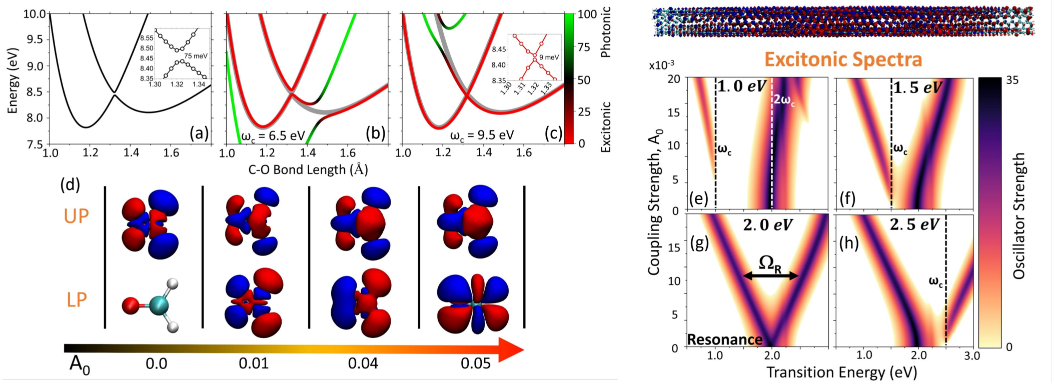

FIGURE 1 (a) Adiabatic potential energy surface of the formaldehyde molecule's A_1-symmetry excited states as a function of the C-O bond length, R_{CO}. The inset presents the avoided crossing between the two adiabatic states. (b)-(c): Polariton excited state energy $\mathcal{E}_j(R_{\mathrm{CO}}) - \mathrm{MIN}[\mathcal{E}_0(R_{\mathrm{CO}})]$ of the formaldehyde-cavity hybrid system, with the coupling strength of $A_0 = 0.04$ a.u., and a cavity frequency (b) $\omega_{\mathrm{c}} = 6.5$ eV and (c) $\omega_c = 9.5$ eV. The cavity polarization is parallel to the C-O bond. For panels (b)-(c), the color map indicates the photonic character and the cavity-free electronic states are shown as thick gray lines. The inset in panel c shows the reduction of the avoided crossing from 75 to 9 meV. (d) Polaritonic transition density $\rho^{\mathrm{M}}_{0j}(\mathbf{r})$ of the upper (UP) and lower (LP) polaritons for A_0 = 0 a.u., 0.01 a.u., 0.04 a.u., and 0.05 a.u. at $\omega_{\mathrm{c}} = 7.92$ eV with a C-O bond length of 1.22 Å. (e)-(h) Excitonic absorption spectra of a (6,5) single-walled carbon nanotube (SWCNT) coupled to an optical cavity plotted as a function of the transition energy and coupling strength A_0. The Lorentzian energy-broadening parameter is $\sigma = 0.1$ eV. The cavity frequency is taken to be (e) $\omega_{\mathrm{c}} = 1.0$ eV (half-resonance), (f) $\omega_{\mathrm{c}} = 1.5$ eV, (g) $\omega_{\mathrm{c}} = 2.0$ eV (resonant with bright molecular transition, E_{11}), and (h) $\omega_{\mathrm{c}} = 2.5$ eV. (Above) The polaritonic transition density at $A_0 = 0.0$ a.u. is shown above the spectra for the ground-to-bright E_{11} transition.

basis states (with contracted notation $|\psi_\alpha(\mathbf{R})\rangle \otimes |n\rangle = |\psi_\alpha(\mathbf{R}), n\rangle$) as,

$$|\Phi_j(\mathbf{R})\rangle = \sum_{\alpha}^{\mathcal{N}_{\mathrm{el}}} \sum_{n}^{\mathcal{N}_{\mathrm{F}}} C^j_{\alpha n} |\psi_\alpha(\mathbf{R}), n\rangle, \tag{20}$$

where $C^j_{\alpha n} = \langle \psi_\alpha(\mathbf{R}), n | \Phi_j(\mathbf{R})\rangle$. Here, $\mathcal{N}_{\mathrm{el}}$ and $\mathcal{N}_{\mathrm{F}}$ are treated as convergence parameters such that the polaritonic observables are adequately converged (see more details in Section 3.1.3). The obvious first choice is the convergence of the lowest-energy eigenvalues of Eq. 19. In our experience with realistic *ab initio* systems, the convergence with respect to the number of Fock states is rapid, only requiring $\mathcal{N}_{\mathrm{F}} \sim 5$ to obtain ~10 meV accuracy. However, due to the complicated and highly off-diagonal dipole matrix[36] in real molecules, the convergence with respect to electronic states is slow, possibly requiring $\mathcal{N}_{\mathrm{el}} \sim 100$ or more states to achieve ~10 meV accuracy.[37;38] In Sec. 3.2, we will briefly address other approaches, namely self-consistent schemes, to converge complicated systems which contain many strongly dipole-connected states as well as systems with large light-matter coupling that necessitate a more advanced and rigorous approach toward obtaining the polaritonic eigenstates in a self-consistent way.

Fig. 1a-d presents excited state potential energy surfaces of formaldehyde as a function of the C-O bond length, showing the two lowest-energy excited states with ground-to-excited transition dipole along the C-O bond direction (which is parallel to the cavity polarization direction, $\hat{e}$). The bare electronic states (Fig. 1a) show two local minima in the lower-energy excited state as well as an avoided crossing (see inset). Upon coupling to the cavity, the local minima near C-O bond length of 1.50 Å can be removed with a negatively detuned cavity (ω_c = 6.5 eV, Fig. 1b, colorbar indicates the average photonic character $\langle \hat{a}^\dagger \hat{a} \rangle$). Alternatively, the avoided crossing can be systematically reduced via a positively detuned cavity (ω_c = 9.5 eV, Fig. 1c, see inset). An important feature of this change in the avoided crossing is that the character of both states involved is retained (*i.e.*, mainly electronic excitation character) where both states exhibit negligible amounts of photonic contributions. Direct control over the relative energy of electronic states while maintaining their original character is a useful concept and design principle in processes controlled by non-adiabatic coupling between the excited electronic states.

Fig. 1d presents the matter-projected polaritonic transition density in real space,

$$\rho^{\mathrm{M}}_{0j}(\mathbf{r}) = \langle \mathbf{r} | \mathrm{Tr}_{\mathrm{ph}}\left[\hat{\rho}_{0j}\right] | \mathbf{r} \rangle = \sum_{\alpha\beta}^{\mathcal{N}_{\mathrm{el}}} \sum_{n}^{\mathcal{N}_{\mathrm{F}}} C^{0}_{\alpha n} (C^{j}_{\beta n})^* \cdot \xi^{\mathrm{M}}_{\alpha\beta}(\mathbf{r}), \tag{21}$$

where the photonic DOFs have been traced out, leaving only the electronic contributions. Here, $\xi^{\mathrm{M}}_{\alpha\beta}(\mathbf{r}) = \psi^*_\beta(\mathbf{r})\psi_\alpha(\mathbf{r})$ is the $\alpha\beta_{\mathrm{th}}$ electronic transition density in real space $\mathbf{r}$ and $\hat{\rho}_{0j} = |\Phi_j\rangle\langle\Phi_0|$ is the $0j_{\mathrm{th}}$ polaritonic density operator. More details on calculating observables can be found in Sec. 3.1.3. The light-matter hybridization leads to superpositions between photon-dressed electronic states, which leads to various electronic transition densities mixing through the polaritonic expansion coefficients in the adiabatic-Fock basis (see Eq. 20). The matter-projected polaritonic transition density[39;37] is only one of many ways to examine the character of the molecular part of the polaritonic excitation. Other examples of matter-projected polaritonic observables are the difference density,[40;41] the natural transition orbitals,[37] the transition density matrix,[37] and other yet to be applied for the polaritonic case.

The changes of the polaritonic transition density are presented as a function of the coupling strength A_0 (varied along the horizontal axis of panel d) for the upper and lower polaritons, with a C-O bond length of 1.22 Å and at cavity energy ω_c = 7.92 eV. Under this configuration, the cavity is nearly resonant with the molecular adiabatic transition from the ground state to the $\psi_1^{\mathrm{A}_1}$ state at the Franck-Condon points. Through the coupling-dependent mixing of the various electronic transition densities, the polaritonic transition density is modified for each coupling strength, and the results showcase how tuning the cavity parameters can modify the local electronic properties to facilitate chemical reactions or photophysical changes.

Fig. 1e-h shows the excitonic spectra of a (6,5) single-walled carbon nanotube (SWCNT) system inside an optical cavity for cavity frequencies ω_c = (e) $\frac{1}{2}E_{11}$, (f) $\frac{3}{4}E_{11}$, (g) E_{11}, and (h) $\frac{5}{4}E_{11}$, where E_{11} is the lowest energy bright transition in the pristine SWCNT. This system has been the subject of recent exploration by the polaritonic community and has yielded many interesting results.[42;43;44;45;46;47] It is well known that pristine SWCNTs are relatively dark to emission due to low-lying optical inactive electronic transitions. Here, the $|\psi_0, 2\rangle$ photon-dressed ground state is in resonance with the bright $|E_{11}\rangle \equiv |\psi_6, 0\rangle$ state. At resonance (panel g), the bright character of the E_{11} state is split nearly symmetrically as a function of the light-matter coupling strength, A_0. For negatively detuned cavity (panels e,f), the bright character is blueshifted. For a positively detuned cavity (panel h), the bright character is redshifted to below the manifold of low-lying dark states, effectively brightening the emission of the SWCNT system without the need for chemical functionalization[48;49;50;51;52;53;54;55] or solvent doping.[56;57]

3.1.2 | Polarized Fock State Basis

In Section 3.1.1, we have described one possible basis for the representation of the PF Hamiltonian (Eq. 13). However, this is not the only choice. In fact, the adiabatic-Fock representation is useful in the weak coupling limit, since the basis is simply the basis that diagonalizes the unperturbed electronic ($\hat{H}_{\mathrm{el}}$) and photonic ($\hat{H}_{\mathrm{ph}}$) Hamiltonians. In this sense,

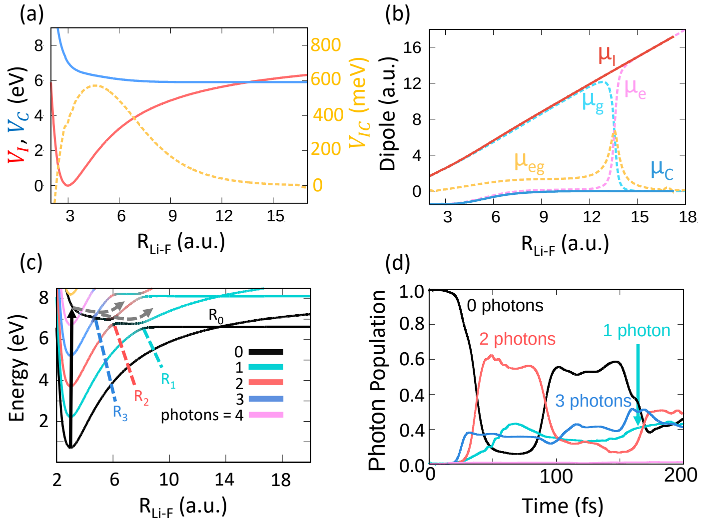

FIGURE 2 (a) Diabatic Mulliken-Hush (MH) potentials $V_I(R)$ (red) and $V_C(R)$ (blue), with diabatic coupling V_{IC} (gold line). (b) Matrix elements of $\hat{\mu}$ in the adiabatic representation (dashed curves) μ_{gg} (pink), μ_{ee} (cyan), and μ_{eg} (gold), as well as in the diabatic representation (solid lines) μ_{II} (red) and μ_{CC} (blue). Here $\mu_{II} = \mu_I$ (red) and $\mu_{CC} = \mu_C$ in the MH representation since no off-diagonal dipole elements are present in the dipole operator. (c) Polaritonic potentials color-coded according to the number of photons with four relevant avoided crossings labeled as R_0, R_1, R_2, and R_3. The black solid vertical arrow indicates the initial photoexcitation, and the dashed lines illustrate the dynamics of the hybrid system. (d) Time-dependent photon populations. For panels (c)-(d), the light-matter coupling strength set to $A_0 = 0.127$ a.u. with a cavity frequency of $\omega_c = 1.5$ eV.

when the contributions of the interaction ($\hat{H}_{e-ph}$) or dipole self-energy ($\hat{H}_{DSE}$) become large, the many adiabatic and Fock states will be needed in the description of the polaritonic wavefunctions. Other choices exist for the description of the photonic DOFs, such as the grid basis, which diagonalizes $\hat{q}_c \propto \hat{a}^\dagger + \hat{a}$ and has been extensively used.[5;58;59;60]

The choice of basis can significantly enhance computational efficiency or reduce the conceptual complexity of a problem, depending on the light-matter coupling strength and cavity frequency parameters. One such basis, aimed for use in the strong light-matter coupling regime, is the recently proposed polarized Fock State (PFS) basis introduced in Ref. 61. Here, the Pauli-Fierz Hamiltonian is rewritten using an entangled electronic-photonic basis, where the electronic states are represented by the eigenstates of the dipole operator $\sum_\nu \hat{\mathcal{P}}\hat{\mu}\hat{\mathcal{P}} = \boldsymbol{\mu}_{\nu\nu}(\mathbf{R})|\phi_\nu\rangle\langle\phi_\nu|$ and is referred to as the Mulliken-Hush (MH) representation (Eq. 11). The polaritonic Hamiltonian (see Eq. 13) in the MH basis can be written as,

$$\hat{\mathcal{H}}_{pl} = \hat{\mathcal{H}}_{el} + \frac{\hat{p}_c^2}{2} + \sum_\nu \frac{\omega_c^2}{2}\left[\hat{q}_c + q_\nu^0(\mathbf{R})\ |\phi_\nu\rangle\langle\phi_\nu|\right]^2, \tag{22}$$

where $q_\nu^0(\mathbf{R}) = -\frac{\boldsymbol{\lambda}}{\omega_c} \cdot \boldsymbol{\mu}_{\nu\nu}(\mathbf{R})$. Considering the Hamiltonian of the bare photonic field, $\hat{H}_{ph} = \frac{1}{2}(\hat{p}_c^2 + \omega_c^2\hat{q}_c^2)$, one may notice that the QED Hamiltonian is simply shifted in the position coordinate $\hat{q}_c$ by the value $-q_\nu^0(\mathbf{R})$ and is hence a shifted harmonic oscillator (or "polarized Fock state" since the field is polarized by the molecular electric multipole), unique for each MH electronic state ($|\phi_\nu\rangle$). At zero light-matter coupling or infinitely large cavity frequency, the original MH and un-shifted (or "vacuum") Fock states are returned. The light-matter Hamiltonian (Eq. 22) can be now block-diagonalized using the polarized Fock state basis (PFS) $\{|n_\nu(\mathbf{R})\rangle\}$ for each MH state $|\phi_\nu\rangle$, which is defined as,

$$\frac{1}{2}\Big[\hat{p}_c^2 + \omega_c^2\big(\hat{q}_c + q_\nu^0(\mathbf{R})\big)^2\Big]|n_\nu(\mathbf{R})\rangle \equiv (\hat{b}_\nu^\dagger \hat{b}_\nu + \frac{1}{2})\hbar\omega_c|n_\nu(\mathbf{R})\rangle = \big(n_\nu + \frac{1}{2}\big)\hbar\omega_c|n_\nu(\mathbf{R})\rangle.$$

where $\hat{b}_\nu^\dagger$ ($\hat{b}_\nu$) is the creation (annihilation) ladder operator for the shifted harmonic oscillator specific to the ν_{th} MH state. Defining the total basis as the tensor product of the MH states and the PFS basis, $|\phi_\nu(\mathbf{R})\rangle \otimes |n_\nu(\mathbf{R})\rangle \equiv |\phi_\nu(\mathbf{R}), n_\nu(\mathbf{R})\rangle$, which is an entangled light-matter basis since the molecular dipole appears in the definition of the shifted Fock state, the matrix elements of the light-matter Hamiltonian can be expressed as

$$(\hat{\mathcal{H}}_{\text{pl}})_{\nu\mu,n_\nu m_\mu} = \Big[V_{\nu\nu} + \hbar\omega_c(n_\nu + \frac{1}{2})\Big]\delta_{\nu\mu}\delta_{n_\nu m_\mu} + \langle n_\mu|m_\nu\rangle\, V_{\nu\mu}(1 - \delta_{\nu\mu}\delta_{n_\nu m_\mu}). \tag{23}$$

Note here that we have dropped the explicit dependence on the nuclear position $\mathbf{R}$ for clarity. In this basis, the diagonal matrix elements are the diagonal MH energies $V_{\nu\nu}$ (Eq. 12) and PFS harmonic oscillator eigenvalues $\omega_c(n_\nu + \frac{1}{2})$, while the off-diagonal contributions are now the MH coupling elements $V_{\nu\neq\mu}$ ***reduced in magnitude*** by the overlaps $\langle n_\epsilon|m_\nu\rangle \in [-1, 1]$ between two PFS harmonic oscillator states with n_ν photons and m_μ photons associated with two different electronic MH states ϕ_ν and ϕ_μ. In this compact basis, the light-matter coupling *and* dipole self-energy are all neatly housed in the MH coupling and PFS overlaps, $\langle n_\mu|m_\nu\rangle\, V_{\nu\mu}$, and thus all interactions between light and matter DOFs are carried through this single term. Note also that the calculation of the PFS overlaps is analytic and can be written as,

$$\langle n_\epsilon|m_\nu\rangle = (-2\xi)^{n-m} e^{-2\xi^2}\sqrt{\frac{m!}{n!}} * L_g(4\xi^2, m, n-m), \quad \text{for } m < n \tag{24}$$

where L_g is the associated Laguerre polynomial and $\xi = (q_\nu^0 - q_\mu^0)/\sqrt{2\omega_c}$ with $q_\nu^0 = \frac{\boldsymbol{\lambda}}{\omega_c}\cdot\boldsymbol{\mu}_{\nu\nu}$. This basis is expected (and has been explicitly shown for models systems[61]) to efficiently converge the photonic basis, especially when the permanent dipoles $\mu_{\nu\nu}$ in the MH basis are large. For additional discussion on the PFS basis, see Ref. 61. Further, a similar basis has been used in the quantum optics and recently in the polariton communities, which is referred to as the generalized coherent state (GCS) basis,[62;63;41;64] which also relies on the molecular dipole information to define a new photonic basis. The polaritonic Hamiltonian in the PFS basis is, in general, not as sparse as that of the adiabatic-Fock matrix (see Eq. 19) since all shifted Fock states between different MH electronic states ϕ_ν are connected via their shifted harmonic oscillator overlaps, so sparse matrix techniques cannot be as readily applied. The main advantage of the PFS basis is that many of the overlaps will be near zero due to the widely varying magnitudes of the molecular dipole $\mu_{\nu\nu}$ elements. In this way, the PFS basis, in principle, will allow one to use many fewer shifted Fock states as a basis than the vacuum Fock states used in the adiabatic-Fock basis (see Section 3.1.1) and therefore may perform more efficiently in many cases. More rigorous testing is required for real, *ab initio* molecular systems where the dipole matrices are extremely non-diagonal in the many-state adiabatic basis compared to many of the tested model systems, such as the harmonic oscillator or the double-well potentials where the dipole matrix is nearly diagonal, hence the adiabatic states are already almost equal to the MH states themselves. In our experience, the photonic basis is more easily converged in *ab initio* systems compared to the convergence of the electronic basis, which often requires many states to provide a useful convergence (see Sec. 3.2 for additional discussion).

Fig. 2 presents the polariton potential energy surfaces predicted by various quantum optics model Hamiltonians for the model LiF molecule shown in Fig. 2a-b (the details of the model can be found in Ref. 61). Here, only two diabatic states were considered, which are denoted as the ionic state $|\text{I}\rangle$, and covalent state $|\text{C}\rangle$. These two diabatic states are coupled through a diabatic coupling $V_{\mathrm{IC}}(R)$ (dotted yellow line in Fig. 2a) that causes a splitting (avoided crossing) near the anti-crossing of the diabatic potentials $V_{\mathrm{C}}(R)$ and $V_{\mathrm{I}}(R)$ (solid red and blue line in Fig. 2a, respectively). The adiabatic electronic states, ground $|\mathrm{G}(R)\rangle$ and excited $|\mathrm{E}(R)\rangle$ states can be obtained by diagonalizing the electronic Hamiltonian $\hat{H}_{\mathrm{el}} = V_{\mathrm{I}}(R)|\mathrm{I}\rangle\langle\mathrm{I}| + V_{\mathrm{C}}(R)|\mathrm{C}\rangle\langle\mathrm{C}| + V_{\mathrm{IC}}(R)(|\mathrm{I}\rangle\langle\mathrm{C}| + |\mathrm{C}\rangle\langle\mathrm{I}|)$ at each R (see Eq. 12).

The electronic dipole matrix at each R is diagonal in this diabatic representation. This is because the diabatic states $|\mathrm{I}\rangle$ and $|\mathrm{C}\rangle$, also referred to as the Mulliken-Hush diabatic states, are by definition the eigenstates of the electronic transition dipole operator (see discussion around Eq.10). Fig. 2b presents the matrix elements of $\hat{\boldsymbol{\mu}}$ in both the diabatic (solid lines) and the adiabatic (dashed lines) representations. As expected, the permanent dipole for the ionic state $|\mathrm{I}\rangle$ (corresponding to $\mathrm{Li^{+}F^{-}}$) $\mu_{\mathrm{I}}(R)$ linearly increases, while the permanent dipole for the $|\mathrm{C}\rangle$ state (corresponding to covalently bonded Li-F) $\mu_{\mathrm{C}}(R)$ remains nearly zero with increasing interatomic separation R. The adiabatic states switch their characters around $R \approx 13.5$ a.u., as a result, the adiabatic permanent dipole switches in that region, and $\mu_{eg}(R)$ peaks at $R \approx 13.5$ a.u.

Fig. 2c shows the polaritonic potential energy surfaces for a cavity frequency $\omega_{\mathrm{c}} = 1.5$ eV and light-matter coupling strength $A_0 = 0.127$ a.u. The coloring indicates the average photon number of the polaritonic state. Given an initial excitation from $|\mathrm{G}(R), 0\rangle \rightarrow |\mathrm{E}(R), 0\rangle$ (vertical black arrow) at the ground state minimum (outside the cavity's influence), the time-dependent average photon number was calculated (see Ref.[61] for more details) and shown in Fig. 2d. Thus, through nuclear motion and light-matter coupling, excited photons can be generated.

3.1.3 | Calculating Relevant Polaritonic Properties

Exciton-polaritons have many characteristic features, such as the Rabi splitting observed in linear spectroscopy when the cavity frequency is in resonance with a well-separated electronic transition (*e.g.* historically found in single-atom spectroscopy). Of course, there are many spectroscopic footprints of polariton formation that are of interest to the community for finding and exploring the physics of such quasi-particles; however, the spectroscopic results available experimentally may not be the most informational for probing local phenomena such as chemical reactions, charge transfer, or exciton diffusion. In these examples, the main features are stored in the excitonic part of the polariton, which is usually not directly visible in most experimental configurations due to the fast photon loss mechanisms and mirror absorption. However, examining the photonic contribution to the spectroscopy will give *indirect* information regarding the changes to the excitonic part of the polaritonic wavefunctions. In this section, we will outline the necessary steps to compute observables of polaritonic states using the direct diagonalization approach already discussed. We will focus on the local excitonic changes due to the formation of hybrid light-matter states, which are *directly* relevant to the local chemical reactivity, excited-state charge transfer, and exciton diffusion processes.

Any polaritonic observable $\hat{O}$ can be described with any basis of light and matter, *e.g.* adiabatic-Fock (Section 3.1.1), PFS (Section 3.1.2), or any other. Note that this is a more general case than was done in Eq. 21. Here, we will choose the adiabatic-Fock basis for conceptual simplicity, but all of the main points are easily transferable to another basis by unitary transformation. The matrix elements of the polaritonic observable $\hat{O}$ can be expanded in the adiabatic-Fock basis (Eq. 20) as,

$$\langle\Phi_j|\hat{O}|\Phi_k\rangle = \sum_{\alpha\beta}^{N_{el}}\sum_{nm}^{N_F} C^{j}_{\alpha n} C^{k}_{\beta m}\langle\psi_\alpha, n|\hat{O}|\psi_\beta, m\rangle = \sum_{\alpha\beta}^{N_{el}}\sum_{nm}^{N_F} C^{j}_{\alpha n} C^{k}_{\beta m}\langle\psi_\alpha|\hat{A}_{\mathrm{el}}|\psi_\beta\rangle\langle n|\hat{B}_{\mathrm{ph}}|m\rangle, \tag{25}$$

where $C^{k}_{\beta m} = \langle\psi_\beta, m|\Phi_k\rangle$. Note here that since the polaritonic Hamiltonian, Eq. 15, is real-valued, then the expansion coefficients in the adiabatic-Fock or PFS basis will also be real-valued, *i.e.*, $(C^{k}_{\beta m})^{*} = C^{k}_{\beta m}$. In general, any polaritonic

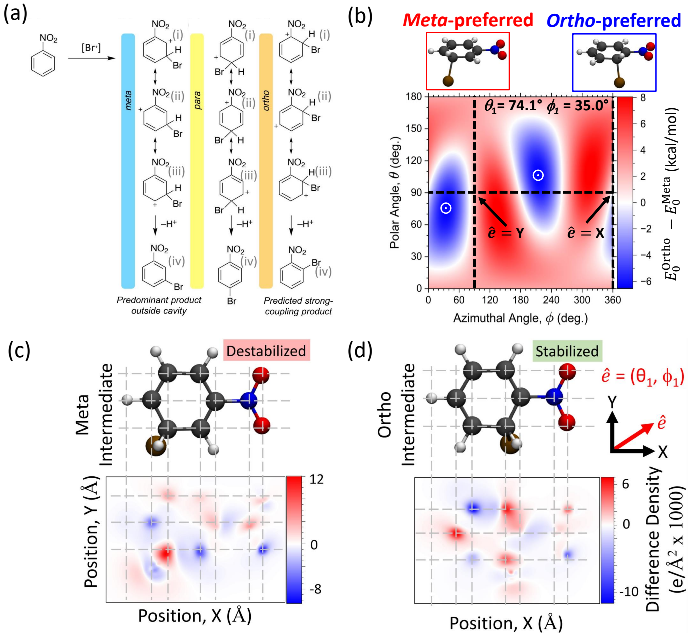

FIGURE 3 (a) Schematic of possible reaction pathways of theelectrophilic bromination of nitrobenzene. (b) Relative energy of the polaritonic ground states between *ortho*-$PhNO_2$- Br^+ and *meta*-$PhNO_2$- Br^+ intermediates with various cavity polarization directions. Ground state density difference between coupling to the cavity and outside the cavity case, for (c) the *meta*-cationic intermediate and (d) the *ortho*-cationic.

observable, even restricting to ground-to-excited elements, are linear combinations of *all* matrix elements present in the electronic and photonic subs-systems. As such, highly non-trivial mixing of matrix elements can appear when the light-matter coupling becomes large. Here $\hat{O} = \hat{A}_{\text{el}} \otimes \hat{B}_{\text{ph}}$ are factorized electronic and photonic operators, respectively, which is not a requirement of $\hat{O}$ but is often the case for simple, non-entangled observables, such as the average photon number $\hat{O} = \hat{\mathcal{I}}_{\text{el}} \otimes \hat{a}^\dagger \hat{a}$.[65] Another example is linear spectroscopy where the polaritonic dipole matrix elements can be expressed as $\hat{\mu}_{\text{pol}} \sim \hat{\mu}_{\text{el}} \otimes \hat{\mathcal{I}}_{\text{ph}} + \hat{\mathcal{I}}_{\text{el}} \otimes \hat{q}_{\text{c}}$. In experiment, the relative magnitudes of the excitonic and photonic contributions are highly dependent on the experimental configuration and are usually understood to be dominated by the photonic contributions (*i.e.*, keeping only the $\hat{q}_{\text{c}}$ term in $\hat{\mu}_{\text{pol}}$) and is often called the "visibility spectrum" or "transmission spectrum".[66] In this case, the local information regarding the excitonic spectrum is present only in an *indirect* sense. However, often one is interested in examining the changes to the excitonic subsystem for purposes of exploring electronic reorganization through the mixing of electronic adiabatic states via hybridization with light.[39;37;63;40;67;68;17;69;70] As such, to achieve an observable that will give direct information on the excitonic subsystem, we will ignore the second term in the polaritonic dipole operator to exclude photonic contribution, and in this way, we have traced out the photonic DOFs. An arbitrary matter-projected polaritonic operator can now be written as,

$$\hat{O}^{\text{M}}_{jk} = \langle \Phi_j | \hat{A}_{\text{el}} \otimes \hat{\mathcal{I}}_{\text{ph}} | \Phi_k \rangle = \sum_{\alpha\beta}^{N_{el}} \sum_{n}^{N_F} C^j_{\alpha n} C^k_{\beta n} \langle \psi_\alpha | \hat{A}_{\text{el}} | \psi_\beta \rangle, \tag{26}$$

where we have made use of the orthogonality of the vacuum Fock states, $\langle n|m\rangle = \delta_{nm}$. For example, one may be interested in the polaritonic transition density[39;71;37] $\rho^{\mathrm{M}}_{0j}(\mathbf{r})$ (see Eq. 21) or the polaritonic difference density[40;17;41] $\Delta\rho(\mathbf{r}) = \rho^{\mathrm{M}}_{jj} - \xi_{jj}$ of the molecule inside the cavity.

With the pQED approach, textbook organic reactions can be studied. Several theoretical studies have recently shown[17;19] that the cavity can *completely switch selectivity of well-known chemical reactions*. If successful, cavity QED could revolutionize fundamental knowledge of organic chemistry. One such reaction is the electrophilic bromination of nitrobenzene[17] shown in Fig. 3a. This is a textbook reaction,[72;73] where only the *meta*-substitution product is possible, and the *ortho*-substituted (or *para*-substituted) product is not observed experimentally. This has been well-explained due to the stability of the catatonic active complex $\mathrm{PhNO_2}$-$\mathrm{Br^+}$, for example, using the resonance structure or using *ab initio* calculations. By coupling this reaction to an optical cavity which mixes the character of the ground and excited electronic states, it was observed that one can fundamentally change the selectivity of this reaction, making the *ortho*-substituted product possible. Fig. 3b presents the relative energy difference between the meta-substituted and the ortho-substituted catatonic active complex $\mathrm{PhNO_2}$-$\mathrm{Br^+}$, where the blue region of the figure indicates where the *meta*-substitution is more stable, and red region of the figure indicates where the *ortho*-substitution is more stable. Fig. 3c,d presents the ground state density difference ($\Delta\rho(\mathbf{r})$, defined below Eq. 26 using Eq. 21) for the *meta*- and *ortho*-substituted intermediate coupled inside the cavity and outside the cavity. This density difference aids in the understanding of the cavity QED effects on modified relative energies of the intermediate species. This observable has a close connection with the intuitive resonance structure arguments, since the difference density shows how the electronic distribution is modified by the presence of the cavity.[17] As such, coupling to the cavity cavity enables ortho-substituted nitro-benzene, thus making impossible reactions possible. Additionally, Ref. 17 predicts that the experimental condition for this change requires the cavity frequency of $\omega_{\mathrm{c}} = 1.8$ eV and the filed intensity of $2 - 10$ V/nm, both of which can be accomplished with the state-of-the-art plasmonic cavity designs.[25;26;74]

3.2 | Iterative Approaches

In the previously discussed QED approach, one is required to compute the many-body electronic states $\{|\psi_\alpha\rangle\}$ for use in a direct diagonalization procedure of the Pauli-Fierz Hamiltonian (Eq. 18) coupled with some basis for the photonic DOFs (*e.g.*, Fock/number states, polarized Fock states) to arrive at a description of the polaritonic states in these choices of basis. This method, in the infinite basis limit, provides the exact results for the polaritonic states, capturing the exact correlation between the electronic and photonic DOFs. The primary limitation of this approach is that the electronic basis converges very slowly for strong light-matter coupling strengths, requiring the calculation of highly excited electronic states (~100) to converge even the lowest polaritonic energies.[38;37] Contrary to this, the photonic basis only requires a relatively small number of basis states to converge for realistic, *ab initio* systems.[37;17]

Due to this limitation of the direct diagonalization approach, the community seeks other approximations in line with previous electronic structure approaches that now include the photonic interactions to some degree to arrive at a self-consistent description of the problem. In principle, this approach will require many fewer basis states than a single, direct diagonalization but with similar approximations for the electron-photon and photon-photon interactions that are intrinsic to the many-body method of choice. In this way, these approaches will be able to capture the cases where strong light-matter coupling is too strong to utilize the direct diagonalization approach with a frozen basis. We define these self-consistent analogues to the commonly used electronic structure approaches as scQED-X, where X can be any of the standard approaches, such as Hartree-Fock theory (HF),[41;64;63;68] density functional theory (DFT), linear response time-dependent DFT (LR-TD-DFT),[75;76;39] coupled cluster (CC),[41;64;40;67] configuration interaction (CI),[63;77] full configuration interaction (FCI),[78], second-order Møller–Plesset perturbation theory (MP2),[79] and density matrix renormalization group (DMRG).[80]

3.2.1 | Generalized Coherent State Transformation

In a similar manner as done in the construction of the polarized Fock states in Sec. 3.1.2, the generalized coherent state (GCS) transformation is a specific instance of polarizing the photonic basis by a parameter proportional to the molecular dipole moment. The GCS basis has been used in many recent works exploring the self-consistent solution to the ground polaritonic state.[41;64;40;68] The unitary transformation can be written as,

$$\hat{U}_{\text{GCS}} = e^{\mathcal{Z}\hat{a}^{\dagger} - \mathcal{Z}^{*}\hat{a}}, \tag{27}$$

where the GCS shift parameter $\mathcal{Z}$ is chosen to be,

$$\mathcal{Z} = -\frac{\boldsymbol{\lambda} \cdot \langle \hat{\boldsymbol{\mu}} \rangle_{\text{GS}}}{\sqrt{2\omega_{\text{c}}}}, \tag{28}$$

where $\langle \hat{\mu} \rangle_{\text{GS}}$ is the expectation value of the molecular dipole in the ground state. For this choice of GCS parameter, one can rewrite the Pauli-Fierz Hamiltonian, $\hat{U}^{\dagger}_{\text{GCS}}\hat{H}_{\text{pl}}\hat{U}_{\text{GCS}} = \hat{H}^{\text{GCS}}_{\text{pl}}$,

$$\hat{H}^{\text{GCS}}_{\text{pl}} = \hat{H}_{\text{el}} + \hbar\omega_{\text{c}}\big(\hat{a}^{\dagger}\hat{a} + \frac{1}{2}\big) + \sqrt{\frac{\omega_{\text{c}}}{2}}(\boldsymbol{\lambda} \cdot \Delta\hat{\boldsymbol{\mu}})(\hat{a}^{\dagger} + \hat{a}) + \frac{1}{2\hbar}(\boldsymbol{\lambda} \cdot \Delta\hat{\boldsymbol{\mu}})^2, \tag{29}$$

in terms of the deviation of the molecular dipole from its expectation value in the ground state $\Delta\hat{\boldsymbol{\mu}} = \hat{\boldsymbol{\mu}} - \langle \hat{\boldsymbol{\mu}} \rangle_{\text{GS}}$ and its variance $(\Delta\hat{\boldsymbol{\mu}})^2$. In the following section (Sec. 3.2.2), we will see that $\langle \Delta\hat{\boldsymbol{\mu}} \rangle_{\text{SD}} = 0$ for many-body methods that employ only a single-determinant (SD) wavefunction, such as Hartree-Fock (SD→HF) or density functional (SD→DFT) theories, allowing for a drastic simplification of the coupled electron-photon Hamiltonian. Note that contributions from the dipole self-energy survive, since $\langle (\Delta\hat{\boldsymbol{\mu}})^2 \rangle_{\text{SD}} = \langle \hat{\boldsymbol{\mu}}^2 \rangle_{\text{SD}} - \langle \hat{\boldsymbol{\mu}} \rangle^2_{\text{SD}}$, even with a single determinant approach.

It is important to note that simply using the GSC transformation does not yield a fully origin invariant Fock matrix or single-particle orbital energies. Ref. 68 discusses such drawbacks and proposes the so-called strong coupling variant of the Hartree-Fock theory (SC-QED-HF), which transforms the Pauli-Fierz Hamiltonian in a similar way as the GSC rotation but now contains orbital specific rotations, similar to the polarized Fock state basis (see Sec. 3.1.2). Since the orbitals are involved and the transformation depends on the dipole operator, the single-particle Hamiltonian is first rotated to the dipole basis (similar to Eq. 12 but for single-particle molecular orbitals instead of many-body states).

Furthermore, one should note that this choice of $\mathcal{Z}$ (Eq. 28) or the case of SC-QED-HF in Ref. 68 only applies in the limit of infinite light-matter coupling. Recent works have performed a variational optimization procedure on the shift parameter $\mathcal{Z}$, *e.g.*, choosing $\mathcal{Z}_{\text{OPT}}$ under the condition $\frac{\partial \mathcal{E}(\mathbf{R})}{\partial \mathcal{Z}} = 0$, which further minimizes the energy of the ground state.[79;81] This minimization is done on top of the self-consistent iterations and can be interpreted as an additional DOF for the self-consistent procedure. Given this rotation of the Hamiltonian, both the DSE as well as the bilinear interaction term would remain, even for single-determinant approaches, but would be scaled (or partially shifted away) by some optimal factor proportional to $\Delta\lambda = \lambda - \mathcal{Z}_{\text{OPT}}$ and $(\Delta\lambda)^2$, respectively. This partial transformation can be interpreted as a rotation that pushes the maximal amount of complicated many-body electron-photon and photon-mediated electron-electron correlations into the mean-field solution of the QED problem.

3.2.2 | Single-determinant Ground Polaritonic States

Assuming a single-reference (*i.e.*, single-determinant) wavefunction for the electronic DOFs $|\mathrm{HF}\rangle$ (taken as Hartree-Fock determinant) for the polaritonic ground state in the GCS basis (see Sec. 3.2.1), then the deviation in the molecular dipole $\Delta\hat{\boldsymbol{\mu}} = \hat{\boldsymbol{\mu}} - \langle\hat{\boldsymbol{\mu}}\rangle_{\mathrm{GS=HF}} = 0$ since $\langle\mathrm{HF}|\hat{\boldsymbol{\mu}}|\mathrm{HF}\rangle = \langle\hat{\boldsymbol{\mu}}\rangle_{\mathrm{GS=HF}}$, effectively removing the bilinear coupling term in the GCS light-matter Hamiltonian (Eq. 29). However, the DSE term remains since $\langle(\Delta\hat{\mu})^2\rangle_{\mathrm{HF}} \neq 0$ even for the single-determinant approximation. To be clear, for approaches with multiple determinants (*i.e.*, the use of excited Slater determinants in a CIS-like expansion), the direct coupling term will survive. For a single-reference ground state, Eq. 29 can then be simplified to,

$$\hat{H}_{\mathrm{pl}}^{\mathrm{GCS}} = \hat{H}_{\mathrm{el}} + \hbar\omega_{\mathrm{c}}\big(\hat{a}^{\dagger}\hat{a} + \frac{1}{2}\big) + \frac{1}{2\hbar}(\boldsymbol{\lambda}\cdot\Delta\hat{\boldsymbol{\mu}})^2, \tag{30}$$

where the only photonic operator that appears is that of the photonic Hamiltonian $\hat{H}_{\mathrm{ph}} = \hbar\omega_{\mathrm{c}}\big(\hat{a}^{\dagger}\hat{a} + \frac{1}{2}\big)$ whose eigenstates are the vacuum Fock states $|\tilde{n}\rangle$ in the rotated GCS basis (which have the same frequency but with a shift in position q_{c} by $\mathcal{Z}$ compared to the vacuum Fock states). One should note that the Pauli-Fierz Fock states can be re-obtained by applying the reverse unitary coherent state transformation $\hat{U}_{\mathrm{GCS}}$ (Eq. 27) to the resulting Fock states after the self-consistent solution (discussed below) of Eq. 30 has been achieved, whose average photon number will depend on the self-consistent solution of the dipole moment $\langle\hat{\boldsymbol{\mu}}\rangle_{\mathrm{HF}} = 0$. suggesting that molecules with strong ground-state dipole moments will exhibit stronger polaritonic effects.[40;82]

The ground polaritonic state can be defined as the $|\mathrm{HF},\tilde{0}\rangle$ wavefunction. Neglecting the photonic zero-point energy (*i.e.*, $\langle\tilde{0}|\hat{H}_{\mathrm{ph}}|\tilde{0}\rangle = \frac{\hbar\omega_{\mathrm{c}}}{2}$), the electron-photon Fock matrix can be written as,

$$\mathcal{F}_{pq} = \mathcal{F}_{pq}^{\mathrm{HF}} + \frac{1}{2\hbar}\Big[\sum_{o}^{N_{\mathrm{occ}}}(\boldsymbol{\lambda}\cdot\boldsymbol{\mu}_{po})(\boldsymbol{\lambda}\cdot\boldsymbol{\mu}_{oq}) - \sum_{v}^{N_{\mathrm{vir}}}(\boldsymbol{\lambda}\cdot\boldsymbol{\mu}_{pv})(\boldsymbol{\lambda}\cdot\boldsymbol{\mu}_{vq})\Big], \tag{31}$$

where o, v, and (p,q) are occupied, virtual, and any molecular orbitals, respectively. Noting that the solution to the bare molecular Fock matrix is achieved if $\mathcal{F}_{ov}^{\mathrm{HF}} = 0$, the scQED-HF energy can be written as,[41]

$$E_{\mathrm{QED-HF}} = E_{\mathrm{HF}} + \frac{1}{2\hbar}\langle(\boldsymbol{\lambda}\cdot\Delta\hat{\boldsymbol{\mu}})^2\rangle_{\mathrm{HF}} = E_{\mathrm{HF}} + \frac{1}{\hbar}\sum_{ov}(\boldsymbol{\lambda}\cdot\boldsymbol{\mu}_{ov})^2, \tag{32}$$

which is then variationally minimized in a self-consistent way, updating the coherent shift $\mathcal{Z}$ at each iteration. More details on the scQED-HF scheme in varying complexity can be found in Refs. 41, 68, and 63.

Following a similar procedure, the single-determinant nature of density functional theory can be used to simplify the Pauli-Fierz Hamiltonian to that of the GSC representation without the direct coupling term. However, due to the *ad hoc* nature of density functional theory, there are many ways to approximate the exchange-correlation kernel to arrive at various levels of corrections to the electron-electron, electron-photon, and photon-photon correlations. In fact, the simplest choice (albeit the least motivated) is to ignore the electron-photon and photon-photon terms in the exchange-correlation kernel. In this case, the only responses of the single-particle orbitals $\{p, q\}$ are those induced by the dipole self-energy contributions (the last term in Eq. 31). This is the simplest approach since no novel exchange-correlation functionals need to be used/created, and one can rely on the already-developed, high-level functionals for the complicated electron-electron correlation, such as CAM-B3LYP[83], ωB97XD[84;85], and SCAN.[86;87] Recently, novel exchange-correlation functionals for electronic and photonic DOFs have been constructed based on a variety of frameworks, such as the optimized effective potential (OEP) approach,[88;89] photon-free effective Hamiltonians,[90] and the fluctuation-dissipation theorem approach.[91] In any case, the ground state energy can be loosely written as

$$E_{\mathrm{QED-DFT}} = E_{\mathrm{DFT}} + E^{\mathrm{el-ph}}_{\mathrm{ex-corr}} + E^{\mathrm{ph-ph}}_{\mathrm{ex-corr}}, \tag{33}$$

where the last two terms (or more specifically the exchange-correlation functionals of the density $E[\rho]$), in addition to the first term for standard DFT, are not known explicitly and must be approximated.[92] Note that a fraction of Hartree-Fock exchange can still be included in the electron-electron exchange term within E_{DFT}. For more details, we refer the reader to the original references regarding density functional theory, Refs. 89, 90, and 91, as well as others who have explored and utilized similar Hartree-Fock[63;68;40;93;41;64] and density functional theories for electron-photon systems.[58;39;71;88;91;94;95;96;75;97;98;99;100;101;102;103;104]

3.2.3 | Addressing Correlations and Excited States

Capturing higher-order correlations between electrons has a well-defined procedure using post-HF approaches, such as configuration interaction (CI) or coupled cluster (CC) expansions in the basis of excited Slater determinants. The polaritonic community has also used such wavefunction approaches for computing the polaritonic electronic-bosonic states[41;64;40;67;63;36;105;69;81;70] in addition to other approaches such as time-dependent DFT (TD-DFT),[70;82;75;39;97;71;89;99] reduced density matrix (RDM) theory,[106] quantum Monte Carlo,[107] Møller-Plesset Theory (MP-n),[79] and density matrix renormalization group (DMRG).[108;109;110;80] While mean-field approaches (*e.g.*, HF, DFT) yield useful ground state information, even in the absence of correlation, it is not yet clear to what extent the correlated excitations of the matter and photonic DOFs will impact the results, even in the ground polaritonic state. Further, the need for polaritonic excited states is ubiquitous in the photophysics and photochemistry of excited polaritons. Additionally, the determination of the light-matter coupling strength is often predicated on the magnitude of the Rabi splitting between the light and matter excitations at resonance. While our goal is not to outline all possible many-body approaches which go beyond mean-field, we will briefly outline and discuss QED coupled cluster theory (QED-CCSD) since in the electronic structure community coupled cluster theory is one of the most widely used approximations for capturing electronic correlation in a wide variety of molecules.

The CC ansatz for the ground-state polaritonic wavefunction is[41;78]

$$|\mathcal{E}_0^{\mathrm{CC}}\rangle = e^{\hat{\mathcal{T}}}|\mathcal{E}_0^{\mathrm{HF}}\rangle = e^{\hat{\mathcal{T}}}\big[|\psi^{\mathrm{HF}}\rangle \otimes |0\rangle_{\mathcal{Z}}\big], \tag{34}$$

where $|\mathcal{E}_0^{\mathrm{HF}}\rangle$ is the polaritonic ground state calculated at the uncorrelated HF level (see Eq. 32) and $|\psi^{\mathrm{HF}}\rangle$ is the uncorrelated HF electronic ground state. Here, $|0\rangle_{\mathcal{Z}}$ is the photon vacuum state in the rotated coherent state representation with $|0\rangle_{\mathcal{Z}} = \hat{U}_{\mathcal{Z}}|0\rangle$ (see Eq. 27) at the optimal coherent state parameter $\mathcal{Z}$ after the HF self-consistent procedure. $\hat{\mathcal{T}}$ is the cluster operator (not to be confused with the kinetic energy operator $\hat{T}_{\mathrm{R}}$ or $\hat{T}_{\mathrm{r}}$ in Eq. 1). This cluster operator involves a sum of electronic, photonic, and mixed electron-photon excitations as follows

$$\hat{\mathcal{T}} = \sum_{\alpha} t_{\alpha}\hat{\tau}_{\alpha} + \sum_{n} t_n\hat{\tau}_n + \sum_{\tilde{\alpha},\tilde{n}} t_{\tilde{\alpha}\tilde{n}}\hat{\tau}_{\tilde{\alpha}\tilde{n}}, \tag{35}$$

where $\hat{\tau}_{\alpha}$ represents creation and annihilation operators for an α_{th}-order electronic excitation. For example, with $\alpha = 1$ (single electronic excitation), $\hat{\tau}_i^a = \hat{c}_a^{\dagger}\hat{c}_i$ excites an electron from an occupied orbital i to an unoccupied orbital a. Similarly, $\alpha = 2$ implies $\hat{\tau}_{ij}^{ab} = \hat{c}_a^{\dagger}\hat{c}_b^{\dagger}\hat{c}_i\hat{c}_j$ which will excite two electrons $i \rightarrow a$ and $j \rightarrow b$, respectively. The photon excitation operator is commonly written as the standard photonic ladder operator $\hat{\tau}_n = (\hat{a}^{\dagger})^n$.[40;41] It should be noted that this is not the only way to define the bosonic excitations. The authors of Ref. 78 defined an idempotent form of the excitation operator as $\hat{\tau}_n = |n\rangle\langle 0|$ for a finite number of Fock states $\{|n\rangle\} = \{|0\rangle, |1\rangle, ..., |N_\mathrm{F}\rangle\}$. However, the two cases are not formally equivalent, and a rigorous comparison of the quality of the results has not been performed. In a similar manner, the coupled electron-photon excitation operator $\hat{\tau}_{\tilde{\alpha}\tilde{n}}$ can be written, for example, as $\hat{c}_a^\dagger \hat{c}_i (\hat{a}^\dagger)^n$ for a one-electron electronic excitation coupled to an n_th-level photonic excitation while $\hat{c}_a^\dagger \hat{c}_b^\dagger \hat{c}_i \hat{c}_j (\hat{a}^\dagger)^n$ will provide the two-electron and n_th-level photonic coupled excitations. Each of these excitation operators is connected with a unique cluster amplitude $\{t_\alpha, t_n, t_{\tilde{\alpha},\tilde{n}}\}$.

The amplitudes t_α, t_n, and $t_{\tilde{\alpha}\tilde{n}}$ can be solved by projection (Eq. 36). This requires the evaluation of the similarity-transformed Hamiltonian operator $\hat{\bar{H}}_\mathrm{PF} = e^{-\hat{\mathcal{T}}} \hat{H}_\mathrm{PF} e^{\hat{\mathcal{T}}}$, where $\hat{H}_\mathrm{PF}$ is expressed in Eq. 13 and is usually rotated to the coherent state basis (see Sec. 3.2.1). This leads to the ground state coupled cluster energy $\mathcal{E}_0^\mathrm{CC}$ as a solution to the following set of equations,

$$\langle \mathcal{E}_0 | \hat{\bar{H}} | \mathcal{E}_0 \rangle = \mathcal{E}_0^\mathrm{CC}, \quad \{\mathcal{L}_\Gamma\} = \langle \mathcal{E}_{\{\Gamma\}} | \hat{\bar{H}} | \mathcal{E}_0 \rangle = 0, \tag{36}$$

with $|\mathcal{E}_{\{\Gamma\}}\rangle = \hat{\tau}_{\{\Gamma\}} |\mathcal{E}_0^\mathrm{HF}\rangle$, where $\{\Gamma\} = \{\alpha, n, \tilde{\alpha}\tilde{n}\}$ is the set of possible excitations in the cluster operator $\hat{\mathcal{T}}$ (Eq. 35) leading to the set of projection equations $\{\mathcal{L}_\Gamma\}$. These projections lead to the equations for the excitation amplitudes $t_{\{\Gamma\}}$ and are usually solved in a self-consistent manner. A similar CC projection formalism can be found in any electronic structure textbook.[111]

There are many different notations for the methods developed by changing the highest level of excitation for each term in the cluster operator. The most straightforward notation is CCSD-n-jm, which implies that the electronic DOFs are treated up to double (SD) excitations in the cluster operator, the photonic excitation is limited to n levels, and the mixed excitation is set to j electronic and m photonic. As per usual CC theory, the cutoff value of the excitation levels leads to effects that include even higher excitations through the exponential treatment of the cluster operator $\hat{\mathcal{T}}$, thus effectively outperforming similar methods such as CI with the same excitation level cutoff. However, due to the $\mathcal{O}(N^6 * N_\mathrm{F}^{N_\mathrm{mode}})$ scaling (with N electrons/basis functions and N_modes cavity modes each with N_F Fock states) of the scQED-CC method in general, including more than two Fock states has been a challenge even for small molecular systems,[40;112;18;41] and limited study has been performed including up to 10 Fock states for a half-filled four-site Hubbard model with direct comparison to the full configuration interaction result.[78] This will have unfavorable scaling on multi-mode cavities with quasi-continuous dispersion relations (where $N_\mathrm{mode} > 10$). Nevertheless, QED-CCSD remains one of the most accurate approaches for simulating *ab initio* polaritons.[107]

4 | POLARITON QUANTUM DYNAMICS

In this section, we address and outline various approaches to simulate the quantum dynamics of polaritons at various levels of theory. The essential task is trying to solve the time-dependent Schrödinger equation (TDSE)

$$i\hbar \frac{\partial}{\partial t} |\Psi(t)\rangle = \hat{H}_\mathrm{PF} |\Psi(t)\rangle, \tag{37}$$

where $|\Psi(t)\rangle$ is the total quantum state of the electronic-nuclear-photonic hybrid system. The time-evolution of such a system is governed by the Pauli-Fierz QED Hamiltonian $\hat{H}_\mathrm{PF}$ (Eq. 13). Depending on this complexity of the molecular system, one may perform the dynamics exactly as dictated by the TDSE (which may be prohibitively expensive for more than a few nuclear DOFs) or resort to various approximations, such as mixed quantum-classical (MQC) approaches, semi-classical approaches, various approximate master equation approaches (*e.g.*, Lindblad, Redfield, etc.), or approximate wavefunction approaches (*e.g.*, multi-configurational Hartree-Fock). In the following discussion, we will briefly introduce an exact method for solving polariton quantum dynamics (Sec. 4.1) as well as a few popular mixed quantum-classical approaches (Sec. 4.2). Additionally, we will address the calculation of the exact nuclear gradients and their effects on the quantum dynamics (Sec.4.3).

4.1 | Exact Polaritonic Quantum Dynamics

We begin by briefly discussing how to solve Eq. 37 exactly, thus giving an exact solution to the polaritonic quantum dynamics. There are, in principle, many possible strategies for exact quantum dynamics propagation, and we only outline one of the most commonly used strategies based on the Born-Huang expansion[113] and subsequent propagation in the energy basis. We describe the total wavefunction of the electron-photon-nuclear DOFs using the adiabatic-Fock basis as,

$$|\Psi\rangle = \sum_{\xi}^{\mathcal{N}_{\mathrm{G}}} \sum_{\alpha}^{\mathcal{N}_{\mathrm{el}}} \sum_{n}^{\mathcal{N}_{\mathrm{F}}} \chi_{\alpha n}(\mathbf{R}_{\xi})\, |\mathbf{R}_{\xi}\rangle \otimes |\psi_{\alpha}(\mathbf{R}_{\xi})\rangle \otimes |n\rangle, \tag{38}$$

where $\chi_{\alpha n}(\mathbf{R}_{\xi}) = \langle \mathbf{R}_{\xi}, \psi_{\alpha}, n|\Psi\rangle = \big(\langle \mathbf{R}_{\xi}| \otimes \langle \psi_{\alpha}(\mathbf{R}_{\xi})| \otimes \langle n|\big)|\Psi\rangle$ is the $\xi\alpha n_{\mathrm{th}}$ expansion coefficient and $\mathcal{N}_{\mathrm{G}}$ is the number of grid points for the nuclear basis set in a grid or spectral basis (*e.g.*, discrete variable representation).[114] Here $\{|\psi_{\alpha}(\mathbf{R})\rangle\}$ are the electronic adiabatic states at nuclear configuration $\mathbf{R}$, $\{|n\rangle\}$ are the photonic Fock states, and $\{|\mathbf{R}_{\xi}\rangle\}$ are the basis functions of the grid describing the nuclear DOFs.

Within this representation, the matrix elements of the total light-matter Hamiltonian $\hat{H}_{\mathrm{PF}} = \hat{T}_{\mathrm{R}} + \hat{H}_{\mathrm{pl}}$ are written as,

$$(\hat{T}_R + \hat{H}_{\mathrm{pl}})_{\xi\xi',\alpha\beta,nm} = (\hat{T}_R)_{\xi\xi',\alpha\beta}\delta_{nm} + (\hat{\mathcal{H}}_{\mathrm{pl}})_{\alpha\beta,nm}(\mathbf{R}_{\xi})\delta_{\xi\xi'} \tag{39}$$

$$(\hat{T}_R)_{\xi\xi',\alpha\beta} = -\frac{1}{2}\sum_{a}^{N_R}\frac{1}{M_a}\Big[\langle \mathbf{R}_{\xi}|\nabla_a^2|\mathbf{R}_{\xi'}\rangle\delta_{\alpha\beta} + 2\mathbf{d}_{\alpha\beta}^{a}(\mathbf{R}_{\xi})\cdot\langle \mathbf{R}_{\xi}|\nabla_a|\mathbf{R}_{\xi'}\rangle + D_{\alpha\beta}^{a}(\mathbf{R}_{\xi})\delta_{\xi\xi'}\Big] \tag{40}$$

$$(\hat{\mathcal{H}}_{\mathrm{pl}})_{\alpha\beta,nm}(\mathbf{R}_{\xi}) = \Big[E_{\alpha}(\mathbf{R}_{\xi}) + \hbar\omega_{\mathrm{c}}(n+\frac{1}{2})\Big]\delta_{\alpha\beta}\delta_{nm} + \tilde{\mu}_{\alpha\beta}(\mathbf{R}_{\xi})\eta_{nm} + \mathcal{D}_{\alpha\beta}(\mathbf{R}_{\xi})\delta_{nm}, \tag{41}$$

where the individual terms in $\hat{H}_{\mathrm{pl}}$ (*i.e.*, $\tilde{\mu}_{\alpha\beta}$, η_{nm}, and $\mathcal{D}_{\alpha\beta}$) were defined previously in Eq. 18. Additionally, $\mathbf{d}_{\alpha\beta}^{a}(\mathbf{R}_{\xi}) = \langle\psi_{\alpha}|\nabla_a|\psi_{\beta}\rangle$ is the non-adiabatic coupling and $D_{\alpha\beta}^{a}(\mathbf{R}_{\xi}) = \langle\psi_{\alpha}|\nabla_a^2|\psi_{\beta}\rangle$ is the second-derivative coupling, which were defined in Eqs. 4 and 5, respectively. N_R is the number of nuclear DOFs in the system. We refer the reader to Ref. 114 and Ref 115 for evaluating quantities (*e.g.*, the nuclear kinetic energy) using the grid or spectral basis for the nuclear DOFs.

Upon diagonalization of this Hamiltonian $\hat{H}_{\mathrm{PF}} = \hat{T}_{\mathbf{R}} + \hat{H}_{\mathrm{pl}}$ (Eq. 39), the electronic-nuclear-photonic eigenstates can be obtained as,

$$\hat{H}_{\mathrm{PF}}|\mathcal{E}_p\rangle = (\hat{T}_R + \hat{H}_{\mathrm{pl}})|\mathcal{E}_p\rangle = \mathcal{E}_p|\mathcal{E}_p\rangle. \tag{42}$$

The electronic-nuclear-photonic wavefunction can then be propagated in time as,

$$|\Psi(t)\rangle = \mathrm{e}^{-i\hat{H}_{\mathrm{PF}}t}|\Psi(t=0)\rangle = \sum_{p} c_p \mathrm{e}^{-i\mathcal{E}_p t}|\mathcal{E}_p\rangle, \tag{43}$$

where $\mathcal{E}_p$ is the p_{th} eigenvalue and c_p is the projection onto initial total wavefunction onto the p_{th} eigenstate $|\mathcal{E}_p\rangle$,

$$c_p = \langle \mathcal{E}_p | \Psi(t=0) \rangle, \tag{44}$$

where $|\Psi(t=0)\rangle$ is an arbitrary initial condition (in the same form as Eq. 38). Additional details on the exact propagation can be found in Refs. 116, 117, and 59.

There are many ways in which to evaluate the exact (or approximately exact) dynamics of a quantum mechanical system in addition to the one outlined above, which may be one of the simplest to write down. However, other approaches exist, such as the Multi-configuration time-dependent Hartree (MCTDH),[118;119;120;60;121], the exact factorization (XF)[11;122], the hierarchical equation of motion (HEOM)[123;124], etc., which have been already used for exploration in polaritonic systems. Additionally, *ab initio* multiple spawning (AIMS),[125;126] Ehrenfest multiple cloning (EMC),[127;69] and their variants[128;129;130] could also be adapted for polaritonic dynamics to give nearly exact results.

4.2 | Trajectory-based Approaches

In lieu of an exact propagation of the total wavefunction, including electron, photon, *and* nuclear DOFs as quantum mechanical DOFs, we now move to a discussion of Mixed Quantum-Classical (MQC) and Semi-classical approaches. These methods are trajectory-based schemes of varying complexity and accuracy in the sense that the nuclear (and in some cases photonic) distribution is now composed of an ensemble of trajectories in order to compute observables over the entire nuclear (and/or photonic) initial distribution as ensemble averages. Further, usually the trajectories are taken to be completely independent of one another, aside from the initial nuclear distribution, with some recent exceptions of the coupled-trajectory approaches and quasi-coupled trajectories approaches stemming from the exact factorization scheme.[131;132;133;134]

Two schemes exist for applying the MQC approach: (I) treating the nuclear *and* photon DOFs classically or (II) treating *only* the nuclear DOFs classically. While both approaches will yield interesting results, we will focus on scheme (II) where the photon is treated fully quantum mechanically. In the following two sections, we will briefly outline two approaches commonly used in the quantum dynamics, namely the mean-field Ehrenfest and fewest switches surface hopping.

4.2.1 | Mean-field Ehrenfest

Ehrenfest (EH) dynamics is a MQC approach for propagating the coupled electron-photon-nuclear dynamics.[135;136;127] We choose to treat the electronic and photonic DOFs as fully quantum mechanical while treating the nuclear DOFs as classical ones. In this way, we can write the total wavefunction (Eq. 38) in an approximate form, including only the electronic and photonic DOFs explicitly and the nuclear DOFs as parameters as,

$$|\Psi(t)\rangle = \sum_{\alpha}^{\mathcal{N}_{\text{el}}} \sum_{n}^{\mathcal{N}_{\text{F}}} c_{\alpha n}(t) |\psi_\alpha(\mathbf{R}(t)), n\rangle, \tag{45}$$

where $c_{\alpha n}(t) = \langle \psi_\alpha(\mathbf{R}(t)), n | \Psi(t) \rangle$ is the αn_{th} time-dependent, adiabatic-Fock expansion coefficient, $|\psi_\alpha(\mathbf{R}(t))\rangle$ is the α_{th} electronic adiabatic wavefunction parameterized by the nuclear positions at time t, $\mathbf{R}(t)$, and $|n\rangle$ is the time-independent photonic Fock state. The time-dependent electronic-photonic wavefunction $|\Phi(t)\rangle$ is evolved by approximating the time-dependent Schrödinger equation (TDSE), $i\frac{\partial}{\partial t}|\Psi(t)\rangle = \hat{H}_{\text{PF}}|\Psi(t)\rangle$ (see Eqs. 13 and 18), as the following set of differential equations for the expansion coefficients in the adiabatic-Fock basis,

$$\dot{c}_{\alpha n}(t) = -i\epsilon_{\alpha,n} c_{\alpha n}(t) - \sum_{\beta}^{N_{\text{el}}} \Big[\frac{d\mathbf{R}(t)}{dt} \cdot \mathbf{d}_{\alpha\beta}(\mathbf{R}(t)) - i\mathcal{D}_{\alpha\beta} \Big] c_{\beta n}(t) - i \sum_{\beta}^{N_{\text{el}}} \sum_{m}^{N_{\text{F}}} \tilde{\mu}_{\alpha\beta}\, \eta_{nm}\, c_{\beta m}(t) \tag{46}$$

Here, $\mathbf{d}_{\alpha\beta}(\mathbf{R}(t)) = \langle \psi_\alpha(\mathbf{R}(t)) | \nabla_R | \Psi_\beta(\mathbf{R}(t)) \rangle$ is the derivative coupling (Eq. 4) and $\frac{d\mathbf{R}(t)}{dt}$ is the classical nuclear velocity. The matrix elements $\epsilon_{\alpha,n}$, $\tilde{\mu}_{\alpha\beta}$, η_{nm}, and $\mathcal{D}_{\alpha\beta}$ were defined previously in Eq. 18. To achieve this expression, one assumes that the second-derivative couplings are vanishingly small and that the nuclear distribution is sharply peaked around its average position. Additionally, we have made use of the orthogonality of the vacuum Fock states, $\langle n|m \rangle = \delta_{nm}$ as well as noting that the nuclear gradient does not act on the photonic basis states (*i.e.*, $\langle n|\nabla_{\mathbf{R}}|m\rangle = 0$) since they do not depend on the nuclear positions **R**. This non-dependency of the photonic basis states leads to a large amount of sparsity in the matrices, and as noted earlier in Section 3.1.1, sparse matrix methods could be employed to achieve more efficient calculations. Note that this is not true, for example, when employing the PFS photonic basis (Section 3.1.2), where the definition of the photonic basis states relies on the nuclear positions through the use of the molecular dipole operator.[61]

In order to propagate the classical nuclear DOFs, the classical-like force is simply the sum of all contributions from the elements of the reduced density matrix, $\rho_{\alpha n,\beta m}(t) = c^*_{\alpha,n}(t) c_{\beta,m}(t)$. In this way, the force can be written as,

$$\mathbf{F}(t) = -\langle \Psi(\mathbf{R}(t)) | \nabla_{\mathbf{R}} \hat{H}_{\text{pl}} | \Psi(\mathbf{R}(t)) \rangle = -\sum_{\alpha\beta}^{N_{\text{el}}} \sum_{nm}^{N_{\text{F}}} \rho_{\alpha n,\beta m}(t)\, \langle \psi_\alpha(\mathbf{R}(t)), n | \nabla_{\mathbf{R}} \hat{H}_{\text{pl}} | \Psi_\beta(\mathbf{R}(t)), m \rangle, \tag{47}$$

where the nuclear gradients on the Hamiltonian $\nabla_{\mathbf{R}} \hat{H}_{\text{pl}}$ will be discussed in detail in Sec. 4.3. For a similar description in terms of the polaritonic basis, see Ref. 36.

4.2.2 | Linearized Spin-mapping

In the fully linearized spin-mapping framework,[137;138;139;140] any electronic-only, two-operator correlation function can be written as,

$$C_{AB}(t) = \langle\, A_{\text{W}}(\mathbf{Z}(0))\; B_{\text{W}}(\mathbf{Z}(t))\, \rangle_{\text{spin-LSC}} \tag{48}$$

where A_{W} (F_{W}) is the Stratonovich-Weyl (SW) transform of operator $\hat{A}$ ($\hat{B}$). The measurement of an arbitrary operator at time t can be written as,

$$[\hat{B}]_{\text{W}}(Z,t) \equiv B_{\text{W}}(Z(t)) = \text{Tr}[\hat{B}\, \hat{\omega}_{\text{W}}(Z(t))]. \tag{49}$$

The SW kernel can be written as,

$$\hat{\omega}_{\text{W}}(Z,t) = \frac{1}{2} \sum_{\alpha\beta}^{N_{\text{el}}} \sum_{nm}^{N_{\text{F}}} \Big(Z_{\alpha n}(t) Z^*_{\beta m}(t) - \gamma_{\text{W}} \delta_{\alpha\beta} \delta_{nm} \Big) |\psi_\alpha, n\rangle\langle\psi_\beta m|, \tag{50}$$

in a diabatic basis for the N_{pol} polaritonic states. The SW kernel is evaluated as a function of the complex-valued, time-evolved mapping variables $\mathbf{Z} = \{Z_1, Z_2, ..., Z_{N_{\text{pol}}}\}$ with a *fixed* zero-point energy parameter $\gamma_{\text{W}} = \frac{2}{N_{\text{pol}}}(\sqrt{N_{\text{pol}}+1} - 1)$.

It should be noted that the approach outlined here is one of many realizations for spin-mapping dynamics. In this work, we focus on the so-called spin-mapping dynamics confined to the W-sphere, which shows the most accurate results for the widest variety of systems.[137;138;141;142;143]

The correlation function for the time-evolved density matrix $\rho_{\alpha n,\beta m}$, given an initial excitation to state arbitrary state σl (*i.e.*, $\hat{A} = |\sigma l\rangle\langle\sigma l|$ in Eq. 48) is evaluated using focused initial conditions such that,

$$\rho_{\alpha n,\beta m}(t) \approx \int d\mathbf{R}\, d\mathbf{P}\, d\mathbf{Z}\, \rho_{\mathrm{b}}(\mathbf{R},\mathbf{P})\, \rho_{\mathrm{W}}^{(\sigma l)}\, \left[|\psi_\alpha n\rangle\langle\psi_\beta m|\right]_{\mathrm{W}}(\mathbf{Z}(t))), \tag{51}$$

where $\rho_{\mathrm{b}}(\mathbf{R},\mathbf{P})$ is the Wigner distribution for the nuclear DOFs, and $\rho_{\mathrm{W}}^{(\sigma l)}$ is the initially focused distribution for the mapping variables,

$$\rho_{\mathrm{W}}^{(\sigma l)} = \frac{\delta(|Z_{\sigma l}|^2 - \gamma_{\mathrm{W}} - 2)\Pi_{\alpha n \neq \sigma l}\delta(|Z_{\alpha n}|^2 - \gamma_{\mathrm{W}})}{\int dZ\, \delta(|Z_{\sigma l}|^2 - \gamma_{\mathrm{W}} - 2)\Pi_{\alpha n \neq \sigma l}\delta(|Z_{\alpha n}|^2 - \gamma_{\mathrm{W}})}. \tag{52}$$

For a given initial state σl, the mapping variables Z are initialized as,

$$\begin{aligned} Z_{\sigma l} &= \sqrt{2+\gamma_{\mathrm{W}}}\;\; e^{i\theta_{\sigma l}} \quad && \text{(Initially focused state)} \\ Z_{\alpha n} &= \sqrt{\gamma_{\mathrm{W}}}\;\; e^{i\theta_{\alpha n}}, && \alpha n \neq \sigma l \end{aligned} \tag{53}$$

with $\{\theta\}$ randomly sampled between 0 and 2π, independently from one another.

The propagation of the mapping and nuclear variables can be done identically to Eq. 47 with the state-dependent forces $F_e(\mathbf{R},\mathbf{Z})$,

$$F_e(\mathbf{R},\mathbf{Z}) = -\frac{1}{2}\sum_{\alpha\beta}^{\mathcal{N}_{\mathrm{el}}}\sum_{nm}^{\mathcal{N}_{\mathrm{F}}} \rho_{\alpha n,\beta m}\langle\psi_\alpha, n|\nabla_{\mathbf{R}}\hat{H}_{\mathrm{pl}}(\mathbf{R})|\psi_\beta, m\rangle. \tag{54}$$

with

$$\rho_{\alpha n,\beta m} = \frac{1}{2}(Z^*_{\alpha,n}(t)Z_{\beta,m}(t) - \gamma_{\mathrm{W}}\delta_{\alpha\beta}\delta_{nm}). \tag{55}$$

For more details on the linearized spin mapping approach, we refer the reader to Refs. 137, 138, and 140. We also want to point out extensions of the spin mapping approach to partially linearized methods[144;140;145;146] as well as a recently developed surface hopping-inspired spin mapping formalism.[147;148;149]

4.2.3 | Surface Hopping

We now move to an alternative description of mixed quantum classical treatment of the dynamics known as Fewest Switches Surface Hopping (FSSH), which is one of many variants of the surface hopping.[150;151] This method approaches the problem in a more classical way, propagating the nuclei on a single adiabatic surface until a discontinuous hop is performed. Once a hop is achieved, which must satisfy energy conservation through a rescaling of the classical nuclear velocities, then the nuclear forces are now derived from the new adiabatic state. The electronic DOFs are propagated according to the Schrodinger equation, and the probabilities for hopping between adiabatic states are proportional to the first-order non-adiabatic couplings $\mathbf{d}_{\alpha\beta}$ between adiabatic states. This approach has also been recently used to simulate polariton chemistry.[27;152;77;28;153;116;154]

It is well-known that surface hopping approaches perform better when the propagation is done in the adiabatic (*i.e.*, polariton) basis. However, many "tricks" exist to propagate the quantum mechanical DOFs in a locally diabatic basis for higher accuracy and to work around the sharply peaked non-adiabatic couplings throughout the nuclear dynamics. The total wavefunction for the quantum mechanical DOFs (*i.e.*, the electrons and photons) can be written as,

$$|\Psi(t)\rangle = \sum_{j}^{\mathcal{N}_{\mathrm{pol}}} c_j(t)|\Phi_j(\mathbf{R}(t))\rangle, \tag{56}$$

where $c_j(t) = \langle\Psi(t)|\Phi_j(\mathbf{R}(t))\rangle$ is the time-dependent expansion coefficient for polaritonic state j and $\mathcal{N}_{\mathrm{pol}}$ is the number of polaritonic states. During the nuclear dynamics, the active polaritonic state S dictates the nuclear forces, which can be written as,

$$\mathbf{F}(t) = -\langle\Phi_{\mathrm{S}}(\mathbf{R}(t))|\nabla_{\mathbf{R}}\hat{H}_{\mathrm{pl}}|\Phi_{\mathrm{S}}(\mathbf{R}(t))\rangle = -\nabla_{\mathbf{R}}\mathcal{E}_{\mathrm{S}}(\mathbf{R}(t)). \tag{57}$$

At each nuclear time-step Δt, the probability to hop from the current active polaritonic state S to any other polaritonic state j is computed as,

$$\mathcal{P}_{\mathrm{S}\to j}(t) = \mathrm{MAX}\Big[-\frac{\sigma_{\mathrm{S}j}(t)}{\rho_{\mathrm{SS}}(t)}, 0\Big], \tag{58}$$

with,

$$\sigma_{\mathrm{S}j}(t) = 2\mathrm{Re}\big[\rho_{\mathrm{S}j}(t)\big]\frac{d\mathbf{R}(t)}{dt}\cdot\mathbf{d}_{\mathrm{S}j}(\mathbf{R}(t)). \tag{59}$$

Here, $\mathbf{d}_{\mathrm{S}j}(\mathbf{R}(t))$ is the non-adiabatic coupling between polaritonic states, $\frac{d\mathbf{R}(t)}{dt} = \dot{\mathbf{R}}(t)$ are the classical nuclear velocities, and $\rho_{\mathrm{S}j}(t) = c_{\mathrm{S}}^*(t)c_j(t)$ is the reduced density matrix in the polaritonic basis. Between nuclear time-steps, the electronic DOFs are updated via direct propagation of the time-dependent Schrodinger equation as,

$$\dot{c}_j(t) = -iE_j(\mathbf{R}(t))c_j(t) - \sum_{k}^{\mathcal{N}_{\mathrm{pol}}} c_k(t)\,\dot{\mathbf{R}}(t)\cdot\mathbf{d}_{jk}(\mathbf{R}(t)). \tag{60}$$

It is well known[151] that FSSH suffers from producing overly coherent results (or, equivalently, a lack of proper decoherence between quantum states) within the expansion electronic coefficients and will subsequently be problematic for the polaritonic coefficients.[151] Many *ad hoc* corrections exist to modify the expansion coefficients in FSSH to account for decoherence, such as the instantaneous decoherence correction (IDC),[155;127] the energy-based decoherence correction (EDC),[156] etc., as well as other forms of the surface hopping scheme, such as the augmented surface hopping (A-FSSH),[157] the decoherence-induced surface hopping (DISH),[158] and the global flux surface hopping[159] schemes. More recently, a spin-mapping[145;144;140;137;138;139;160;141;142;143] analogue of the surface hopping approach was constructed and mitigates much of the shortcomings of the standard FSSH procedure without *ad hoc* adjustments.[147;148]

A major simplicity afforded by the FSSH method is that the derivative coupling vectors $\mathbf{d}_{jk}(\mathbf{R}(t))$ are not explicitly required as the nuclear forces (unlike in the mean-field MQC methods) do not require this quantity for time-evolution of the electronic or nuclear DOFs except at the hops for the nuclear velocity rescaling. To be clear, the electronic propagation only requires the scalar non-adiabatic coupling terms $\mathbf{d}_{jk}(\mathbf{R}(t)) \cdot \dot{\mathbf{R}}(t) = \langle \Psi_j | \frac{d}{dt} | \Psi_k \rangle$, which can be easily obtained via finite difference wavefunction overlaps of the polaritonic states throughout the trajectory.[161;162] This procedure is drastically cheaper than the direct computation of the non-adiabatic coupling vectors themselves, as one only needs to compute the non-adiabatic coupling vectors to rescale the nuclei at the moment of a hop.[155] Further, one can ignore the asymmetric nuclear velocity rescaling altogether and perform uniform energy-based rescaling, which is known to provide slightly worse dynamics but alleviates the computation of the vector non-adiabatic couplings altogether, providing a substantial speed-up in *ab initio* simulations. It is also worth mentioning that the first-order non-adiabatic couplings of the electronic subsystem $\mathbf{d}_{\alpha\beta}(\mathbf{R}(t))$ can be approximated using the scalar non-adiabatic coupling and the diagonal gradients.[163;164]

4.3 | Exact QED Nuclear Gradients

In the aforementioned mean-field, MQC Ehrenfest approach as well as other mean-field approaches not discussed here,[144;140;138;165;166] the nuclear force is written as a weighted average over the reduced density matrix involving both the diagonal gradients of the adiabatic states as well as the off-diagonal non-adiabatic couplings (see Eq. 47). Here, $\boldsymbol{\nabla}_\mathbf{R} \hat{H}_\mathrm{pl}$ is,

$$\boldsymbol{\nabla}_\mathbf{R} \hat{H}_\mathrm{pl} = \boldsymbol{\nabla}_\mathbf{R} \hat{H}_\mathrm{el} + \sqrt{\frac{\omega_\mathrm{c}}{2}} \lambda (\hat{a}^\dagger + \hat{a}) \boldsymbol{\nabla}_\mathbf{R} \hat{\mu} + \frac{\lambda^2}{2} \boldsymbol{\nabla}_\mathbf{R} \hat{\mu}^2. \tag{61}$$

Note here that the matrix elements of $\boldsymbol{\nabla}_\mathbf{R} \hat{H}_\mathrm{ph}$ are zero in the adiabatic-Fock basis and that the matrix elements of $\boldsymbol{\nabla}_\mathbf{R} \hat{H}_\mathrm{el}$ will lead to the usual electronic gradient of the adiabatic PESs, $\boldsymbol{\nabla}_\mathbf{R} E_\alpha(\mathbf{R})$, as well as the non-adiabatic couplings, $\mathbf{d}_{\alpha\beta}(\mathbf{R})$ (Eq. 4). Additional terms arise in the nuclear force that are proportional to the gradient on the molecular dipole matrix elements $\nabla_\mathbf{R} \hat{\mu}$, and these terms may contribute large amounts to the nuclear force in regions of large light-matter coupling λ.

Using the chain rule,[116] the matrix elements of the nuclear gradient operator for the a_th nuclear DOF acting on the polaritonic Hamiltonian can be written as,

$$[\nabla^a \hat{H}_\mathrm{pl}] = \nabla^a [\hat{H}_\mathrm{pl}] - [\hat{H}_\mathrm{pl}][\hat{d}^a] + [\hat{d}^a][\hat{H}_\mathrm{pl}] \equiv \nabla^a [\hat{H}_\mathrm{pl}] + X^a, \tag{62}$$

where $[\nabla^a \hat{H}_\mathrm{pl}]$, $[\hat{H}_\mathrm{pl}]$ and $[d^a]$ are the matrix representations (in the adiabatic-Fock basis) of $\nabla^a \hat{H}_\mathrm{pl}$, $\hat{H}_\mathrm{pl}$, and the non-adiabatic coupling operators, respectively, along the a_th nuclear DOF, and we have defined the matrix

$$X^a \equiv [\hat{d}^a][\hat{H}_\mathrm{pl}] - [\hat{H}_\mathrm{pl}][\hat{d}^a]. \tag{63}$$

Note that $[\hat{d}^a]$ is the same as that of Eq. 4 but in the full electron-photon Hilbert space as $\hat{d} \otimes \hat{\mathcal{I}}_\mathrm{ph}$. As a concrete example, for a polaritonic system composed of two electronic adiabatic states $\{|\mathrm{g}\rangle, |\mathrm{e}\rangle\}$ and two photonic Fock states $\{|0\rangle, |1\rangle\}$, the 4×4 gradient matrices can be written explicitly, with the $\nabla^a [\hat{H}_\mathrm{pl}]$ expressed as,

$$\nabla^a [\hat{H}_\mathrm{pl}] = \begin{bmatrix} \nabla^a (E_g + \mathcal{D}_{gg}) & \nabla^a \mathcal{D}_{ge} & \nabla^a \tilde{\mu}_{gg} & \nabla^a \tilde{\mu}_{ge} \\ \nabla^a \mathcal{D}_{eg} & \nabla^a (E_e + \mathcal{D}_{ee}) & \nabla^a \tilde{\mu}_{eg} & \nabla^a \tilde{\mu}_{ee} \\ \nabla^a \tilde{\mu}_{gg} & \nabla^a \tilde{\mu}_{ge} & \nabla^a (E_g + \mathcal{D}_{gg}) & \nabla^a \mathcal{D}_{ge} \\ \nabla^a \tilde{\mu}_{eg} & \nabla^a \tilde{\mu}_{ee} & \nabla^a \mathcal{D}_{eg} & \nabla^a (E_e + \mathcal{D}_{ee}) \end{bmatrix}, \tag{64}$$

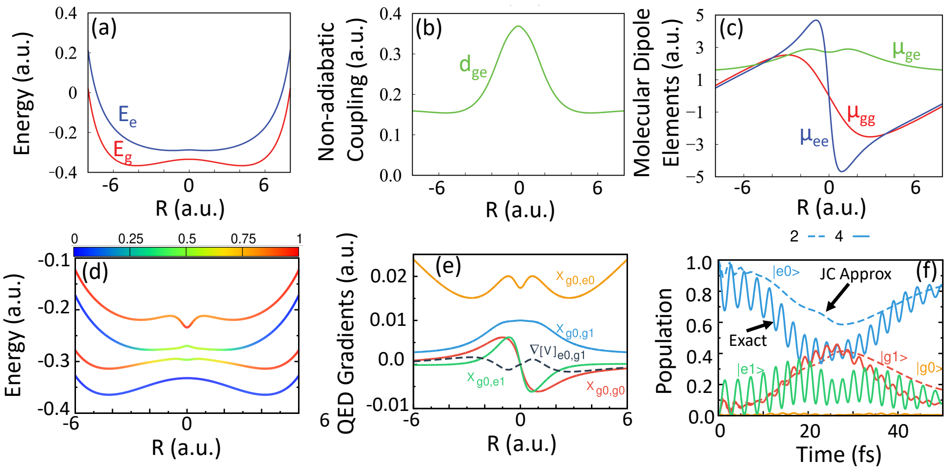

FIGURE 4 (a) Two-state, one-dimensional Shin-Metiu (SM) model along with the (b) non-adiabatic coupling matrix element d_{ge} element and (c) dipole matrix elements $\mu_{\text{gg}}, \mu_{\text{ge}}, \mu_{\text{ee}}$ as functions of the nuclear coordinate R (d) SM model coupled to an optical cavity of frequency ω_{c} = 0.1 a.u. and coupling strength A_0 = 0.05 a.u. using a highly truncated basis of two electronic states $\{|\text{g}\rangle, |\text{e}\rangle\}$ and two photonic Fock states $\{|0\rangle, |1\rangle\}$ The average photon number in the length gauge $\langle \hat{a}^\dagger \hat{a}\rangle$ is shown with the colorbar, where $\langle \hat{a}^\dagger \hat{a}\rangle = 0.0$ represents purely electronic character. (e) Various contributions to the nuclear gradient as functions of nuclear position R. (f) Exact quantum solution for the population dynamics using the approximate (dashed curves) gradient at the Jaynes-Cummings level (*i.e.* with completely uncoupled $|\text{g}, 0\rangle$ and basis $|\text{e}, 1\rangle$ states) and the Pauli-Fierz gradient (solid curves).

and $[X^a]$ as,

$$[X^a] = \begin{bmatrix} 2d^a_{ge}\mathcal{D}_{eg} & d^a_{ge}(E_e - E_g + \mathcal{D}_{ee} - \mathcal{D}_{gg}) & 2d^a_{ge}\tilde{\mu}_{ge} & d^a_{ge}\left(\tilde{\mu}_{ee} - \tilde{\mu}_{gg}\right) \\ d^a_{ge}(E_e - E_g + \mathcal{D}_{ee} - \mathcal{D}_{gg}) & 2d^a_{eg}\mathcal{D}_{eg} & d^a_{ge}\left(\tilde{\mu}_{ee} - \tilde{\mu}_{gg}\right) & 2d^a_{eg}\tilde{\mu}_{ge} \\ 2d^a_{ge}\tilde{\mu}_{ge} & d^a_{ge}\left(\tilde{\mu}_{ee} - \tilde{\mu}_{gg}\right) & 2d^a_{ge}D_{eg} & d^a_{ge}(E_e - E_g + \mathcal{D}_{ee} - \mathcal{D}_{gg}) \\ d^a_{ge}\left(\tilde{\mu}_{ee} - \tilde{\mu}_{gg}\right) & 2d^a_{eg}\tilde{\mu}_{ge} & d^a_{ge}(E_e - E_g + \mathcal{D}_{ee} - D_{gg}) & 2d^a_{eg}\mathcal{D}_{eg} \end{bmatrix}. \tag{65}$$

Note that $\tilde{\mu}_{\alpha\beta} \equiv \omega_{\text{c}} A_0 (\hat{e}\cdot\boldsymbol{\mu}_{\alpha\beta})$ and $\mathcal{D}_{\alpha\beta} = \omega_{\text{c}} A_0 \sum_\gamma^{\mathcal{N}_{\text{el}}} (\hat{e}\cdot\boldsymbol{\mu}_{\alpha\gamma})(\hat{e}\cdot\boldsymbol{\mu}_{\gamma\beta})$, where $\mathcal{N}_{\text{el}}$ is the number of electronic adiabatic states (*i.e.*, $\mathcal{N}_{\text{el}} = 2$ in this example), as defined in Eq. 18. For additional details regarding the nuclear gradients, we refer to interested reader to Ref. 116 and Ref. 154. These nuclear gradients have been the hardest hurdle to overcome in performing on-the-fly simulations with realistic, *ab initio* systems, since the nuclear gradients on the molecular dipole are not widely available analytically.[167] However, some recent work has been done in achieving MQC dynamics at the Jaynes-Cummings level (*i.e.*, without the dipole self-energy term and ignoring the highly oscillatory terms in the light-matter interaction Hamiltonian) through iterative schemes[28] or through the approximation of the gradient via a Taylor expansion.[168] However, for further theoretical advancement, the community requires work toward the efficient and analytic evaluation of these nuclear gradients to enable another theoretical leap in the simulation of polariton dynamics for realistic systems.

Fig. 4 presents an example of the effects of the nuclear gradients on the quantum dynamics of the system.[116] As before, the one-electron Shin-Metiu model is used and provides access to a realistic *ab initio* system, albeit simplified. Fig. 4a-c show the bare electronic properties, lowest two potential energy surfaces $E_\alpha(R)$, the non-adiabatic coupling $d_{\text{ge}}(R)$ (Eq. 4), and the molecular dipole matrix elements $\mu_{\alpha\beta}(R)$. Fig. 4d extends Fig. 4a to include the quantized

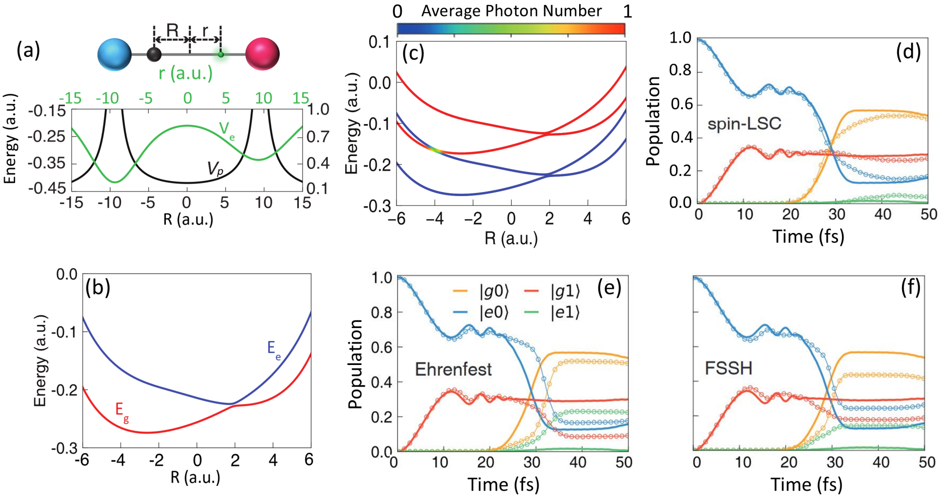

FIGURE 5 (a, top) Depiction of the one-electron Shin-Metiu model system, with two fixed nuclei (red and blue) of unit positive charge, one proton at position R (black), and one electron (green) at position r. (a, bottom) The potential energy of the proton V_p (black) and of the electron V_e (green). (b) The ground and first electronic states of the Shin-Metiu model system as functions of the proton position R, showcasing an avoided crossing near $R = 2.0$ a.u. (c) Polaritonic potential energy surfaces as a function of the proton coordinate R for two choices of light-matter coupling strength $A_0 = 0.01$ a.u. (d-f) Population dynamics for various MQC methods (d) spin-LSC, (e) Ehrenfest, and (f) FSSH. The initial conditions are $|\mathrm{e}, 0\rangle$ at the proton position $R = -4$ and for the same choice of light-matter coupling strength as panel (c). The exact results are shown in solid curves whereas the approximate MQC results are shown as circles. All polaritonic states were described in a truncated basis of two electronic states $|\mathrm{g}\rangle$ and $|\mathrm{e}\rangle$ and two photon vacuum states $|0\rangle$ and $|1\rangle$.

cavity photon in the four-state basis of $|\mathrm{g},0\rangle$, $|\mathrm{e},0\rangle$, $|\mathrm{g},1\rangle$, and $|\mathrm{e},1\rangle$. The colorbar indicates the average photon number $\langle \hat{a}^\dagger \hat{a}\rangle$. The gradients in this basis take the form of Eq. 62. Fig. 4e shows only a few of these matrix elements as a function of the nuclear coordinate. For example, the $\nabla[V]_{\mathrm{e}0,\mathrm{g}1} \equiv \nabla[H_\mathrm{pl}]_{\mathrm{e}0,\mathrm{g}1}$ is the off-diagonal gradient of the Hamiltonian shown in Eq. 64, and the other elements are of the quantity $X = [d][H_\mathrm{pl}] - [H_\mathrm{pl}][d]$ which relates to the cavity-mediated non-adiabatic couplings. Due to the light-matter couplings, the $|\mathrm{g},0\rangle$ and $|\mathrm{g},1\rangle$ are coupled through the gradient on the permanent dipole moment μ_gg as well as through the non-adiabatic coupling multiplied by the transition dipole moment μ_ge, in total, proportional to $\nabla\mu_\mathrm{gg}(R)+2d_\mathrm{ge}(R)\mu_\mathrm{ge}(R)$. This can be seen directly in the $X_{\mathrm{g}0,\mathrm{g}1}$ curve in Fig. 4e given that the permanent dipole moment μ_gg has a constant gradient near $R = 0.0$ and thus provides a plateau for $X_{\mathrm{g}0,\mathrm{g}1}$ in the same region. Most importantly, the redistribution of d_ge among all the basis states allows for a complex and interesting non-adiabatic events that would be absent without the light-matter coupling. Finally, Fig. 4e shows the quantum dynamics simulation using the exact nuclear gradients (solid curves, Eq. 62) in addition to showing the approximate population dynamics using the approximate gradients of the Jaynes-Cummings Hamiltonian in the $|\mathrm{e},0\rangle$, $|\mathrm{g},1\rangle$ subspace (dashed curves, see Ref. 116 for more details). Clearly, additional states beyond the JC subspace will be explored by the quantum dynamics of the hybrid system due to the NACs among these states. The population of the $|e1\rangle$ state is mainly contributed from the population transfer from the $|\mathrm{e}0\rangle$ state due to the light-matter coupling originating from the permanent dipole μ_ee. In addition, the population transition between $|\mathrm{e}0\rangle$ and $|\mathrm{g}1\rangle$ is mediated by the cavity-induced coupling near $R = 0.0$, where the PES exhibits a strong mixing between these two states as shown in Fig. 4d.

As a concrete example of the above-mentioned MQC dynamics applied to a "realistic *ab initio*" system, the authors of Ref. 154 explore the one-electron Shin-Metiu model system (shown in Fig. 5a). This model system is composed of four species: two heavy particles fixed-in-space (red and blue) with unit positive charge as well as a mobile and classical proton (black) and a quantum mechanical electron (green). Below the system, Fig. 5a shows the potential energy of the proton (black curve) as well as that of the electron (green curve) as a function of the proton coordinate R. For a detailed explanation of the parameters of this asymmetric Shin-Metiu model, we refer the interested reader to Ref. 154. The two lowest energy Born-Oppenheimer potential energy surfaces (*i.e.*, the ground and first excited adiabatic states), E_{g} and E_{e}, are shown in Fig. 5b, which exhibit an avoided crossing near $R = 2.0$ a.u.

Using these two electronic states as well as two photon number states, $|0\rangle$ and $|1\rangle$, as a basis, the four polaritonic Born-Oppenheimer surfaces were constructed at a light-matter coupling strength $A_0 = 0.01$ (Fig. 5c) with the curves colored by their average photon number, $\langle \hat{a}^\dagger \hat{a} \rangle$ (see colorbar). The cavity frequency is $\omega_{\mathrm{c}} = 0.1$ a.u. After vertical excitation from the $R = -4.0$ a.u. to the $|\mathrm{e}, 0\rangle$ basis state (*i.e.*, a linear combination of polaritonic states), the quantum dynamics of the system was performed using the (Fig. 5d) MQC spin-LSC, (Fig. 5e) MQC Ehrenfest, and (Fig. 5f) MQC FSSH approaches.[154] The MQC results are shown in circles while the exact results are shown as solid curves. For these MQC simulations, the exact nuclear gradient was implemented (as discussed in the previous section, Sec. 4.3) in order to compute the exact polaritonic nuclear force. At short times ($<$ 20 fs), the nuclear wavepacket starts in and quickly leaves the region of strong light-matter coupling, showcasing a fast decay in coherent oscillations from the light-matter coupling. At ~20 fs, the nuclear wavepacket crosses the electronic non-adiabatic region near $R = 2.0$ a.u. where much of the population decays to the total ground state, $|\mathrm{g}, 0\rangle$, before the simulation ends. In this example, spin-LSC MQC dynamics performs better than either Ehrenfest or FSSH. It should be noted here that FSSH can generally be improved by using various decoherence corrections.[156] Specifically, spin-LSC is able to capture the weak population of the $|\mathrm{e}, 1\rangle$ state (green) while Ehrenfest (and to a lesser extent FSSH) dramatically over-populates this state. Furthermore, Ehrenfest and FSSH do not accurately predict the electronic non-adiabtic crossing time, instead showing a delay of 5-10 fs.

5 | TOWARD REALISTIC POLARITONS

5.1 | Machine Learning

As pointed out in previous sections (*e.g.*, Sec. 4), performing trajectory-based *ab initio* polaritonic dynamics requires multiple properties of the molecular system, including the energy matrix, $(\hat{H})_{\alpha\beta}$, transition dipole matrix, $(\hat{\mu})_{\alpha\beta}$, and the nuclear gradients of both $(\nabla_{\mathbf{R}} \hat{H})_{\alpha\beta}$ and $(\nabla_{\mathbf{R}} \hat{\mu})_{\alpha\beta}$. The gradient on the energy leads to the usual state gradients $\nabla_{\mathbf{R}} E_\alpha$ as well as the first-order non-adiabatic couplings $\nabla_{\mathbf{R}} \mathbf{d}_{\alpha\beta}$ (Eq. 4). These non-adiabatic couplings may be analytically available in some electronic structure software, such as QCHEM,[169] MOLPRO,[170;171] NEXMD,[155] etc. but not all, and largely depend on the level of electronic structure itself. Further, the nuclear gradients of the transition dipole matrix elements, to our knowledge, is not implemented in an analytical form in any common electronic structure software.

With this current limitation in obtaining the exact polaritonic gradient (see Sec. 4.3), we turn toward the use of machine learning, which will allow one to train the molecular dipole as a function of the nuclear coordinates. Then the nuclear gradient can be obtained analytically from the gradient of the trained dipole function. One of the many possible techniques is the kernel ridge regression (KRR) scheme, which relies on supervised learning of the molecular dipole matrix and has been used in several recent works.[172;173;174] In this approach, the molecular property, $\mu^{x_k}_{\alpha\beta}(\mathbf{R})$ (the $\alpha\beta_{\mathrm{th}}$ matrix element of the transition dipole moment in the x_k^{th} spatial direction), is trained based on a function

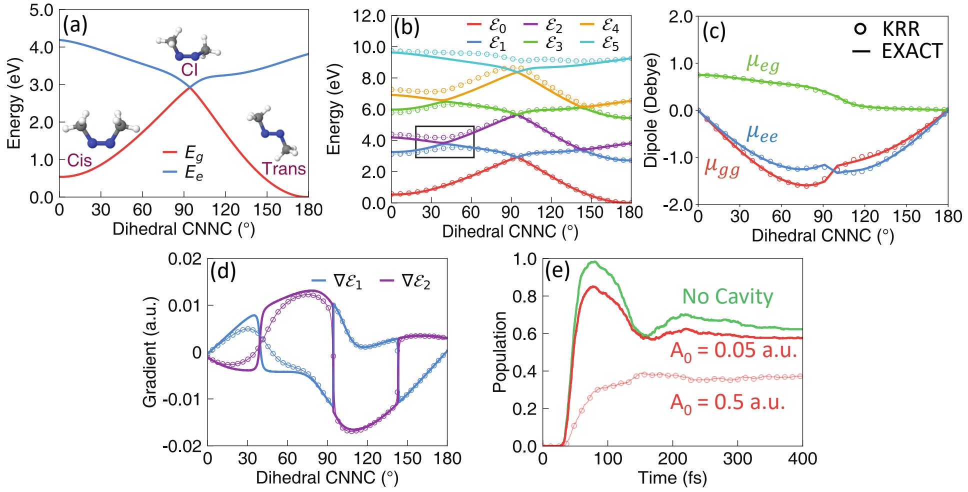

FIGURE 6 (a) Ground and first excited potential energy surface of bare azomethane as computed by CASSCF along its CNNC dihedral angle coordinate, showcasing a conical intersection (CI). (b) Polaritonic potential energy surfaces at light-matter coupling strength A_0 = 0.05 a.u. (solid curves) and A_0 = 0.5 a.u. (circles). (c) Dipole matrix elements along the CNNC dihedral coordinate and projected along the Y-axis of the molecule (perpendicular to the molecular plane) computed by CASSCF (solid curves) and the machine learning framework (open circes). (d) The nuclear gradient on the polariton potential energy surfaces. (e) Population dynamics at varying coupling strengths A_0 = 0.05 a.u. (red solid curve, middle) and A_0 = 0.5 a.u. (open circles, bottom) as well as outside the cavity (green, top).

of the nuclear coordinates which are represented by a molecular descriptor m such that,

$$\mu_{\alpha\beta}^{x_k}(m) = \sum_{s}^{\mathcal{N}_\mathrm{t}} w_s K(m, m^{(s)}), \qquad K(m, m^{(s)}) = e^{-\frac{|m-m^{(s)}|^2}{2\sigma^2}} \tag{66}$$

where $m^{(s)}$ is the molecular descriptor for the s_{th} nuclear configuration (with $\mathcal{N}_\mathrm{t}$ total training configurations), K is the Gaussian kernel function with w_s as the regression coefficient and σ as the width. This choice of kernel function is a radial basis function and only depends on the absolute distance between m and m_s with a single parameter σ. The coefficients w_s are trained by minimizing a cost function C defined as,

$$C \equiv \sum_{s}^{\mathcal{N}_\mathrm{t}} \left[\mu_{\alpha\beta}^{x_k}(m^{(s)}) - \mu_{\alpha\beta}^{\mathrm{ref}}(\mathbf{R})\right]^2 + \lambda \mathbf{W}^\mathrm{T}\mathbf{K}\mathbf{W}. \tag{67}$$

Here $\mu_{\alpha\beta}^{\mathrm{ref}}(\mathbf{R})$ is the reference molecular property value (often calculated numerically by finite-difference methods), λ is a Lagrange multiplier, and $\mathbf{W}$ is the matrix of regression coefficients. The choice of molecular descriptor m for the nuclear geometry can be one of many, but one of the simplest choices is the Coulomb matrix, $m_{\mathbf{R}_a \neq \mathbf{R}_b} = Z_{R_a} Z_{R_b}/|\mathbf{R}_b - \mathbf{R}_a|$ where $\mathbf{R}_a$ is the spatial coordinates of nucleus a and Z_a its nuclear charge. Once the dipole matrix elements are trained as a function of molecular descriptor, $\mu_{\alpha\beta}^{x_k}(m)$, the nuclear gradient can be obtained by the chain rule as,

$$\frac{\partial \mu_{\alpha\beta}^{x_k}(m)}{\partial R_a^{x_j}} = \sum_{l} \frac{\partial \mu_{\alpha\beta}^{x_k}(m)}{\partial m_l} \frac{\partial m_l}{\partial R_a^{x_j}}. \tag{68}$$

Here m_l is an element of the molecular descriptor and $R_a^{x_j}$ are the coordinated of nucleus a in the direction x_j. For additional details on using the KRR method for molecular properties in polaritonics, we refer the reader to Ref. 175.

Fig. 6 presents recent work[175] by Hu and Huo using the KRR approach to parameterize the transition and permanent dipoles of the azomethane molecule (Fig. 6a), which exhibits a conical intersection between the ground S_0 and excited S_1 electronic states as a function of the dihedral angle. Inside the cavity (Fig. 6b), the ground and excited states hybridize (black box) to form exciton-polaritons $\{\mathcal{E}_j\}$ with mixed electronic (primarily S_0 and S_1) and well as photonic character (primarily $n = 0$ and 1 vacuum Fock states). To perform the quantum dynamics simulations, the molecular dipole and its gradient were trained based on the KRR approach to yield the analytic dipole matrix elements, shown in Fig. 6c against the exact results using the CASSCF electronic structure method as the training/exact data. The total polaritonic gradient of the first $\nabla_{\mathbf{R}}\mathcal{E}_1$ and second $\nabla_{\mathbf{R}}\mathcal{E}_2$ excited polaritonic states is shown in Fig. 6d (see Eq. 64). Using these learned values, the quantum dynamics simulation of the photoisomerization of azomethane results are shown in Fig. 6e. Inside the cavity, at a small coupling strength of $A_0 = 0.05$ a.u., the avoided crossing between the first and second excited polaritonic states (black box in Fig. 6b) reduces the amount of product formed by the photo-reaction by bifurcating the wavepacket before reaching the conical intersection. At an increased coupling strength ($A_0 = 0.50$ a.u.), this effect is increased, reducing the overall population of the trans-product to less than 40% from the original product yield of 60% by increasing the population transfer at the polaritonic avoided crossing region.

5.2 | Simulating Cavity Loss with Trajectory Methods

Lindblad decay theory can be used to simulate the effects of photonic loss channels in semi-classical dynamics methods. The most general Markovian description of a dissipative environment (*i.e.*, modes external to the cavity) interacting with the electron-photon subsystem $\hat{\rho}(t)$ of interest that is both norm-preserving and always provides a positive-valued population is the Lindblad master equation. For the current problem, this can be written as,

$$\begin{aligned}\frac{d\hat{\rho}}{dt} &= -\frac{i}{\hbar}[\hat{H},\hat{\rho}] + \Gamma\left(\hat{L}\hat{\rho}\hat{L}^\dagger - \frac{1}{2}\{\hat{L}^\dagger\hat{L},\hat{\rho}\}\right)\\ &= \mathcal{L}_{\text{Coh.}}[\hat{\rho}] + \mathcal{L}_{\text{Diss.}}[\hat{\rho}]\end{aligned} \tag{69}$$

where $\hat{\rho}$ is the reduced density operator of the quantum subsystem including the electronic and photonic DOFs, $\hat{H}$ is the polaritonic Hamiltonian including the non-adiabatic terms, $\hat{L}$ is a Lindblad jump operator that mediates the dissipation due to an effective environment (*i.e.*, loss channel), Γ is the dissipation rate, $\{\hat{A},\hat{B}\} = \hat{A}\hat{B} + \hat{B}\hat{A}$ is the anti-commutator of matrices $\hat{A}$ and $\hat{B}$ and $[\hat{A},\hat{B}] = \hat{A}\hat{B} - \hat{B}\hat{A}$ is the commutator. $\mathcal{L}_{\text{Coh.}}$ and $\mathcal{L}_{\text{Diss.}}$ are super-operators in Liouville space which describe the quantum mechanical evolution of the electron-photon subsystem under the Hermitian Hamiltonian $\hat{H}$ which governs the coherent evolution of the system and $\hat{L}$ which governs the dissipation (*i.e.*, incoherent evolution). Lindblad dynamics ensure the conservation of the total population of the system. The Lindblad jump operator that governs the photon dissipation channel in Fabry-Perot cavities is defined as,

$$\hat{L} = \hat{\mathcal{I}}_{\text{el}} \otimes \hat{a} = \hat{\mathcal{I}}_{\text{el}} \otimes \sum_n^{N_{\text{F}}} \sqrt{n}|n-1\rangle\langle n|, \tag{70}$$

where $\hat{a}$ is the photonic annihilation operator and $\hat{\mathcal{I}}_{\text{el}}$ is the identity operator for the electronic subspace. This jump operator $\hat{L}$ facilitates population transfer from one photonic Fock state to the one below ($|n\rangle \rightarrow |n-1\rangle$) while also creating decoherence between the original state ($|n\rangle$) and all other states ($|m \neq n\rangle$).

The evolution of the reduced density matrix $\hat{\rho}$ in the Liouville space can be written as,

$$\hat{\rho}(t+dt) = \mathrm{e}^{(\mathcal{L}_{\mathrm{Coh.}}+\mathcal{L}_{\mathrm{Diss.}})dt}[\hat{\rho}(t)] \approx \mathrm{e}^{\frac{1}{2}\mathcal{L}_{\mathrm{Diss.}}dt}\mathrm{e}^{\mathcal{L}_{\mathrm{Coh.}}dt}\mathrm{e}^{\frac{1}{2}\mathcal{L}_{\mathrm{Diss.}}dt}[\hat{\rho}(t)], \tag{71}$$

where a short-time evolution by dt can be approximated to first-order by the symmetric, factorized product of individual exponentiated Liouville operators. This leads to a time-reversible and symplectic propagation for the simulated cavity loss, at a similar level to a velocity-Verlet-like scheme. The time-evolution can then be obtained as a step-wise propagation using the following equations of motion,

$$\dot{\rho}(t) = \frac{\Gamma}{2}\Big(\hat{L}\hat{\rho}(t)\hat{L}^{\dagger} - \frac{1}{2}\{\hat{L}^{\dagger}\hat{L},\hat{\rho}(t)\}\Big), \quad \dot{\rho}(t) = -\frac{i}{\hbar}[\hat{H},\hat{\rho}(t)], \quad \dot{\rho}(t) = \frac{\Gamma}{2}\Big(\hat{L}\hat{\rho}(t)\hat{L}^{\dagger} - \frac{1}{2}\{\hat{L}^{\dagger}\hat{L},\hat{\rho}(t)\}\Big). \tag{72}$$

We can expand the equations of motion in the adiabatic-Fock basis (Sec. 3.1.1). We define the matrix elements of the polaritonic Hamiltonian including the first-order non-adiabatic couplings as $H_{\alpha n,\beta m} = (H_{\mathrm{pl}})_{\alpha n,\beta m} - i\hbar\mathbf{d}_{\alpha\beta}\cdot\dot{\mathbf{R}}\delta_{nm}$, where we have used the fact that the Fock states have no dependence on the nuclear coordinates $\mathbf{d}_{\alpha n,\beta m} = \mathbf{d}_{\alpha\beta}\delta_{nm}$ and that $\dot{\mathbf{R}}$ is the classical velocity of the nuclei. Further, the matrix elements of the Lindblad jump operator can be written as $L_{\alpha n,\beta m} = \sqrt{m}\delta_{n,m-1}\delta_{\alpha\beta}$, which has no affect on the electronic states. Fig. 7 presents results of the computational method by combining (Fig. 7a-d) Ehrenfest and (Fig. 7e,f) surface hopping dynamics with a stochastic extension to the previously outlined Lindblad decay. For details pertaining to the stochastic analogue to the aforementioned Lindblad loss approach, see Ref. 176. This approach stochastically maps the dynamics in Liouville space to dynamics in the Hilbert space. We refer to this method as the $\mathcal{L}$-MFE approach. The convergence of this approach[176] with respect to the number of trajectories is similar to any mixed quantum-classical method, thus the addition of the stochastic cavity loss does not increase the computational cost. This is a general scheme that can be easily incorporated into any trajectory-based dynamics approaches, such as Ehrenfest, FSSH, or mapping approaches, or additionally to any trajectory-guided wavepacket-based methods, such as *ab initio* multiple spawning or *ab initio* multiple cloning.

The model system[13] portrays an isomerization reaction containing two electronic states $|\mathrm{g}\rangle$ and $|\mathrm{e}\rangle$ and two photonic Fock states $|0\rangle$ and $|1\rangle$ with a spin-boson bath for the nuclear DOFs to mediate electronic transitions. Due to the use of the Jaynes-Cummings Hamiltonian in the single-excited subspace, the ground state is "uncoupled" from the excited states via direct light-matter interaction; however, due to the cavity loss, the Lindblad decay mediates population transfer from $|\mathrm{g},1\rangle \rightarrow |\mathrm{g},0\rangle$ with a rate of Γ.

Fig. 7a,b show the potential energy surfaces of the three states with light-matter coupling A_0 set to 0.0 eV (Fig. 7a) and 0.136 eV (Fig. 7b) with a cavity frequency of ω_{c} = 1.632 eV. Fig. 7c,d present the polariton population dynamics in the adiabatic-Fock basis with loss rates of Γ = 0 meV (Fig. 7c) and Γ = 1 meV (Fig. 7d). The numerically exact results are obtained using the discrete variable representation (DVR) basis[114] for the nuclear DOF and Fock states for the photonic basis. As shown in Fig. 7c, the $\mathcal{L}$-MFE dynamics (dotted line) capture the essential physics of the problem but deviate from the exact simulations (solid) at a longer time, which is a known problem of the mean-field Ehrenfest approach and is not the main point of this discussion. The dynamics portrayed with a loss rate of Γ = 0.0 meV (Fig. 7c) reduce exactly to the dynamics of a closed quantum system with zero population residing in the uncoupled ground state, at any time t. At increased cavity loss of Γ = 1 meV (Fig. 7d), the system slowly populates the ground polaritonic states by funneling population from $|\mathrm{g},1\rangle$ to $|\mathrm{g},0\rangle$. This gives rise to plateaus in the ground state population curve when the majority of the population is present in the $|\mathrm{e},1\rangle$ state during the coherent population transfer processes, most pronounced at short times $t < 1.0$ ps.

Fig. 7e,f provides a direct application of this method to an *ab initio* on-the-fly dynamics study of the isomerization of azomethane (a direct extension to the results shown in Fig. 6).[175] The polaritonic potential energy surfaces can

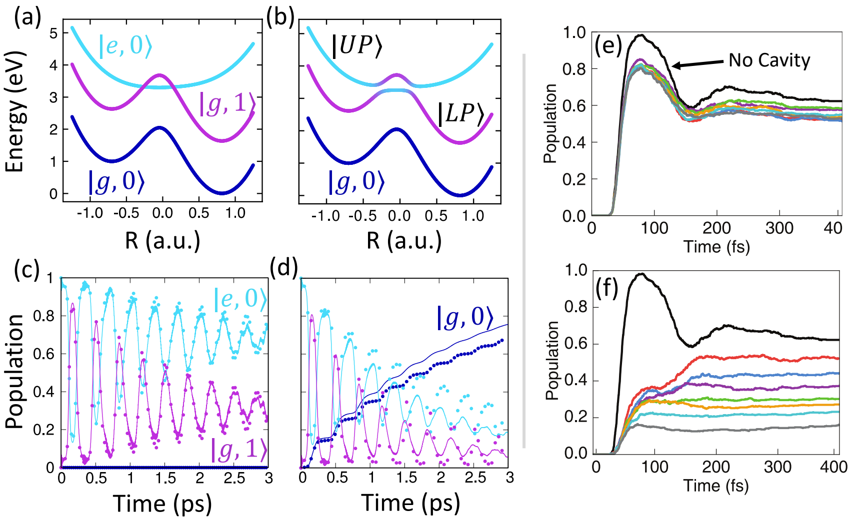

FIGURE 7 Potential energy surfaces (PESs) and population dynamics of the model isomerization reaction coupled to the cavity. Panel (a) presents the diabatic PESs where the dark blue line is the $|g,0\rangle$ PES, the cyan line is the $|e,0\rangle$ PES, and the magenta line is the $|g,1\rangle$ PES. Panel (b) presents the adiabatic PESs where the dark blue line is the uncoupled ground state $|g,0\rangle$ PES, the middle line (labeled $|\text{LP}\rangle$) is the lower polariton PES, and the upper line (labeled $|\text{UP}\rangle$) is the upper polariton PES. The colors along the adiabatic PESs represent the diabatic character at each nuclear position. Panels (c)–(d) present the polaritonic population dynamics with a decay rate of (c) $\Gamma = 0$ and (d) $\Gamma = 1$ meV. The solid lines are exact Lindblad dynamics, while the dotted lines are the approximate L-MFE method. The colors of the curves represent the population of various adiabatic-Fock basis states: $|g,0\rangle$ (dark blue), $|e,0\rangle$ (cyan), and $|g,1\rangle$ (magenta). For the same on-the-fly *ab initio* isomerization as shown in Fig. 6, panels (e)-(f) show the trans isomer population dynamics for various cavity loss rates $\Gamma = 0$, 2, 4, 8, 16, 32, and 64 meV (colors, top to bottom) at light-matter coupling strengths of A_0 = (e) 0.05 a.u. and (f) 0.5 a.u. The results outside the cavity is shown as a solid black curve.

be found in Fig. 6b. The loss rate Γ was varied (colors) from $\Gamma = 0.0$ to 64 meV for a light-matter coupling strengths A_0 = (Fig. 7e) 0.05 a.u. and (Fig. 7f) 0.5 a.u. At low coupling strength, the effects of the cavity loss are minimal. The dynamics at increased coupling strength allow for additional population to transfer to $|\text{g},1\rangle$ leading to fast decay into the cis-ground state $|\text{g},0\rangle$ without allowing enough time for the nuclear rearrangement to the trans-isomer before relaxing. This almost completely removes the isomerization pathway previously available to the system, effectively turning off the isomerization process for increased cavity loss rate.

In the present cases, the effects of cavity loss provide an additional factor when considering cavity-modified reaction rates – in the present *ab initio* case, the cavity loss coincide with the effects of the light-matter coupling strength which decreases the reaction yield. Overall, explicitly including cavity loss in realistic polaritonic dynamics is required for a rigorous and consistent comparison to experiment, where the cavity loss rates are substantial enough to cause dramatic effects on the population dynamics and subsequent photo-reaction pathways accessible to the system.

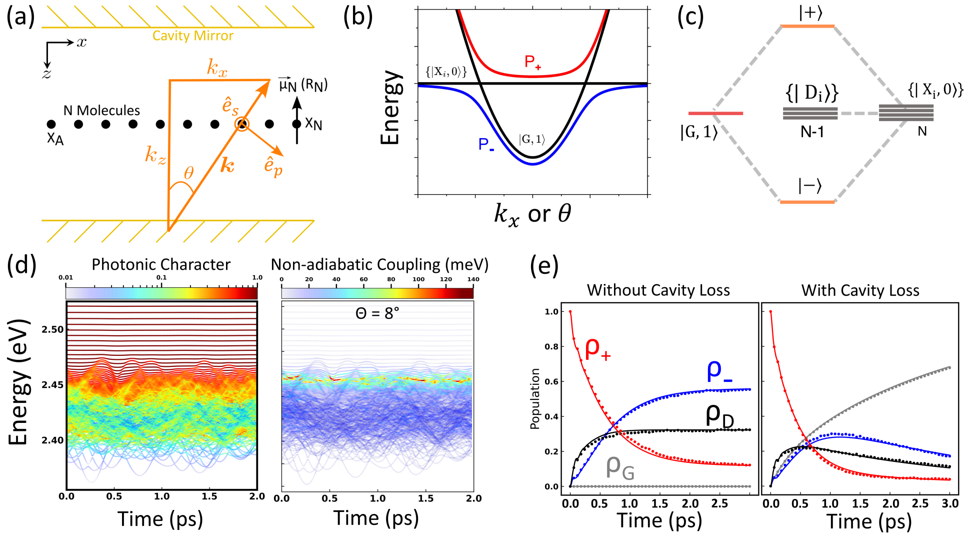

FIGURE 8 (a) Schematics of N molecules coupled to a FP cavity. (b) Polariton Eigenspectrum predicted by the Tavis-Cummings (TC) model. (c) Polariton Eigenspectrum predicted by the Jaynes-Cummings (JC) model. (d) Time-dependent polaritonic energies colored by (left) photonic character and (right) non-adiabatic coupling from a representative trajectory. (e) Time-dependent polaritonic populations of the ground-state (gray), upper polariton states (red), lower polariton state (blue), as well as the total population of the dark-states (black). Panels (d) and (e) were taken from https://pubs.acs.org/doi/10.1021/acsnano.4c05871

5.3 | Extending to many-molecule and many-mode simulations

In reality, optical cavities are composed of many photonic modes/wavevectors (*i.e.*, cavity dispersion relations) whose form depends on the type of cavity. For example, in typical Fabry-Perot (parallel mirror cavities, Fig. 8a), the dispersion relation can be written as $E_{\text{ph}}(\theta) = \frac{\hbar}{n_\text{c}} c\sqrt{k_z^2 + k_x^2} = \frac{\hbar}{n_\text{c}} ck_z\sqrt{1 + \tan^2\theta}$, which depends on the angle of the external probe, $\theta = \tan^{-1}(k_x/k_z)$. Here c is the speed of light in vacuum, n_c is the refractive index inside the cavity, and $\hbar\mathbf{k}$ is the momentum of the photon. It should be noted that there are many other cavity designs, most notably the plasmonic cavity which contain many varied geometrical arrangements of nanoparticles-on-metal-surfaces which lead to a wide variety of cavity dispersion relations.[177] As shown in Fig. 8a, the total wavevector $\mathbf{k} = \langle k_x, k_z\rangle$ is related to the quasi-continuous parallel k_x and strictly quantized perpendicular k_z modes. Additionally, there may be many molecules N_mol collectively coupled to these cavity modes N_mode, The scaling of such a Hilbert space (given by the Hamiltonian in Eq. 17) can be written as $\dim[\hat{H}] \propto N_\text{el}^{N_\text{mol}} \times N_\text{F}^{N_\text{mode}}$, which is exponential in both the number of molecules as well as the number of photon modes. While not the focus of this review, for extended systems (*i.e.*, solids), the incorporation of k-points raises further issues regarding the conservation of momentum between the electron and photon systems. This has been discussed in a few recent works.[178;179] In any case, making the long wavelength approximation nullifies any mismatch between the electron and photon momenta.

To overcome this unfeasible scaling, many works have shown that excited polaritonic states at weak-to-moderate light-matter coupling strengths can be simulated in the so-called first-excited subspace of the total Hamiltonian (Eq. 17). In singly excited subspace, the overall scaling can be written as $\dim[\hat{H}] \propto N_\text{el} N_\text{mol} N_\text{F} N_\text{mode}$, which is now

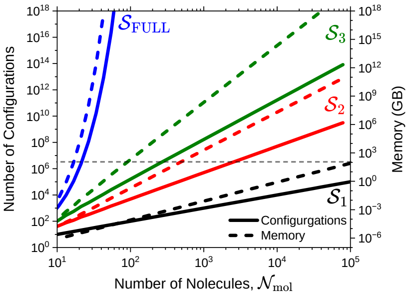

FIGURE 9 Numerical scaling of the Pauli-Fierz Hamiltonian in various subspaces: $\mathcal{S}_1$ (black), $\mathcal{S}_2$ (red), $\mathcal{S}_3$ (green) as well as the full Hilbert space $\mathcal{S}_{\text{FULL}}$ (blue) as a function of the number of molecules. The number of configurations/basis states are shown as solid curves and the required memory to store the Hamiltonian is shown as dashed curves. The thin, dashed gray line represents 100 GB of memory. Here, we assume only two electronic states per molecule, a single photonic mode with two Fock states, and a real-valued Hamiltonian (*i.e.*, complex would simply double the memory requirements).

linear scaling in all quantities. The zeroth $\mathcal{S}_0$ and singly excited $\mathcal{S}_1$ subspaces can be explicitly written as,

$$|\mathcal{S}_0\rangle = \bigotimes_{A}^{\mathcal{N}_{\text{mol}}} |\text{g}\rangle^{(A)} \otimes \bigotimes_{M}^{\mathcal{N}_{\text{mode}}} |0\rangle^{(M)}, \tag{73}$$

$$|\mathcal{S}_1\rangle = \sum_{A}^{\mathcal{N}_{\text{mol}}} \left(\bigotimes_{B<A}^{\mathcal{N}_{\text{mol}}} |\text{g}\rangle^{(B)} \otimes |\text{e}\rangle^{(A)} \otimes \bigotimes_{B>A}^{\mathcal{N}_{\text{mol}}} |\text{g}\rangle^{(B)} \right) \otimes |0\rangle + \bigotimes_{A}^{\mathcal{N}_{\text{mol}}} |0\rangle^{(A)} \otimes \sum_{M}^{\mathcal{N}_{\text{mode}}} \left(\bigotimes_{M<N}^{N-1} |0\rangle^{(M)} \otimes |1\rangle^{(N)} \otimes \bigotimes_{M>N}^{\mathcal{N}_{\text{mode}}} |0\rangle^{(M)} \right) \tag{74}$$

where we assumed only a single molecular ground and excited state per molecule $\{|\text{g}\rangle, |\text{e}\rangle\}$ and a single excited photon $\{|0\rangle, |1\rangle\}$ per mode, which is already a major approximation for most molecules with many nearby excited states. Higher-order subspaces have also been explored,[180] but even including the second excited subspace produces highly unfavorable scaling with a realistic number of molecules $\mathcal{N}_{\text{mol}} \sim 10^6$. Fig. 9 presents the numerical scaling (*i.e.* the number of possible configurations/basis states) as solid curves as well as the required memory to store the Hamiltonian (dashed curves) as a function of the number of molecules. Here, we assume only two electronic states per molecule, a single photonic mode with two Fock states, and a real-valued Hamiltonian (*i.e.*, complex would simply double the memory requirements). The thick gray line represents 100 GB of memory, a typical node on a typical high-performance computing cluster. In the $\mathcal{S}_1$ subspace (black), the 100-GB line is reached with a little over 10^5 molecules, while for the second excited subspace $\mathcal{S}_2$ (red), this line is reached with a little less than 1000 molecules. Third subspace $\mathcal{S}_3$ (green) only allows for 100 molecules. The full Hilbert space scales exponentially (blue). This exemplifies the need for the truncation of the total Hilbert space in order to perform meaningful theoretical explorations with realistic cavity designs and environments.

Upon the diagonalization of the many-molecule, many-mode Hamiltonian (Eq. 17) in the singly excited subspace $\mathcal{S}_1$, polariton eigenenergies and eigenstates are obtained, as shown in Fig. 8b for a collection of quasi-continuous parallel cavity modes and Fig. 8c for a single resonant mode. Here, the formation of the upper and lower polariton branches $\text{P}_{+/-}$ (Fig. 8b) or states $|+/-\rangle$ (Fig. 8c) can be observed. Furthermore, due to the presence of the other molecules (which are all degenerate with the cavity frequency), many degenerate polaritonic states can be found at the same energy as the bare molecular transition. These states are referred to as "dark states" $\{\mathrm{D}_i\}$ since they contain no transition dipole moment between the polaritonic ground state nor do they contain any photonic character (in the absence of molecular disorder). The Rabi splitting in this case famously scales as $\Omega_\mathrm{R} \propto \sqrt{\mathcal{N}_\mathrm{mol}}$.[25;36] In the presence of molecular fluctuations (*e.g.*, thermal fluctuations), the photonic character becomes distributed amongst the "dark states".

Fig. 8d shows the time-dependence of the polariton eigenenergies colored by the (left) photonic character $\langle \psi_j | \hat{a}^\dagger \hat{a} | \psi_j \rangle$ and (right) non-adiabatic coupling $\sigma_j = \sum_k \langle \psi_j | \frac{d}{dt} | \psi_k \rangle$ for each polaritonic state j (both on log colorbar scales). The exchange of character mediates population dynamics between such polariton states (*i.e.*, cavity-mediated non-adiabtic couplings). Fig. 8e presents mixed quantum-classical mapping approach to surface hopping (MASH)[148;147] dynamics where a LASER drives population from the collective ground state $|\mathrm{G}\rangle$ to the upper polariton $|+\rangle$ (left) without and (right) with cavity loss. The dynamics suggest that the dark states quickly accumulate much of the population at initial times. Wihout cavity loss, the polaritonic states reach equilibrium by 3.0 ps, while with cavity loss, none of the state retain significant population due to the rapid transfer to the ground state and the ongoing polariton-polariton non-adiabatic couplings.

As discussed above in Fig. 9, the explicit inclusion of many-molecules yields unfavorable conditions for the direct diagonalization (Sec. 3.1) of the Hamiltonian. In the case of self-consistent approaches (Sec. 3.2), one encounters a similar bottleneck where the inclusion of many sets of one-molecule single-particle orbitals $N_\mathrm{sp} = N_\mathrm{occ} \times N_\mathrm{vir}$ leads to a many-molecule ground state density matrix of $\dim[\hat{\rho}] \propto N_\mathrm{sp} \times \mathcal{N}_\mathrm{mol}$. The off-diagonal blocks of which will include the long-range Coulomb, short-range exchange, and intermolecular DSE interactions. In recent work,[181] it was argued that the off-diagonal blocks of the total density matrix can be decoupled in the cavity Born-Oppenheimer (BO) approximation[58] in which the cavity photon is treated as a parameter (similar to the nuclear BO approximation). Thus, the diagonal blocks of the density matrix and treated as effectively independent, reducing the memory cost of the self-consistent treatment back to $\dim[\hat{\rho}] \propto N_\mathrm{sp}$ but with $\mathcal{N}_\mathrm{mol}$ such matrices. However, without approximations, such as cavity BO, treating many molecules coupled to many cavity modes is still beyond the reach of direct simulation. Relying on efficient semi-empirical or tight-binding approaches[182;183;184;185] may provide the most direct route toward the direct simulation of many molecule QED, including both ground and excited states and has already been used to simulate plasmonic systems.[186;187;188;189]

5.4 | Intermolecular Interactions

In experiment, often the molecules are spatially confined in a polymer matrix (*e.g.*, Poly(methyl methacrylate), PMMA). In such cases, the the molecules are often close enough to exhibit strong dipolar interactions amongst one another. Alternatively, molecular aggregates can be formed directly.[190] In these cases, from the perspective of polaritonic structure theory, the inclusion of molecular interactions must be considered carefully. The most rigorous approach is to consider all molecules simultaneously in a self-consistent sense (Sec. 3.2), which will naturally capture all molecule-molecule interactions, including those at or beyond dipole such as the entire Coulomb and exchange interactions. Additionally, the cavity itself provides intermolecular interactions through the DSE term in the Hamiltonian and thus provides a competition between bare molecular interactions and cavity-mediated molecular interactions. These cavity-induced effects to non-bonded interactions (*i.e.*, van der Waals, hydrogen bonding, etc.) was directly explored with the high-level scQED-CCSD approach for two molecules.[64] Though, for the extension to the many-molecules, including all molecules in the self-consistency is difficult and scales poorly with the number of increasing molecules. Hence, one should turn toward an approximate model which captures the leading-order physics, in the same sense as the parameterized QED approach aims to do (see Sec. 3.1).

Intermolecular interactions have been well-studied for molecules in the absence of a cavity,[191] including effects beyond the bare Coulomb interactions.[192] Here, we will focus only on the direct Coulomb interactions at the dipole level for brevity. Such interactions can be written as $\hat{H}_{\mathrm{Agg}} = \hat{H}_{\mathrm{el}} + \hat{J}$, where

$$\hat{J} = \frac{\hat{\boldsymbol{\mu}}_A \cdot \hat{\boldsymbol{\mu}}_B - 3(\hat{\boldsymbol{\mu}}_A \cdot \hat{\mathbf{e}}_A)(\hat{\boldsymbol{\mu}}_B \cdot \hat{\mathbf{e}}_B)}{|\mathbf{R}_A - \mathbf{R}_B|^3}$$

where $\hat{H}_{\mathrm{el}}$ is the bare electronic Hamiltonian (diagonal in the adiabatic representation) and $\hat{J}$ is the dipole-dipole interaction term.[50] $\mathbf{R}_A$ is the location of molecule A, and $\hat{\mathbf{e}}_A$ is the unit vector of molecule A (not to be confused with the unit vector of the cavity polarization $\mathbf{e}$). Adding the interaction term $\hat{J}$ to the many-molecule Hamiltonian in Eq. 17 will lead to additional physics and direct competition between the intermolecular DSE terms and the direct Coulomb interactions. These two interactions were shown to cancel each other when there is no electron density overlaps (*i.e.* in the absence of exchange couplings)[98;193]. However, this textbook result[193] has, to our knowledge, never been explicitly investigated in molecular cavity QED. Thus, in this modified light-matter Hamiltonian, the molecules now communicate between one another through both the light-matter and Coulomb interactions, and each molecule's electronic structure can be evaluated individually with massively parallelized electronic structure calculations.[32;168;194].

6 | CONCLUSIONS

As the experimental demonstrations of molecular cavity QED in the strong and ultrastrong coupling regimes become more frequent and accessible to the broader community, there is a need for the development of new theoretical tools that can accurately and efficiently describe such complex light-matter interactions found in experiments. This review summarizes some of these exciting theoretical advances in polariton chemistry, showcasing methods ranging from improvements in the fundamental framework and description of these hybrid systems to the computational challenges, techniques, and applications spanning from modifying reactivity in the ground state to understanding spectral signatures of excited state photochemistry.

In Sec. 2, we discussed the rigorous theoretical background of molecular cavity QED. We first reviewed the basic theory of the molecular Hamiltonian (Sec. 2.1) and introduced the necessary formalism for molecular quantum electrodynamics (Sec. 2.2). Sec.3 focused on solving the polaritonic eigenvalue equation using various approaches from direct diagonalization in the adiabatic-Fock basis (Sec. 3.1.1) and polarized Fock basis (Sec. 3.1.2) as well as the self-consistent solution at the mean-field (Sec. 3.2.2) and correlated (Sec. 3.2.3) levels of theory. Using the tools put forth in the previous two sections, Sec. 4 explored the rich quantum dynamics of the strongly coupled light-matter systems, laying out common approaches toward simulating exact (Sec. 4.1) and realistic (Sec. 4.2.1-4.2.3) molecules in the extended Hilbert space of the coupled electron-photon system as well as motivating the need for an accurate description and efficient calculation of the nuclear gradients (Sec. 4.3) used in the exact Pauli-Fierz Hamiltonian. Finally, in Sec. 5, we provide three directions toward a more complete picture of the molecular polariton picture in experiment, including machine learning polariton gradients (Sec. 5.1), the simulation and effects of cavity loss (Sec. 5.2), and the extension to many molecule and many cavity modes (Sec. 5.3).

Overall, with the recent new capabilities demonstrated in experiments, there has been a recent push to rigorously simulate polariton systems in the strong coupling regime. This has led to a number of theoretical innovations that start to explain and predict these experimental results. However, there are still many mysteries to solve as the systems get increasingly more complex with more molecules and cavity modes. From the theoretical perspective, the single-molecule case has made significant progress due to the relative numerical simplicity of the simulations compared to highly expensive many-mode and many-molecule (with many electronic levels) simulations that have yet to be fully explored. From the experimental perspective, single-molecule spectroscopy in plasmonic cavities is extremely challenging and has not been widely achieved; however, the results stemming from such simple hybrid systems will afford a much greater leap forward in understanding.

The purpose of this review was to introduce and outline state-of-the-art techniques toward the simulation of realistic, *ab initio* molecular polaritons for readers in the emergent field of polariton chemistry. This review captures much of the recent work, but not all, toward the description of polaritonic states and properties as well as their quantum dynamics. Specifically, this work focused on the methods and approaches needed for one to explore these complicated problems in more depth and did not focus on connecting theory to experiment. While this connection is intrinsic to the answers one seeks from simulation, the discussion of experimental progress and its setbacks is well beyond the scope of this review. We hope this work allows readers of all kinds to dive into the simulation of molecular polaritons to explore the many unknown features of this novel tool to manipulate chemical reactions as well as physical phenomena and to help the community address the many open questions still unexplored by theory and simulation.

Acknowledgements

This work was supported by the Air Force Office of Scientific Research under AFOSR Award No. FA9550-23-1-0438.

Conflict of Interest

The authors declare no competing interests.

references

1. Nagarajan K, Thomas A, Ebbesen TW. Chemistry under Vibrational Strong Coupling. *J. Am. Chem. Soc.* 2021; 143(41): 16877–16889. http://dx.doi.org/10.1021/jacs.1c07420 doi: 10.1021/jacs.1c07420

2. Garcia-Vidal FJ, Ciuti C, Ebbesen TW. Manipulating matter by strong coupling to vacuum fields. *Science* 2021; 373(6551). http://dx.doi.org/10.1126/science.abd0336 doi: 10.1126/science.abd0336

3. Hutchison JA, Schwartz T, Genet C, Devaux E, Ebbesen TW. Modifying Chemical Landscapes by Coupling to Vacuum Fields. *Angew. Chem. Int. Ed.* 2012; 51(7): 1592–1596. http://dx.doi.org/10.1002/anie.201107033 doi: 10.1002/anie.201107033

4. Thomas A, Lethuillier-Karl L, Nagarajan K, et al. Tilting a ground-state reactivity landscape by vibrational strong coupling. *Science* 2019; 363(6427): 615–619. http://dx.doi.org/10.1126/science.aau7742 doi: 10.1126/science.aau7742

5. Kowalewski M, Bennett K, Mukamel S. Cavity Femtochemistry: Manipulating Nonadiabatic Dynamics at Avoided Crossings. *J. Phys. Chem. Lett.* 2016; 7(11): 2050–2054. http://dx.doi.org/10.1021/acs.jpclett.6b00864 doi: 10.1021/acs.jpclett.6b00864

6. Kowalewski M, Bennett K, Mukamel S. Non-adiabatic dynamics of molecules in optical cavities. *J. Chem. Phys.* 2016; 144(5): 054309. http://dx.doi.org/10.1063/1.4941053 doi: 10.1063/1.4941053

7. Galego J, Garcia-Vidal FJ, Feist J. Suppressing photochemical reactions with quantized light fields. *Nat. Commun.* 2016; 7(1). http://dx.doi.org/10.1038/ncomms13841 doi: 10.1038/ncomms13841

8. Herrera F, Spano FC. Cavity-Controlled Chemistry in Molecular Ensembles. *Phys. Rev. Lett.* 2016; 116(23): 238301. http://dx.doi.org/10.1103/physrevlett.116.238301 doi: 10.1103/physrevlett.116.238301

9. Ribeiro RF, Martínez-Martínez LA, Du M, Gonzalez-Angulo JC, Yuen-Zhou J. Polariton chemistry: controlling molecular dynamics with optical cavities. *Chem. Sci.* 2018; 9(30): 6325–6339. http://dx.doi.org/10.1039/c8sc01043a doi: 10.1039/c8sc01043a

10. Feist J, Galego J, Garcia-Vidal FJ. Polaritonic Chemistry with Organic Molecules. *ACS Photonics* 2018; 5(1): 205–216. http://dx.doi.org/10.1021/acsphotonics.7b00680 doi: 10.1021/acsphotonics.7b00680

11. Lacombe L, Hoffmann NM, Maitra NT. Exact Potential Energy Surface for Molecules in Cavities. *Phys. Rev. Lett.* 2019; 123: 083201. http://dx.doi.org/10.1103/PhysRevLett.123.083201 doi: 10.1103/PhysRevLett.123.083201

12. Mandal A, Krauss TD, Huo P. Polariton-Mediated Electron Transfer via Cavity Quantum Electrodynamics. *J. Phys. Chem. B* 2020; 124(29): 6321–6340. http://dx.doi.org/10.1021/acs.jpcb.0c03227 doi: 10.1021/acs.jpcb.0c03227

13. Mandal A, Huo P. Investigating New Reactivities Enabled by Polariton Photochemistry. *J. Phys. Chem. Lett.* 2019; 10(18): 5519–5529. http://dx.doi.org/10.1021/acs.jpclett.9b01599 doi: 10.1021/acs.jpclett.9b01599

14. Li X, Mandal A, Huo P. Theory of Mode-Selective Chemistry through Polaritonic Vibrational Strong Coupling. *J. Phys. Chem. Lett.* 2021; 12(29): 6974–6982. http://dx.doi.org/10.1021/acs.jpclett.1c01847 doi: 10.1021/acs.jpclett.1c01847

15. Brumer P, Shapiro M. Control of unimolecular reactions using coherent light. *Chem. Phys. Lett.* 1986; 126(6): 541–546. http://dx.doi.org/10.1016/s0009-2614(86)80171-3 doi: 10.1016/s0009-2614(86)80171-3

16. Shapiro M. *Quantum control of molecular processes*. Wiley-VCH . 2012.

17. Weight BM, Weix DJ, Tonzetich ZJ, Krauss TD, Huo P. Cavity Quantum Electrodynamics Enables para- and ortho-Selective Electrophilic Bromination of Nitrobenzene. *J. Am. Chem. Soc.* 2024; 146(23): 16184–16193. http://dx.doi.org/10.1021/jacs.4c04045 doi: 10.1021/jacs.4c04045

18. Pavošević F, Hammes-Schiffer S, Rubio A, Flick J. Cavity-Modulated Proton Transfer Reactions. *J. Am. Chem. Soc.* 2022; 144(11): 4995–5002. http://dx.doi.org/10.1021/jacs.1c13201 doi: 10.1021/jacs.1c13201

19. Pavošević F, Smith RL, Rubio A. Computational study on the catalytic control of endo/exo Diels-Alder reactions by cavity quantum vacuum fluctuations. *Nat Commun* 2023; 14(1): 2766. http://dx.doi.org/10.1038/s41467-023-38474-w doi: 10.1038/s41467-023-38474-w

20. Thomas A, George J, Shalabney A, et al. Ground-State Chemical Reactivity under Vibrational Coupling to the Vacuum Electromagnetic Field. *Angew. Chem. Int. Ed.* 2016; 55(38): 11462–11466. http://dx.doi.org/10.1002/anie.201605504 doi: 10.1002/anie.201605504

21. Lather J, Bhatt P, Thomas A, Ebbesen TW, George J. Cavity Catalysis by Cooperative Vibrational Strong Coupling of Reactant and Solvent Molecules. *Angew. Chem. Int. Ed.* 2019; 58(31): 10635–10638. http://dx.doi.org/10.1002/anie.201905407 doi: 10.1002/anie.201905407

22. Imperatore MV, Asbury JB, Giebink NC. Reproducibility of cavity-enhanced chemical reaction rates in the vibrational strong coupling regime. *J. Chem. Phys.* 2021; 154(19): 191103. http://dx.doi.org/10.1063/5.0046307 doi: 10.1063/5.0046307

23. Wiesehan GD, Xiong W. Negligible rate enhancement from reported cooperative vibrational strong coupling catalysis. *J. Chem. Phys.* 2021; 155(24): 241103. http://dx.doi.org/10.1063/5.0077549 doi: 10.1063/5.0077549

24. Kowalewski M, Mukamel S. Manipulating Molecules with Quantum Light. *Proc. Natl. Acad. Sci.* 2017; 114(13): 3278–3280. http://dx.doi.org/10.1073/pnas.1702160114 doi: 10.1073/pnas.1702160114

25. Chikkaraddy R, Nijs dB, Benz F, et al. Single-molecule strong coupling at room temperature in plasmonic nanocavities. *Nature* 2016; 535(7610): 127–130. http://dx.doi.org/10.1038/nature17974 doi: 10.1038/nature17974

26. Santhosh K, Bitton O, Chuntonov L, Haran G. Vacuum Rabi splitting in a plasmonic cavity at the single quantum emitter limit. *Nat. Commun.* 2016; 7(1): 1–5.

27. Fregoni J, Granucci G, Coccia E, Persico M, Corni S. Manipulating Azobenzene Photoisomerization through Strong Light-Molecule Coupling. *Nat. Commun.* 2018; 9(1): 4688. http://dx.doi.org/10.1038/s41467-018-06971-y doi: 10.1038/s41467-018-06971-y

28. Zhang Y, Nelson T, Tretiak S. Non-Adiabatic Molecular Dynamics of Molecules in the Presence of Strong Light-Matter Interactions. *J. Chem. Phys.* 2019; 151(15): 154109. http://dx.doi.org/10.1063/1.5116550 doi: 10.1063/1.5116550

29. Qiu L, Mandal A, Morshed O, et al. Molecular Polaritons Generated from Strong Coupling between CdSe Nanoplatelets and a Dielectric Optical Cavity. *J. Phys. Chem. Lett.* 2021; 12(20): 5030–5038. http://dx.doi.org/10.1021/acs.jpclett.1c01104 doi: 10.1021/acs.jpclett.1c01104

30. Polak D, Jayaprakash R, Lyons TP, et al. Manipulating molecules with strong coupling: harvesting triplet excitons in organic exciton microcavities. *Chem. Sci.* 2020; 11: 343–354.

31. Schwartz T, Hutchison JA, Genet C, Ebbesen TW. Reversible Switching of Ultrastrong Light-Molecule Coupling. *Phys. Rev. Lett.* 2011; 106(19): 196405. http://dx.doi.org/10.1103/physrevlett.106.196405 doi: 10.1103/physrevlett.106.196405

32. Groenhof G, Climent C, Feist J, Morozov D, Toppari JJ. Tracking Polariton Relaxation with Multiscale Molecular Dynamics Simulations. *J. Phys. Chem. Lett.* 2019; 10(18): 5476–5483. http://dx.doi.org/10.1021/acs.jpclett.9b02192 doi: 10.1021/acs.jpclett.9b02192

33. Golub GH. *Matrix Computations*. Johns Hopkins University Press . 1996.

34. Tretiak S, Mukamel S. Density Matrix Analysis and Simulation of Electronic Excitations in Conjugated and Aggregated Molecules. *Chem. Rev.* 2002; 102(9): 3171–3212. http://dx.doi.org/10.1021/cr0101252 doi: 10.1021/cr0101252

35. Tretiak S, Isborn CM, Niklasson AMN, Challacombe M. Representation independent algorithms for molecular response calculations in time-dependent self-consistent field theories. *J. Chem. Phys.* 2009; 130(5): 054111. http://dx.doi.org/10.1063/1.3068658 doi: 10.1063/1.3068658

36. Mandal A, Taylor MAD, Weight BM, Koessler ER, Li X, Huo P. Theoretical Advances in Polariton Chemistry and Molecular Cavity Quantum Electrodynamics. 2023; 123(16): 9786–9879. http://dx.doi.org/https://doi.org/10.1021/acs.chemrev.2c00855 doi: https://doi.org/10.1021/acs.chemrev.2c00855

37. Weight BM, Krauss TD, Huo P. Investigating Molecular Exciton Polaritons Using Ab Initio Cavity Quantum Electrodynamics. *J. Phys. Chem. Lett.* 2023; 14: 5901–5913. http://dx.doi.org/10.1021/acs.jpclett.3c01294 doi: 10.1021/acs.jpclett.3c01294

38. Yang J, Ou Q, Pei Z, et al. Quantum-electrodynamical time-dependent density functional theory within Gaussian atomic basis. *J. Chem. Phys.* 2021; 155(6): 064107. http://dx.doi.org/10.1063/5.0057542 doi: 10.1063/5.0057542

39. Flick J, Narang P. Ab initio polaritonic potential-energy surfaces for excited-state nanophotonics and polaritonic chemistry. *J. Chem. Phys.* 2020; 153(9): 094116. http://dx.doi.org/10.1063/5.0021033 doi: 10.1063/5.0021033

40. DePrince AE. Cavity-modulated ionization potentials and electron affinities from quantum electrodynamics coupled-cluster theory. *J. Chem. Phys.* 2022; 154(9): 094112. http://dx.doi.org/10.1063/5.0038748 doi: 10.1063/5.0038748

41. Haugland TS, Ronca E, Kjønstad EF, Rubio A, Koch H. Coupled Cluster Theory for Molecular Polaritons: Changing Ground and Excited States. *Phys. Rev. X* 2020; 10(4): 041043. http://dx.doi.org/10.1103/PhysRevX.10.041043 doi: 10.1103/PhysRevX.10.041043

42. Son M, Armstrong ZT, Allen RT, Dhavamani A, Arnold MS, Zanni MT. Energy cascades in donor-acceptor exciton-polaritons observed by ultrafast two-dimensional white-light spectroscopy. *Nat Commun* 2022; 13(1): 7305. http://dx.doi.org/10.1038/s41467-022-35046-2 doi: 10.1038/s41467-022-35046-2

43. Graf A, Held M, Zakharko Y, Tropf L, Gather MC, Zaumseil J. Electrical pumping and tuning of exciton-polaritons in carbon nanotube microcavities. *Nature Mater* 2017; 16(9): 911–917. http://dx.doi.org/10.1038/nmat4940 doi: 10.1038/nmat4940

44. Graf A, Tropf L, Zakharko Y, Zaumseil J, Gather MC. Near-infrared exciton-polaritons in strongly coupled single-walled carbon nanotube microcavities. *Nat Commun* 2016; 7(1): 13078. http://dx.doi.org/10.1038/ncomms13078 doi: 10.1038/ncomms13078

45. Möhl C, Graf A, Berger FJ, et al. Trion-Polariton Formation in Single-Walled Carbon Nanotube Microcavities. *ACS Photonics* 2018; 5(6): 2074–2080. http://dx.doi.org/10.1021/acsphotonics.7b01549 doi: 10.1021/acsphotonics.7b01549

46. Lüttgens JM, Berger FJ, Zaumseil J. Population of Exciton–Polaritons via Luminescent sp3 Defects in Single-Walled Carbon Nanotubes. *ACS Photonics* 2021; 8(1): 182–193. http://dx.doi.org/10.1021/acsphotonics.0c01129 doi: 10.1021/acsphotonics.0c01129

47. Allen RT, Dhavamani A, Son M, Kéna-Cohen S, Zanni MT, Arnold MS. Population of Subradiant States in Carbon Nanotube Microcavities in the Ultrastrong Light–Matter Coupling Regime. *J. Phys. Chem. C* 2022; 126(19): 8417–8424. http://dx.doi.org/10.1021/acs.jpcc.2c02076 doi: 10.1021/acs.jpcc.2c02076

48. Amori AR, Hou Z, Krauss TD. Excitons in Single-Walled Carbon Nanotubes and Their Dynamics. *Annual Review of Physical Chemistry* 2018; 69(1): 81–99. http://dx.doi.org/10.1146/annurev-physchem-050317-014241 doi: 10.1146/annurev-physchem-050317-014241

49. Weight BM, Zheng M, Tretiak S. Signatures of Chemical Dopants in Simulated Resonance Raman Spectroscopy of Carbon Nanotubes. *J. Phys. Chem. Lett.* 2023; 14(5): 1182–1191. http://dx.doi.org/10.1021/acs.jpclett.2c03591 doi: 10.1021/acs.jpclett.2c03591

50. Weight BM, Sifain AE, Gifford BJ, Kilin D, Kilina S, Tretiak S. Coupling between Emissive Defects on Carbon Nanotubes: Modeling Insights. *J. Phys. Chem. Lett.* 2021; 12(32): 7846–7853. http://dx.doi.org/10.1021/acs.jpclett.1c01631 doi: 10.1021/acs.jpclett.1c01631

51. Weight BM, Sifain AE, Gifford BJ, Htoon H, Tretiak S. On-the-Fly Nonadiabatic Dynamics Simulations of Single-Walled Carbon Nanotubes with Covalent Defects. *ACS Nano* 2023; 17(7): 6208–6219. http://dx.doi.org/10.1021/acsnano.2c08579 doi: 10.1021/acsnano.2c08579

52. Gifford BJ, Saha A, Weight BM, et al. Mod(n-m,3) Dependence of Defect-State Emission Bands in Aryl-Functionalized Carbon Nanotubes. *Nano Lett.* 2019; 19(12): 8503–8509. http://dx.doi.org/10.1021/acs.nanolett.9b02926 doi: 10.1021/acs.nanolett.9b02926

53. Gifford BJ, Kilina S, Htoon H, Doorn SK, Tretiak S. Controlling Defect-State Photophysics in Covalently Functionalized Single-Walled Carbon Nanotubes. *Acc. Chem. Res.* 2020; 53(9): 1791–1801. http://dx.doi.org/10.1021/acs.accounts.0c00210 doi: 10.1021/acs.accounts.0c00210

54. Gifford BJ, Kilina S, Htoon H, Doorn SK, Tretiak S. Exciton Localization and Optical Emission in Aryl-Functionalized Carbon Nanotubes. *J. Phys. Chem. C* 2018; 122(3): 1828–1838. http://dx.doi.org/10.1021/acs.jpcc.7b09558 doi: 10.1021/acs.jpcc.7b09558

55. Gifford BJ, He X, Kim M, et al. Optical Effects of Divalent Functionalization of Carbon Nanotubes. *Chem. Mater.* 2019; 31(17): 6950–6961. http://dx.doi.org/10.1021/acs.chemmater.9b01438 doi: 10.1021/acs.chemmater.9b01438

56. Hou Z, Krauss TD. Photoluminescence Brightening of Isolated Single-Walled Carbon Nanotubes. *J. Phys. Chem. Lett.* 2017; 8(19): 4954–4959. http://dx.doi.org/10.1021/acs.jpclett.7b01890 doi: 10.1021/acs.jpclett.7b01890

57. Hou Z, Tumiel TM, Krauss TD. Spatially resolved photoluminescence brightening in individual single-walled carbon nanotubes. *Journal of Applied Physics* 2021; 129(1): 014305. http://dx.doi.org/10.1063/5.0030951 doi: 10.1063/5.0030951

58. Flick J, Appel H, Ruggenthaler M, Rubio A. Cavity Born–Oppenheimer Approximation for Correlated Electron–Nuclear-Photon Systems. *J. Chem. Theory Comput.* 2017; 13(4): 1616–1625. http://dx.doi.org/10.1021/acs.jctc.6b01126 doi: 10.1021/acs.jctc.6b01126

59. Triana JF, Peláez D, Sanz-Vicario JL. Entangled Photonic-Nuclear Molecular Dynamics of LiF in Quantum Optical Cavities. *J. Phys. Chem. A* 2018; 122(8): 2266–2278. http://dx.doi.org/10.1021/acs.jpca.7b11833 doi: 10.1021/acs.jpca.7b11833

60. Triana JF, Hernández FJ, Herrera F. The shape of the electric dipole function determines the sub-picosecond dynamics of anharmonic vibrational polaritons. *J. Chem. Phys.* 2020; 152(23): 234111. http://dx.doi.org/10.1063/5.0009869 doi: 10.1063/5.0009869

61. Mandal A, Vega SM, Huo P. Polarized Fock States and the Dynamical Casimir Effect in Molecular Cavity Quantum Electrodynamics. *J. Phys. Chem. Lett.* 2020; 11(21): 9215–9223. http://dx.doi.org/10.1021/acs.jpclett.0c02399 doi: 10.1021/acs.jpclett.0c02399

62. Philbin TG. Generalized coherent states. *Amer. J. Phys.* 2014; 82(8): 742–748. http://dx.doi.org/10.1119/1.4876963 doi: 10.1119/1.4876963

63. McTague J, Foley JJ. Non-Hermitian cavity quantum electrodynamics–configuration interaction singles approach for polaritonic structure with ab initio molecular Hamiltonians. *J. Chem. Phys.* 2022; 156(15): 154103. http://dx.doi.org/10.1063/5.0091953 doi: 10.1063/5.0091953

64. Haugland TS, Schäfer C, Ronca E, Rubio A, Koch H. Intermolecular interactions in optical cavities: An ab initio QED study. *J. Chem. Phys.* 2021; 154(9): 094113. http://dx.doi.org/10.1063/5.0039256 doi: 10.1063/5.0039256

65. Ruggenthaler M, Tancogne-Dejean N, Flick J, Appel H, Rubio A. From a quantum-electrodynamical light–matter description to novel spectroscopies. *Nat. Rev. Chem.* 2018; 2(3): 1–16. http://dx.doi.org/10.1038/s41570-018-0118 doi: 10.1038/s41570-018-0118

66. Tichauer RH, Feist J, Groenhof G. Multi-scale dynamics simulations of molecular polaritons: The effect of multiple cavity modes on polariton relaxation. *J. Chem. Phys.* 2021; 154(10): 104112. http://dx.doi.org/10.1063/5.0037868 doi: 10.1063/5.0037868

67. Liebenthal MD, Vu N, DePrince AE. Equation-of-motion cavity quantum electrodynamics coupled-cluster theory for electron attachment. *J. Chem. Phys.* 2022; 156(5): 054105. http://dx.doi.org/10.1063/5.0078795 doi: 10.1063/5.0078795

68. Riso RR, Haugland TS, Ronca E, Koch H. Molecular orbital theory in cavity QED environments. *Nat. Commun.* 2022; 13(1): 1368. http://dx.doi.org/10.1038/s41467-022-29003-2 doi: 10.1038/s41467-022-29003-2

69. Weight BM, Li X, Zhang Y. Theory and modeling of light-matter interactions in chemistry: current and future. *Phys. Chem. Chem. Phys.* 2023. http://dx.doi.org/10.1039/D3CP01415K doi: 10.1039/D3CP01415K

70. Foley JJ, McTague JF, DePrince AE. Ab initio methods for polariton chemistry. *Chemical Physics Reviews* 2023; 4(4): 041301. http://dx.doi.org/10.1063/5.0167243 doi: 10.1063/5.0167243

71. Wang DS, Yelin SF, Flick J. Defect Polaritons from First Principles. *ACS Nano* 2021; 15(9): 15142–15152. http://dx.doi.org/10.1021/acsnano.1c05600 doi: 10.1021/acsnano.1c05600

72. Loudon M, Parise J. *Organic Chemistry*. Macmillan Learning . 2015. Google-Books-ID: 9YhPrgEACAAJ.

73. Anslyn EV, Dougherty DA. *Modern Physical Organic Chemistry*. University Science Books . 2006.

74. Akselrod GM, Huang J, Hoang TB, et al. Large-Area Metasurface Perfect Absorbers from Visible to Near-Infrared. *Advanced Materials* 2015; 27(48): 8028–8034. http://dx.doi.org/10.1002/adma.201503281 doi: 10.1002/adma.201503281

75. Vu N, McLeod GM, Hanson K, DePrince AE. Enhanced Diastereocontrol via Strong Light–Matter Interactions in an Optical Cavity. *J. Phys. Chem. A* 2022; 126(49): 9303–9312. http://dx.doi.org/10.1021/acs.jpca.2c07134 doi: 10.1021/acs.jpca.2c07134

76. Liebenthal MD, Vu N, Iii AED. Mean-Field Cavity Effects in Quantum Electrodynamics Density Functional and Coupled-Cluster Theories. http://dx.doi.org/10.48550/arXiv.2303.10821Xiv:2303.10821 doi: 10.48550/arXiv.2303.10821Xiv:2303.10821

77. Fregoni J, Corni S, Persico M, Granucci G. Photochemistry in the strong coupling regime: A trajectory surface hopping scheme. *J. Comput. Chem.* 2020; 41(23): 2033–2044. http://dx.doi.org/10.1002/jcc.26369 doi: 10.1002/jcc.26369

78. Mordovina U, Bungey C, Appel H, Knowles PJ, Rubio A, Manby FR. Polaritonic coupled-cluster theory. *Phys. Rev. Research* 2020; 2(2): 023262. http://dx.doi.org/10.1103/PhysRevResearch.2.023262 doi: 10.1103/PhysRevResearch.2.023262

79. Cui ZH, Mandal A, Reichman DR. Variational Lang–Firsov Approach Plus Møller–Plesset Perturbation Theory with Applications to Ab Initio Polariton Chemistry. *J. Chem. Theory Comput.* 2024; 20(3): 1143–1156. http://dx.doi.org/10.1021/acs.jctc.3c01166 doi: 10.1021/acs.jctc.3c01166

80. Matoušek M, Vu N, Govind N, Foley IV JJ, Veis L. Polaritonic Chemistry using the Density Matrix Renormalization Group Method. 2024. arXiv:2407.01381

81. Li X, Zhang Y. First-principles molecular quantum electrodynamics theory at all coupling strengths. 2023. arXiv:2310.18228 [physics]http://dx.doi.org/10.48550/arXiv.2310.18228 doi: 10.48550/arXiv.2310.18228

82. Liebenthal MD, Vu N, DePrince AEI. Assessing the Effects of Orbital Relaxation and the Coherent-State Transformation in Quantum Electrodynamics Density Functional and Coupled-Cluster Theories. *J. Phys. Chem. A* 2023; 127(24): 5264–5275. http://dx.doi.org/10.1021/acs.jpca.3c01842 doi: 10.1021/acs.jpca.3c01842

83. Yanai T, Tew DP, Handy NC. A new hybrid exchange–correlation functional using the Coulomb-attenuating method (CAM-B3LYP). *Chem. Phys. Let.* 2004; 393(1): 51–57. http://dx.doi.org/10.1016/j.cplett.2004.06.011 doi: 10.1016/j.cplett.2004.06.011

84. Chai JD, Head-Gordon M. Systematic optimization of long-range corrected hybrid density functionals. *J. Chem. Phys.* 2008; 128(8): 084106. http://dx.doi.org/10.1063/1.2834918 doi: 10.1063/1.2834918

85. Chai JD, Head-Gordon M. Long-range corrected hybrid density functionals with damped atom–atom dispersion corrections. *Phys. Chem. Chem. Phys.* 2008; 10(44): 6615. http://dx.doi.org/10.1039/b810189b doi: 10.1039/b810189b

86. Sun J, Ruzsinszky A, Perdew JP. Strongly Constrained and Appropriately Normed Semilocal Density Functional. *Phys. Rev. Lett.* 2015; 115(3): 036402. http://dx.doi.org/10.1103/PhysRevLett.115.036402 doi: 10.1103/PhysRevLett.115.036402

87. Sun J, Remsing RC, Zhang Y, et al. Accurate first-principles structures and energies of diversely bonded systems from an efficient density functional. *Nature Chem* 2016; 8(9): 831–836. http://dx.doi.org/10.1038/nchem.2535 doi: 10.1038/nchem.2535

88. Flick J, Schäfer C, Ruggenthaler M, Appel H, Rubio A. Ab Initio Optimized Effective Potentials for Real Molecules in Optical Cavities: Photon Contributions to the Molecular Ground State. *ACS Photonics* 2018; 5(3): 992–1005. http://dx.doi.org/10.1021/acsphotonics.7b01279 doi: 10.1021/acsphotonics.7b01279

89. Pellegrini C, Flick J, Tokatly IV, Appel H, Rubio A. Optimized Effective Potential for Quantum Electrodynamical Time-Dependent Density Functional Theory. *Phys. Rev. Lett.* 2015; 115(9): 093001. http://dx.doi.org/10.1103/PhysRevLett.115.093001 doi: 10.1103/PhysRevLett.115.093001

90. Schäfer C, Buchholz F, Penz M, Ruggenthaler M, Rubio A. Making ab initio QED functional(s): Nonperturbative and photon-free effective frameworks for strong light–matter coupling. *Proc. Natl. Acad. Sci.* 2021; 118(41): e2110464118. http://dx.doi.org/10.1073/pnas.2110464118 doi: 10.1073/pnas.2110464118

91. Flick J. Simple Exchange-Correlation Energy Functionals for Strongly Coupled Light-Matter Systems Based on the Fluctuation-Dissipation Theorem. *Phys. Rev. Lett.* 2022; 129(14): 143201. http://dx.doi.org/10.1103/PhysRevLett.129.143201 doi: 10.1103/PhysRevLett.129.143201

92. Lu IT, Ruggenthaler M, Tancogne-Dejean N, Latini S, Penz M, Rubio A. Electron-photon exchange-correlation approximation for quantum-electrodynamical density-functional theory. *Phys. Rev. A* 2024; 109(5): 052823. http://dx.doi.org/10.1103/PhysRevA.109.052823 doi: 10.1103/PhysRevA.109.052823

93. Riso RR, Haugland TS, Ronca E, Koch H. On the characteristic features of ionization in QED environments. *J. Chem. Phys.* 2022; 156(23): 234103. http://dx.doi.org/10.1063/5.0091119 doi: 10.1063/5.0091119

94. Flick J, Rivera N, Narang P. Strong light-matter coupling in quantum chemistry and quantum photonics. *Nanophotonics* 2018; 7(9): 1479–1501. http://dx.doi.org/10.1515/nanoph-2018-0067 doi: 10.1515/nanoph-2018-0067

95. Flick J, Narang P. Cavity-Correlated Electron-Nuclear Dynamics from First Principles. *Phys. Rev. Lett.* 2018; 121(11): 113002. http://dx.doi.org/10.1103/PhysRevLett.121.113002 doi: 10.1103/PhysRevLett.121.113002

96. Flick J, Ruggenthaler M, Appel H, Rubio A. Kohn–Sham approach to quantum electrodynamical density-functional theory: Exact time-dependent effective potentials in real space. *Proc. Natl. Acad. Sci.* 2015; 112(50): 15285–15290. http://dx.doi.org/10.1073/pnas.1518224112 doi: 10.1073/pnas.1518224112

97. Flick J, Welakuh DM, Ruggenthaler M, Appel H, Rubio A. Light–Matter Response in Nonrelativistic Quantum Electrodynamics. *ACS Photonics* 2019; 6(11): 2757–2778. http://dx.doi.org/10.1021/acsphotonics.9b00768 doi: 10.1021/acsphotonics.9b00768

98. Flick J, Ruggenthaler M, Appel H, Rubio A. Atoms and molecules in cavities, from weak to strong coupling in quantum-electrodynamics (QED) chemistry. *Proc. Natl. Acad. Sci.* 2017; 114(12): 3026–3034. http://dx.doi.org/10.1073/pnas.1615509114 doi: 10.1073/pnas.1615509114

99. Wang DS, Neuman T, Flick J, Narang P. Light–matter interaction of a molecule in a dissipative cavity from first principles. *J. Chem. Phys.* 2021; 154(10): 104109. http://dx.doi.org/10.1063/5.0036283 doi: 10.1063/5.0036283

100. Buchholz F, Theophilou I, Giesbertz KJH, Ruggenthaler M, Rubio A. Light–Matter Hybrid-Orbital-Based First-Principles Methods: The Influence of Polariton Statistics. *J. Chem. Theory Comput.* 2020; 16(9): 5601–5620. http://dx.doi.org/10.1021/acs.jctc.0c00469 doi: 10.1021/acs.jctc.0c00469

101. Welakuh DM, Flick J, Ruggenthaler M, Appel H, Rubio A. Frequency-Dependent Sternheimer Linear-Response Formalism for Strongly Coupled Light–Matter Systems. *J. Chem. Theory Comput.* 2022; 18(7): 4354–4365. http://dx.doi.org/10.1021/acs.jctc.2c00076 doi: 10.1021/acs.jctc.2c00076

102. Sidler D, Ruggenthaler M, Schäfer C, Ronca E, Rubio A. A perspective on ab initio modeling of polaritonic chemistry: The role of non-equilibrium effects and quantum collectivity. *J. Chem. Phys.* 2022; 156(23): 230901. http://dx.doi.org/10.1063/5.0094956 doi: 10.1063/5.0094956

103. Sidler D, Schäfer C, Ruggenthaler M, Rubio A. Polaritonic Chemistry: Collective Strong Coupling Implies Strong Local Modification of Chemical Properties. *J. Phys. Chem. Lett.* 2021; 12(1): 508–516. http://dx.doi.org/10.1021/acs.jpclett.0c03436 doi: 10.1021/acs.jpclett.0c03436

104. Lu IT, Shin D, Hübener H, et al. Cavity engineered phonon-mediated superconductivity in MgB$_2$ from first principles quantum electrodynamics. 2024

105. White AF, Gao Y, Minnich AJ, Chan GKL. A coupled cluster framework for electrons and phonons. *The Journal of Chemical Physics* 2020; 153(22): 224112. http://dx.doi.org/10.1063/5.0033132 doi: 10.1063/5.0033132

106. Mallory JD, DePrince AE. Reduced-density-matrix-based ab initio cavity quantum electrodynamics. *Phys. Rev. A* 2022; 106(5): 053710. http://dx.doi.org/10.1103/PhysRevA.106.053710 doi: 10.1103/PhysRevA.106.053710

107. Weight BM, Tretiak S, Zhang Y. Diffusion quantum Monte Carlo approach to the polaritonic ground state. *Phys. Rev. A* 2024; 109(3): 032804. http://dx.doi.org/10.1103/PhysRevA.109.032804 doi: 10.1103/PhysRevA.109.032804

108. Xue J, Seo K, Tian L, Xiang T. Quantum phase transition in a multiconnected Jaynes-Cummings lattice. *Phys. Rev. B* 2017; 96(17): 174502. http://dx.doi.org/10.1103/PhysRevB.96.174502 doi: 10.1103/PhysRevB.96.174502

109. Rossini D, Fazio R, Santoro G. Photon and polariton fluctuations in arrays of QED-cavities. *EPL* 2008; 83(4): 47011. http://dx.doi.org/10.1209/0295-5075/83/47011 doi: 10.1209/0295-5075/83/47011

110. Pino dJ, Schröder FAYN, Chin AW, Feist J, Garcia-Vidal FJ. Tensor network simulation of polaron-polaritons in organic microcavities. *Phys. Rev. B* 2018; 98(16): 165416. http://dx.doi.org/10.1103/PhysRevB.98.165416 doi: 10.1103/PhysRevB.98.165416

111. Helgaker T, Jorgensen P, Olsen J. *Molecular Electronic-Structure Theory*. John Wiley & Sons . 2014.

112. Pavošević F, Flick J. Polaritonic Unitary Coupled Cluster for Quantum Computations. *J. Phys. Chem. Lett.* 2021; 12(37): 9100–9107. http://dx.doi.org/10.1021/acs.jpclett.1c02659 doi: 10.1021/acs.jpclett.1c02659

113. Born M, Huang K. Dynamical Theory of Crystal Lattices. *Am. J. Phys.* 1955; 23(7): 474–474. http://dx.doi.org/10.1119/1.1934059 doi: 10.1119/1.1934059

114. Colbert DT, Miller WH. A novel discrete variable representation for quantum mechanical reactive scattering via the S-matrix Kohn method. *J. Chem. Phys.* 1992; 96(3): 1982–1991. http://dx.doi.org/10.1063/1.462100 doi: 10.1063/1.462100

115. Tannor DJ. *Introduction to Quantum Mechanics: A Time-Dependent Perspective*. University Science books: Mill Valley, U.S.A . 2007.

116. Zhou W, Hu D, Mandal A, Huo P. Nuclear gradient expressions for molecular cavity quantum electrodynamics simulations using mixed quantum-classical methods. *J. Chem. Phys.* 2022; 157(10): 104118. http://dx.doi.org/10.1063/5.0109395 doi: 10.1063/5.0109395

117. Hofmann A, Vivie-Riedle dR. Adiabatic approach for ultrafast quantum dynamics mediated by simultaneously active conical intersections. *Chem. Phys. Lett.* 2001; 346(3): 299–304. http://dx.doi.org/10.1016/S0009-2614(01)00922-8 doi: 10.1016/S0009-2614(01)00922-8

118. Vendrell O. Coherent dynamics in cavity femtochemistry: Application of the multi-configuration time-dependent Hartree method. *Chem. Phys.* 2018; 509: 55–65. http://dx.doi.org/10.1016/j.chemphys.2018.02.008 doi: 10.1016/j.chemphys.2018.02.008

119. Csehi A, Vendrell O, Halász GJ, Vibók Á. Competition between Collective and Individual Conical Intersection Dynamics in an Optical Cavity. *New J. Phys.* 2022; 24(7): 073022. http://dx.doi.org/10.1088/1367-2630/ac7df7 doi: 10.1088/1367-2630/ac7df7

120. Triana JF, Herrera F. Ultrafast modulation of vibrational polaritons for controlling the quantum field statistics at mid-infrared frequencies. *New J. Phys.* 2022; 24(2): 023008.

121. Fischer EW, Anders J, Saalfrank P. Cavity-altered thermal isomerization rates and dynamical resonant localization in vibro-polaritonic chemistry. *J. Chem. Phys.* 2022; 156(15): 154305. http://dx.doi.org/10.1063/5.0076434 doi: 10.1063/5.0076434

122. Hoffmann NM, Appel H, Rubio A, Maitra NT. Light-matter interactions via the exact factorization approach. *Eur. Phys. J. B* 2018; 91(8): 180. http://dx.doi.org/10.1140/epjb/e2018-90177-6 doi: 10.1140/epjb/e2018-90177-6

123. Gu B, Mukamel S. Manipulating Nonadiabatic Conical Intersection Dynamics by Optical Cavities. *Chem. Sci.* 2020; 11(5): 1290–1298. http://dx.doi.org/10.1039/C9SC04992D doi: 10.1039/C9SC04992D

124. Lindoy LP, Mandal A, Reichman DR. Quantum dynamical effects of vibrational strong coupling in chemical reactivity. *Nat Commun* 2023; 14(1): 2733. http://dx.doi.org/10.1038/s41467-023-38368-x doi: 10.1038/s41467-023-38368-x

125. Ben-Nun M, Quenneville J, Martínez TJ. Ab Initio Multiple Spawning: Photochemistry from First Principles Quantum Molecular Dynamics. *J. Phys. Chem. A* 2000; 104(22): 5161–5175. http://dx.doi.org/10.1021/jp994174i doi: 10.1021/jp994174i

126. Ibele LM, Curchod BFE. A molecular perspective on Tully models for nonadiabatic dynamics. *Phys. Chem. Chem. Phys.* 2020; 22(27): 15183–15196. http://dx.doi.org/10.1039/D0CP01353F doi: 10.1039/D0CP01353F

127. Nelson TR, White AJ, Bjorgaard JA, et al. Non-adiabatic Excited-State Molecular Dynamics: Theory and Applications for Modeling Photophysics in Extended Molecular Materials. *Chem. Rev.* 2020; 120(4): 2215–2287. http://dx.doi.org/10.1021/acs.chemrev.9b00447 doi: 10.1021/acs.chemrev.9b00447

128. Ibele LM, Lassmann Y, Martínez TJ, Curchod BFE. Comparing (stochastic-selection) ab initio multiple spawning with trajectory surface hopping for the photodynamics of cyclopropanone, fulvene, and dithiane. *J. Chem. Phys.* 2021; 154(10): 104110. http://dx.doi.org/10.1063/5.0045572 doi: 10.1063/5.0045572

129. Lassmann Y, Curchod BFE. AIMSWISS—Ab initio multiple spawning with informed stochastic selections. *J. Chem. Phys.* 2021; 154(21): 211106. http://dx.doi.org/10.1063/5.0052118 doi: 10.1063/5.0052118

130. Curchod BFE, Rauer C, Marquetand P, González L, Martínez TJ. Communication: GAIMS—Generalized Ab Initio Multiple Spawning for both internal conversion and intersystem crossing processes. *J. Chem. Phys.* 2016; 144(10): 101102. http://dx.doi.org/10.1063/1.4943571 doi: 10.1063/1.4943571

131. Agostini F, Min SK, Abedi A, Gross EKU. Quantum-Classical Nonadiabatic Dynamics: Coupled- vs Independent-Trajectory Methods. *J. Chem. Theory Comput.* 2016; 12(5): 2127–2143. http://dx.doi.org/10.1021/acs.jctc.5b01180 doi: 10.1021/acs.jctc.5b01180

132. Lee IS, Ha JK, Han D, Kim TI, Moon SW, Min SK. PyUNIxMD: A Python-based excited state molecular dynamics package. *J. Comput. Chem.* 2021; 42(24): 1755–1766. http://dx.doi.org/10.1002/jcc.26711 doi: 10.1002/jcc.26711

133. Min SK, Agostini F, Gross EKU. Coupled-Trajectory Quantum-Classical Approach to Electronic Decoherence in Nonadiabatic Processes. *Phys. Rev. Lett.* 2015; 115(7): 073001. http://dx.doi.org/10.1103/PhysRevLett.115.073001 doi: 10.1103/PhysRevLett.115.073001

134. Min SK, Agostini F, Tavernelli I, Gross EKU. Ab Initio Nonadiabatic Dynamics with Coupled Trajectories: A Rigorous Approach to Quantum (De)Coherence. *J. Phys. Chem. Lett.* 2017; 8(13): 3048–3055. http://dx.doi.org/10.1021/acs.jpclett.7b01249 doi: 10.1021/acs.jpclett.7b01249

135. Tully JC. Perspective: Nonadiabatic dynamics theory. *J. Chem. Phys.* 2012; 137(22): 22A301. http://dx.doi.org/10.1063/1.4757762 doi: 10.1063/1.4757762

136. Nijjar P, Jankowska J, Prezhdo OV. Ehrenfest and classical path dynamics with decoherence and detailed balance. *J. Chem. Phys.* 2019; 150(20): 204124. http://dx.doi.org/10.1063/1.5095810 doi: 10.1063/1.5095810

137. Runeson JE, Richardson JO. Spin-mapping approach for nonadiabatic molecular dynamics. *J. Chem. Phys.* 2019; 151(4): 044119. http://dx.doi.org/10.1063/1.5100506 doi: 10.1063/1.5100506

138. Runeson JE, Richardson JO. Generalized spin mapping for quantum-classical dynamics. *J. Chem. Phys.* 2020; 152(8): 084110. http://dx.doi.org/10.1063/1.5143412 doi: 10.1063/1.5143412

139. Runeson JE, Mannouch JR, Amati G, Fiechter MR, Richardson JO. Spin-Mapping Methods for Simulating Ultrafast Nonadiabatic Dynamics. *CHIMIA* 2022; 76(6): 582–582. http://dx.doi.org/10.2533/chimia.2022.582 doi: 10.2533/chimia.2022.582

140. Mannouch JR, Richardson JO. A partially linearized spin-mapping approach for nonadiabatic dynamics. II. Analysis and comparison with related approaches. *J. Chem. Phys.* 2020; 153(19): 194110. http://dx.doi.org/10.1063/5.0031173 doi: 10.1063/5.0031173

141. He X, Wu B, Gong Z, Liu J. Commutator Matrix in Phase Space Mapping Models for Nonadiabatic Quantum Dynamics. *J. Phys. Chem. A* 2021; 125(31): 6845–6863. http://dx.doi.org/10.1021/acs.jpca.1c04429 doi: 10.1021/acs.jpca.1c04429

142. He X, Gong Z, Wu B, Liu J. Negative Zero-Point-Energy Parameter in the Meyer–Miller Mapping Model for Nonadiabatic Dynamics. *J. Phys. Chem. Lett.* 2021; 12(10): 2496–2501. http://dx.doi.org/10.1021/acs.jpclett.1c00232 doi: 10.1021/acs.jpclett.1c00232

143. He X, Liu J. A new perspective for nonadiabatic dynamics with phase space mapping models. *J. Chem. Phys.* 2019; 151(2): 024105. http://dx.doi.org/10.1063/1.5108736 doi: 10.1063/1.5108736

144. Mannouch JR, Richardson JO. A partially linearized spin-mapping approach for nonadiabatic dynamics. I. Derivation of the theory. *J. Chem. Phys.* 2020; 153(19): 194109. http://dx.doi.org/10.1063/5.0031168 doi: 10.1063/5.0031168

145. Mannouch JR, Richardson JO. A partially linearized spin-mapping approach for simulating nonlinear optical spectra. *J. Chem. Phys.* 2022; 156(2): 024108. http://dx.doi.org/10.1063/5.0077744 doi: 10.1063/5.0077744

146. Weight B, Mandal A, Hu D, Huo P. Ab initio Spin-Mapping Non-adiabatic Dynamics Simulations of Photochemistry. 2024

147. Mannouch JR, Richardson JO. A mapping approach to surface hopping. *The Journal of Chemical Physics* 2023; 158(10): 104111. http://dx.doi.org/10.1063/5.0139734 doi: 10.1063/5.0139734

148. Runeson JE, Manolopoulos DE. A multi-state mapping approach to surface hopping. *The Journal of Chemical Physics* 2023; 159(9): 094115. http://dx.doi.org/10.1063/5.0158147 doi: 10.1063/5.0158147

149. Lawrence JE, Ansari IM, Mannouch JR, et al. A MASH simulation of the photoexcited dynamics of cyclobutanone. *The Journal of Chemical Physics* 2024; 160(17): 174306. http://dx.doi.org/10.1063/5.0203695 doi: 10.1063/5.0203695

150. Tully JC. Molecular dynamics with electronic transitions. *J. Chem. Phys.* 1990; 93(2): 1061–1071. http://dx.doi.org/10.1063/1.459170 doi: 10.1063/1.459170

151. Subotnik JE, Jain A, Landry B, Petit A, Ouyang W, Bellonzi N. Understanding the Surface Hopping View of Electronic Transitions and Decoherence. *Annu. Rev. Phys. Chem.* 2016; 67(1): 387–417. http://dx.doi.org/10.1146/annurev-physchem-040215-112245 doi: 10.1146/annurev-physchem-040215-112245

152. Fregoni J, Granucci G, Persico M, Corni S. Strong Coupling with Light Enhances the Photoisomerization Quantum Yield of Azobenzene. *Chem* 2020; 6(1): 250–265. http://dx.doi.org/10.1016/j.chempr.2019.11.001 doi: 10.1016/j.chempr.2019.11.001

153. Antoniou P, Suchanek F, Varner JF, Foley JJ. Role of Cavity Losses on Nonadiabatic Couplings and Dynamics in Polaritonic Chemistry. *J. Phys. Chem. Lett.* 2020; 11(21): 9063–9069. http://dx.doi.org/10.1021/acs.jpclett.0c02406 doi: 10.1021/acs.jpclett.0c02406

154. Hu D, Mandal A, Weight BM, Huo P. Quasi-Diabatic Propagation Scheme for Simulating Polariton Chemistry. *J. Chem. Phys.* 2022. http://dx.doi.org/10.1063/5.0127118 doi: 10.1063/5.0127118

155. Malone W, Nebgen B, White A, et al. NEXMD Software Package for Nonadiabatic Excited State Molecular Dynamics Simulations. *J. Chem. Theory Comput.* 2020; 16(9): 5771–5783. http://dx.doi.org/10.1021/acs.jctc.0c00248 doi: 10.1021/acs.jctc.0c00248

156. Granucci G, Persico M, Zoccante A. Including quantum decoherence in surface hopping. *J. Chem. Phys.* 2010; 133(13): 134111. http://dx.doi.org/10.1063/1.3489004 doi: 10.1063/1.3489004

157. Subotnik JE, Shenvi N. A new approach to decoherence and momentum rescaling in the surface hopping algorithm. *J. Chem. Phys.* 2011; 134(2): 024105. http://dx.doi.org/10.1063/1.3506779 doi: 10.1063/1.3506779

158. Jaeger HM, Fischer S, Prezhdo OV. Decoherence-induced surface hopping. *J. Chem. Phys.* 2012; 137(22): 22A545. http://dx.doi.org/10.1063/1.4757100 doi: 10.1063/1.4757100

159. Wang L, Trivedi D, Prezhdo OV. Global Flux Surface Hopping Approach for Mixed Quantum-Classical Dynamics. *J. Chem. Theory Comput.* 2014; 10(9): 3598–3605. http://dx.doi.org/10.1021/ct5003835 doi: 10.1021/ct5003835

160. Bossion D, Ying W, Chowdhury SN, Huo P. Non-adiabatic mapping dynamics in the phase space of the SU(N) Lie group. *J. Chem. Phys.* 2022; 157(8): 084105. http://dx.doi.org/10.1063/5.0094893 doi: 10.1063/5.0094893

161. Hammes-Schiffer S, Tully JC. Proton transfer in solution: Molecular dynamics with quantum transitions. *J. Chem. Phys.* 1994; 101(6): 4657–4667. http://dx.doi.org/10.1063/1.467455 doi: 10.1063/1.467455

162. Plasser F, Ruckenbauer M, Mai S, Oppel M, Marquetand P, González L. Efficient and Flexible Computation of Many-Electron Wave Function Overlaps. *J. Chem. Theory Comput.* 2016; 12(3): 1207–1219. http://dx.doi.org/10.1021/acs.jctc.5b01148 doi: 10.1021/acs.jctc.5b01148

163. Shu Y, Zhang L, Chen X, Sun S, Huang Y, Truhlar DG. Nonadiabatic Dynamics Algorithms with Only Potential Energies and Gradients: Curvature-Driven Coherent Switching with Decay of Mixing and Curvature-Driven Trajectory Surface Hopping. *J. Chem. Theory Comput.* 2022; 18(3): 1320–1328. http://dx.doi.org/10.1021/acs.jctc.1c01080 doi: 10.1021/acs.jctc.1c01080

164. Casal T. dM, Toldo JM, Pinheiro Jr M, Barbatti M. Fewest switches surface hopping with Baeck-An couplings. *Open Res Europe* 2021; 1: 49. http://dx.doi.org/10.12688/openreseurope.13624.1 doi: 10.12688/openreseurope.13624.1

165. Cotton SJ, Miller WH. Trajectory-adjusted electronic zero point energy in classical Meyer-Miller vibronic dynamics: Symmetrical quasiclassical application to photodissociation. *J. Chem. Phys.* 2019; 150(19): 194110. http://dx.doi.org/10.1063/1.5094458 doi: 10.1063/1.5094458

166. Huo P, Coker DF. Communication: Partial linearized density matrix dynamics for dissipative, non-adiabatic quantum evolution. *J. Chem. Phys.* 2011; 135(20): 201101. http://dx.doi.org/10.1063/1.3664763 doi: 10.1063/1.3664763

167. Yang J, Pei Z, Leon EC, et al. Cavity quantum-electrodynamical time-dependent density functional theory within Gaussian atomic basis. II. Analytic energy gradient. *The Journal of Chemical Physics* 2022; 156(12): 124104. http://dx.doi.org/10.1063/5.0082386 doi: 10.1063/5.0082386

168. Luk HL, Feist J, Toppari JJ, Groenhof G. Multiscale Molecular Dynamics Simulations of Polaritonic Chemistry. *J. Chem. Theory Comput.* 2017; 13(9): 4324–4335. http://dx.doi.org/10.1021/acs.jctc.7b00388 doi: 10.1021/acs.jctc.7b00388

169. Epifanovsky E, Gilbert ATB, Feng X, et al. Software for the frontiers of quantum chemistry: An overview of developments in the Q-Chem 5 package. *J. Chem. Phys.* 2021; 155(8): 084801. http://dx.doi.org/10.1063/5.0055522 doi: 10.1063/5.0055522

170. Werner HJ, Knowles PJ, Knizia G, Manby FR, Schütz M. Molpro: a general-purpose quantum chemistry program package. *WIREs Computational Molecular Science* 2012; 2(2): 242–253. http://dx.doi.org/10.1002/wcms.82 doi: 10.1002/wcms.82

171. Werner HJ, Knowles PJ, Manby FR, et al. The Molpro quantum chemistry package. *The Journal of Chemical Physics* 2020; 152(14): 144107. http://dx.doi.org/10.1063/5.0005081 doi: 10.1063/5.0005081

172. Rupp M, Tkatchenko A, Müller KR, Lilienfeld vOA. Fast and Accurate Modeling of Molecular Atomization Energies with Machine Learning. *Phys. Rev. Lett.* 2012; 108(5): 058301. http://dx.doi.org/10.1103/PhysRevLett.108.058301 doi: 10.1103/PhysRevLett.108.058301

173. Rupp M. Machine learning for quantum mechanics in a nutshell. *International Journal of Quantum Chemistry* 2015; 115(16): 1058–1073. http://dx.doi.org/10.1002/qua.24954 doi: 10.1002/qua.24954

174. Hu D, Xie Y, Li X, Li L, Lan Z. Inclusion of Machine Learning Kernel Ridge Regression Potential Energy Surfaces in On-the-Fly Nonadiabatic Molecular Dynamics Simulation. *J. Phys. Chem. Lett.* 2018; 9(11): 2725–2732. http://dx.doi.org/10.1021/acs.jpclett.8b00684 doi: 10.1021/acs.jpclett.8b00684

175. Hu D, Huo P. Ab Initio Molecular Cavity Quantum Electrodynamics Simulations Using Machine Learning Models. *J. Chem. Theory Comput.* 2023. http://dx.doi.org/10.1021/acs.jctc.3c00137 doi: 10.1021/acs.jctc.3c00137

176. Koessler ER, Mandal A, Huo P. Incorporating Lindblad Decay Dynamics into Mixed Quantum-Classical Simulations. *J. Chem. Phys.* 2022; 157(6): 064101. http://dx.doi.org/10.1063/5.0099922 doi: 10.1063/5.0099922

177. Guo R, Hakala TK, Törmä P. Geometry dependence of surface lattice resonances in plasmonic nanoparticle arrays. *Phys. Rev. B* 2017; 95(15): 155423. http://dx.doi.org/10.1103/PhysRevB.95.155423 doi: 10.1103/PhysRevB.95.155423

178. Taylor MAD, Weight BM, Huo P. Reciprocal asymptotically decoupled Hamiltonian for cavity quantum electrodynamics. *Phys. Rev. B* 2024; 109(10): 104305. http://dx.doi.org/10.1103/PhysRevB.109.104305 doi: 10.1103/PhysRevB.109.104305

179. Svendsen MK, Ruggenthaler M, Hübener H, et al. Theory of Quantum Light-Matter Interaction in Cavities: Extended Systems and the Long Wavelength Approximation. 2023. arXiv, 2024, 10.48550/arXiv.2312.17374http://dx.doi.org/10.48550/arXiv.2312.17374 doi: 10.48550/arXiv.2312.17374

180. Campos-Gonzalez-Angulo JA, Yuen-Zhou J. Generalization of the Tavis–Cummings model for multi-level anharmonic systems: Insights on the second excitation manifold. *The Journal of Chemical Physics* 2022; 156(19): 194308. http://dx.doi.org/10.1063/5.0087234 doi: 10.1063/5.0087234

181. Schnappinger T, Sidler D, Ruggenthaler M, Rubio A, Kowalewski M. Cavity Born–Oppenheimer Hartree–Fock Ansatz: Light–Matter Properties of Strongly Coupled Molecular Ensembles. *J. Phys. Chem. Lett.* 2023; 14(36): 8024–8033. http://dx.doi.org/10.1021/acs.jpclett.3c01842 doi: 10.1021/acs.jpclett.3c01842

182. Pracht P, Grant DF, Grimme S. Comprehensive Assessment of GFN Tight-Binding and Composite Density Functional Theory Methods for Calculating Gas-Phase Infrared Spectra. *J. Chem. Theory Comput.* 2020; 16(11): 7044–7060. http://dx.doi.org/10.1021/acs.jctc.0c00877 doi: 10.1021/acs.jctc.0c00877

183. Grimme S, Müller M, Hansen A. A non-self-consistent tight-binding electronic structure potential in a polarized double-ζ basis set for all spd-block elements up to Z = 86. *The Journal of Chemical Physics* 2023; 158(12): 124111. http://dx.doi.org/10.1063/5.0137838 doi: 10.1063/5.0137838

184. Grimme S, Bannwarth C, Shushkov P. A Robust and Accurate Tight-Binding Quantum Chemical Method for Structures, Vibrational Frequencies, and Noncovalent Interactions of Large Molecular Systems Parametrized for All spd-Block Elements (Z = 1–86). *J. Chem. Theory Comput.* 2017; 13(5): 1989–2009. http://dx.doi.org/10.1021/acs.jctc.7b00118 doi: 10.1021/acs.jctc.7b00118

185. Humeniuk A, Mitrić R. DFTBaby: A software package for non-adiabatic molecular dynamics simulations based on long-range corrected tight-binding TD-DFT(B). *Computer Physics Communications* 2017; 221: 174–202. http://dx.doi.org/10.1016/j.cpc.2017.08.012 doi: 10.1016/j.cpc.2017.08.012

186. Asadi-Aghbolaghi N, Rüger R, Jamshidi Z, Visscher L. TD-DFT+TB: An Efficient and Fast Approach for Quantum Plasmonic Excitations. *J. Phys. Chem. C* 2020; 124(14). http://dx.doi.org/10.1021/acs.jpcc.0c00979 doi: 10.1021/acs.jpcc.0c00979

187. Asadi-Aghbolaghi N, Rüger R, Jamshidi Z, Visscher L. TD-DFT+TB: An Efficient and Fast Approach for Quantum Plasmonic Excitations. *J. Phys. Chem. C* 2020; 124(14): 7946–7955. http://dx.doi.org/10.1021/acs.jpcc.0c00979 doi: 10.1021/acs.jpcc.0c00979

188. Alkan F, Aikens CM. TD-DFT and TD-DFTB Investigation of the Optical Properties and Electronic Structure of Silver Nanorods and Nanorod Dimers. *J. Phys. Chem. C* 2018; 122(41): 23639–23650. http://dx.doi.org/10.1021/acs.jpcc.8b05196 doi: 10.1021/acs.jpcc.8b05196

189. D'Agostino S, Rinaldi R, Cuniberti G, Della Sala F. Density Functional Tight Binding for Quantum Plasmonics. *J. Phys. Chem. C* 2018; 122(34): 19756–19766. http://dx.doi.org/10.1021/acs.jpcc.8b05278 doi: 10.1021/acs.jpcc.8b05278

190. Bradbury N, Ribeiro R, Caram JR, Neuhauser D. Polaritons in Large Stochastic Simulations of 2D Molecular Aggregates. 2023. http://dx.doi.org/10.48550/arXiv.2308.04385 doi: 10.48550/arXiv.2308.04385

191. Hestand NJ, Spano FC. Expanded Theory of H- and J-Molecular Aggregates: The Effects of Vibronic Coupling and Intermolecular Charge Transfer. *Chem. Rev.* 2018; 118(15): 7069–7163. http://dx.doi.org/10.1021/acs.chemrev.7b00581 doi: 10.1021/acs.chemrev.7b00581

192. Hestand NJ, Spano FC. Molecular Aggregate Photophysics beyond the Kasha Model: Novel Design Principles for Organic Materials. *Acc. Chem. Res.* 2017; 50(2): 341–350. http://dx.doi.org/10.1021/acs.accounts.6b00576 doi: 10.1021/acs.accounts.6b00576

193. Cohen-Tannoudji C, Dupont-Roc J, Grynberg G. *Photons and Atoms: Introduction to Quantum Electrodynamics*. Wiley . 1997.

194. Groenhof G, Toppari JJ. Coherent Light Harvesting through Strong Coupling to Confined Light. *J. Phys. Chem. Lett.* 2018; 9(17): 4848–4851. http://dx.doi.org/10.1021/acs.jpclett.8b02032 doi: 10.1021/acs.jpclett.8b02032

GRAPHICAL ABSTRACT

1×1

(Original size: 200×200 bp)

Please check the journal's author guidelines for whether a graphical abstract, key points, new findings, or other items are required for display in the Table of Contents.